Safe and Accurate Targeting for Transcranial Focused Ultrasound

By

M. Anthony Phipps

Dissertation

Submitted to the Faculty of the

Graduate School of Vanderbilt University

in partial fulfillment of the requirements

for the degree of

DOCTOR OF PHILOSOPHY

In

Chemical and Physical Biology

May 31, 2021

Nashville, Tennessee

Approved:

William Grissom, PhD

Charles Caskey, PhD

Brett Byram, PhD

Limin Chen, PhD

John Gore, PhD

Table of Contents

List of Figures

Figure Page Number

Chapter 1—Introduction

Focused ultrasound (FUS) is a versatile tool that allows for the non-invasive delivery of energy on the millimeter scale and is actively being applied to a number of research and clinical problems. Generally, FUS can affect tissue through two major mechanisms, mechanical and thermal. These two mechanisms can be either destructive or nondestructive depending on the chosen FUS parameters. Tissue can be destroyed though heating or mechanical disruption with high intensity ultrasound while lower intensities can be used for neuromodulation, targeted drug delivery, and other therapies. These multiple mechanisms of action allow FUS to be noninvasively applied to spatially select regions; however, many scientific and technical challenges remain to be solved.

Applications of FUS within the brain provide unique advantages for both research and therapy. FUS is able to pass through the intact skull and still cause effects within localized regions of the brain. Large aperture transducers can produce foci of millimeter scale, allowing for precise targeting of specific brain structures [1]. Destruction of tissue has been explored with histotripsy [2] and thermal ablation [3], [4] to treat clinical disorders. FUS can be used in conjunction with microbubbles to selectively open the blood brain barrier, allowing for the targeted uptake of drugs for research or treatment [5], [6]. Nanoemulsions that release drugs only when exposed to a FUS beam have been demonstrated for targeted drug release within the brain [7], [8]. The application of FUS has also been shown to cause neuromodulation in mammals from rodents to humans [9]–[11]. These applications of FUS provide tools to better

understand brain function and treat clinical conditions but more development is needed to be able to fully utilize these applications.

The ability to localize the FUS beam is especially important for transcranial applications, since the skull itself produces many challenges. The skull will reflect and absorb sound, which may cause damage to the skull. The skull also aberrates the FUS beam, leading to a larger focal area, less pressure at the focus, and shifts in the focal location. This dissertation presents work focused on improving the ability to accurately target brain regions with transcranial FUS. An introduction to acoustic propagation and transcranial FUS applications is presented in chapter 1. Chapter 2 describes the general methods and technologies used throughout this work. Chapter 3 presents original work studying the safety of a localization method. Chapter 4 presents work on improving said localization method while reducing the FUS dose. Chapter 5 explores the ability to target specific brain regions. The final chapter presents overall conclusions and future work to continue to improve transcranial FUS procedures.

1.1—Ultrasound wave equation and tissue interactions

Ultrasound waves are longitudinal acoustic waves with frequency above the hearing range of humans. These waves can travel though tissues where they can generate a variety of bioeffects. In a longitudinal wave, particles are displaced in the wave propagation direction, and tissue in the path of the wave experience alternating pressure above and below the ambient pressure. During the compression phase of the wave, the tissue will experience increased pressure and density while the opposite effects will occur during the rarefaction phase. During

FUS experiments the peak negative pressure (PNP), the frequency, and the duration of the wave are all parameters which can change the bioeffects that the tissue will experience.

A low amplitude acoustic wave traveling through a lossless and homogenous medium can be described by a series of coupled differential equations. The individual equations covering the conservation of momentum, conservations of mass, and the relationship between pressure and density are as follows:

$$\frac{\partial u}{\partial t} = -\frac{1}{\rho_0}\frac{\partial p}{\partial x} \quad \text{Eq. 1.1}$$

$$\frac{\partial \rho}{\partial t} = -\rho_0\frac{\partial u}{\partial x} \quad \text{Eq. 1.2}$$

$$p = c_0^2\rho \quad \text{Eq. 1.3}$$

where *u* is the particle velocity, *p* is pressure, ρ is the density, ρ_0 is the ambient density, and c_0 is the speed of sound. These equations can be combined to give the classic second order wave equation

$$\frac{\partial^2 p}{\partial x^2} = \frac{1}{c_0^2}\frac{\partial^2 p}{\partial t^2} \quad \text{Eq. 1.4}$$

A solution to this one-dimensional wave equation can be written as

$$p(x,t) = p_0 \sin(\omega t - kx) \quad \text{Eq. 1.5}$$

where ω is the angular frequency, *k* is the wavenumber ($k = 2\pi\lambda$ where λ is the wavelength), and p_0 is the ambient pressure. This results in a pressure changes in the media with compression of the media occurring during the increasing pressure half of the wave and rarefaction during the decreasing pressure half of the wave.

The Food and Drug Administration provides guidance for manufacturers building clinical imaging systems [12]. A number of methods for reporting the intensity of the ultrasound beam relevant for safety considerations have been established and are provided here. These include the spatial peak pulse average intensity (I_{sppa}) and the spatial peak temporal average intensity (I_{spta}) (figure 1). The intensity of the wave can be calculated as

$$I(t) = \frac{p(t)^2}{2\rho c} \quad \text{Eq. 1.6}$$

This intensity is in W/m^2 and for a focused beam, generally the spatial peak intensity at the focus is reported. The instantaneous intensity can be calculated for any point in time. The pulse average intensity can be calculated by first taking the pulse intensity integral

$$PII = \int_{t_1}^{t_2} \frac{p^2(t)}{\rho c} dt' \quad \text{Eq. 1.7}$$

Where the integral period (t_1 to t_2) occurs over a single pulse [13]. The pulse duration (PD) is defined as 1.25 times the time between the intensity integral reaching 10% of the PII and 90% of the PII. The pulse repetition frequency (PRF) can be defined at the number of pulses per second that are generated. Using these values, I_{sppa} can be calculated as

$$I_{sppa} = \frac{PII}{PD} \quad \text{Eq. 1.8}$$

and I_{stpa} can be calculated as

$$I_{spta} = \frac{PII}{PRF} \quad \text{Eq. 1.9}$$

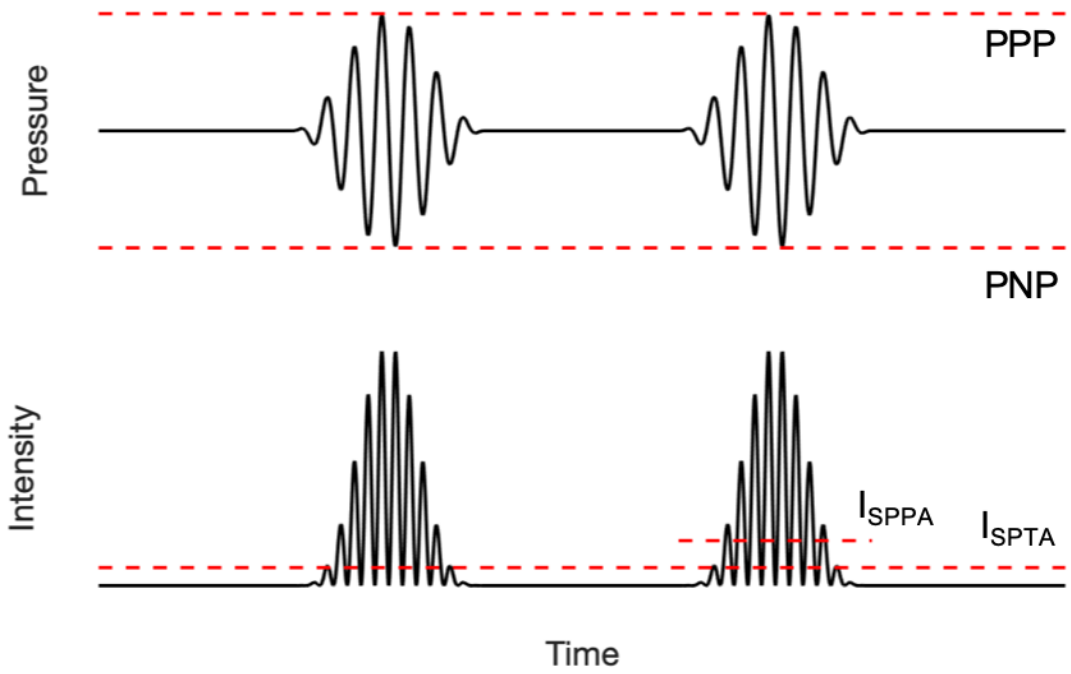

Figure 1.1: Ultrasound waves can be characterized peak positive pressure (PPP) and peak negative pressure (PNP). Intensity measurements can be made across a single pulse as in the spatial peak pulse average or across all pulses used as in the spatial peak temporal average.

These two intensity metrics both measure the spatial peak intensity of the FUS beam but use different time scales for the time averaging. The use of these intensity measures as safety metrics is discussed in section 1.3.

1.1.1—Reflections

For media which are neither homogenous nor lossless, which tend to be interesting for biological applications, a number of other phenomena can affect the propagation of waves. Different tissues can be characterized by the acoustic impedance z, where $z = \rho c$. For a wave that is normally incident from one tissue into another, a portion of the wave will be reflected from the interface by a factor that can be written as

$$R = \frac{z_2 - z_1}{z_2 + z_1} \qquad \text{Eq. 1.10}$$

where R is the displacement reflection coefficient, z_1 is the acoustic impedance in tissue 1, and z_2 is the acoustic impedance in tissue 2. The transmission coefficient can be calculated from

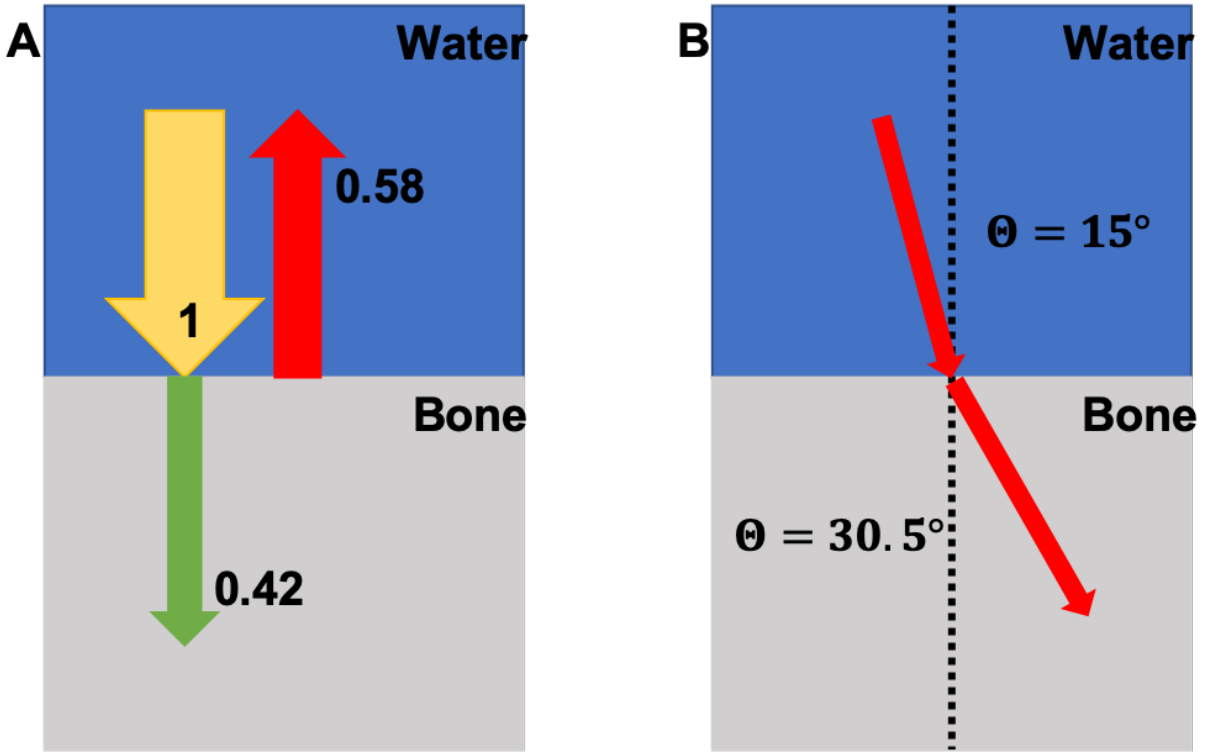

Figure 1.2: A: An example of the transmission and reflection of an ultrasound wave at a water bone interface. 58% of the incoming wave will be reflected off the interface due to the acoustic impedance mismatch between the materials. B: An example of the refraction of the wave due to speed of sound mismatch between materials.

this reflection coefficient as T = 1 – R. For an interface that consists of water and bone, where the acoustic impedance of water can be calculated by z_{water} = 1000 kg/m^3 * 1480 m/s and the acoustic impedance of bone can be calculated by z_{bone} = 1900 kg/m^3 * 2900 m/s [14], the reflection coefficient will be 0.58 and the transmission coefficient will be 0.42 (figure 1.2 A). For transmission from bone into water the reflectivity coefficient will be -0.58 representing a wave that is 180° out of phase with the incident wave and the transmission coefficient will be 1.58 resulting in an increased pressure after transmission into the water. For a simplified three layer

model of water-bone-water the transmission though bone of a normally incident wave will be 67% amplitude of the incident wave.

For incident angles which are not normal, a larger portion of the wave will be reflected depending on the incident angle and the speed of sound in each tissue. We can apply Snell's law to the acoustic wave such that

$$\frac{\sin\theta_1}{c_1} = \frac{\sin\theta_2}{c_2} \qquad \text{Eq. 1.11}$$

where θ_1 is the incident angle on the boundary of tissue 1 and 2 and θ_2 is the transmission angle of the wave into tissue 2. Using the same sound speeds from above, an ultrasound wave at an incident angle of 15° will be transmitted at an angle of 30.5° in the skull (figure 1.2 B). If the incident angle is too steep (past a critical angle θ_c) between tissues with different sound speeds then all of the wave will be reflected and nothing will be transmitted. For the interface between the water and bone the critical angle for an incident wave can be calculated to be 30.7°, past this angle no sound will be transmitted.

1.1.2—Attenuation

As the ultrasound wave travels through tissue it will be attenuated. This loss in pressure is primarily caused by two mechanisms, scattering and absorption [15]. As ultrasound waves pass through an inhomogeneous tissue, the waves will reflect off small density and speed of sound inhomogeneities in the tissue and be scattered [16]. Classical absorption occurs when the density of the tissue comes out of phase with the propagating wave due to frictional forces acting on the particle motion [17]. This absorption causes viscous heating of the tissue which

can be harnessed for therapies but should be avoided during other procedures. Attenuation of ultrasound can be modeled with a power law with respect to frequency

$$p = p_0 e^{-\alpha(f)x} \quad \text{Eq. 1.12}$$

where x is the distance traveled in tissue in cm and $\alpha(f) = af^b$ where a is the attenuation coefficient and generally ranges from 0.1 to 0.7 dB cm^{-1} MHz^{-b} for soft tissues, *f* is the frequency of the transducer, and *b* is tissue dependent parameter which is close to 1 for most biological tissues [15]. This results in reduced pressure with increasing depth.

1.1.3—Transmission of FUS through the skull

The transmission of focused ultrasound through skull bone will be of concern for the work described in this dissertation. For transcranial FUS special attention needs to be paid the skull. Skulls consist of three layers of bone, an outer layer (referred to as a table) of hard, dense bone, an intermediate porous layer, and an inner table similar to the outer table [14]. The porous part of the skull attenuates sound much more strongly than the outer or inner table [14]. Since attenuation increases with increased frequency it is advantageous to use lower frequencies in transcranial applications where the skull is a strong attenuator. Because of this transcranial FUS is often applied at frequencies below 1MHz.

For ablative treatments, the ratio of the density of the inner porous layer to the density of the outer tables is reported as the skull density ratio (SDR). Treatments have been reported to be more effective in patients with a higher SDR, though more adverse events have also occurred in these patients [18], [19]. Jung et al reported that the incident angle on the skull impacted reflection and transmission of FUS with angles greater than 25° showing significant

reflections in addition to SDR effects [20]. The impact of incident angle on transmitted pressure has been studied in a laboratory setting as well. A human skull fragment was placed on a rotation stage between a transducer and hydrophone and the focal pressure was recorded. When comparing an incident angle of 40° to an angle of 0°, the pressure transmitted was reduced to less than half [21].

Experimental studies of attenuation through the skull have found that much of the pressure loss can be attributed to reflection, scattering, and mode conversion with only a limited amount of the ultrasound being absorbed. Fry and Barger found that the angle of scattered sound from the porous inner layer of the skull was independent from the amplitude of the scattered sound [14]. This finding suggests that much of the pressure loss though the skull is due to sound being scattered rather than absorbed. Pinton et al. used high resolution bone images along with numerical modeling of sound propagation and heating to compare the pressure loss in experimental conditions with the modeled data. They found that only a small portion of the measured attenuation (16.6 dB/cm) was due to longitudinal absorption (2.7 dB/cm) or shear absorption (5.4 dB/cm) when transmitting though the skull [22].

1.1.4—Nonlinearity and radiation force

At low acoustic pressure the compression and rarefaction of the tissue do not significantly change the tissue density. Once the pressure is high enough, such as near the focus, the density change of the tissue becomes significant and will change the speed of sound in the tissue. In regions of high pressure the tissue has a higher speed of sound and in regions of low pressure the tissue has a slower speed of sound. These changes in the speed of sound

result in the shape of the wave changing and generating additional frequency content, such as harmonics of the center frequency.

One consequence of these nonlinear terms is the generation of the acoustic radiation force (ARF). This force results from a transfer of momentum from the acoustic ultrasound wave to the tissue in the direction of wave propagation. The momentum transfer is due to a nonzero time average of momentum from the nonlinear term in the wave equation [23]. The radiation force can be described by the following equation

$$F_{rad} = \frac{2\alpha I_{sppa}}{c} \qquad \text{Eq. 1.13}$$

where α is the absorption coefficient, *I* is the intensity, and c is the speed of sound. Since absorption scales with frequency of the ultrasound there are two ways to increase the radiation force: use a higher frequency transducer or use a more intense pulse.

In a biological tissue this force causes a displacement in the tissue. These displacement can measured using ultrasound [24] or MRI [25] to localize the beam or study tissue characteristics. Tissue stiffness, often characterized by the Young's modulus, will affect how much the radiation force can push the tissue. Stiffer materials will displace less compared to softer tissues for the same applied force [26].

1.2—Transcranial Focused Ultrasound Transducers

FUS is generated using ultrasound transducers. These transducers consist of a piezoelectric element which consists of material that change shape when the surface charge changes. When a voltage pulse is applied to a piezoelectric material, the dipole moments in the material shift in distribution leading to a proportional change to the thickness of the material

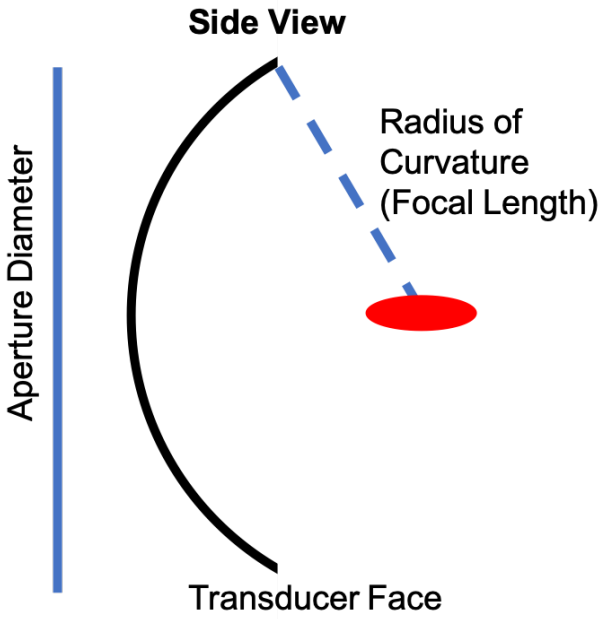

Figure 1.3: A side view schematic of a spherically focused FUS transducer. Transducers are characterized by the aperture diameter and radius of curvature.

[27]. The opposite also occurs, where force which causes a shape change in the piezoelectric material will generate a surface charge allowing detection of the force. Applying a sinusoidal electrical wave to the piezoelectric material will result in mechanical pressure waves being generated from the material which can be transmitted into tissue. As described in equation 1.10, pressure waves will reflect at the interface of materials with different acoustic impedances. Matching layers can be placed between the piezoelectric element and the tissue to improve transmission of the pressure wave [28], [29].

1.2.1—Typical transducers in transcranial focused ultrasound

FUS transducers are often spherical caps, where sound waves generated at any point on the face of the transducer at the same time will arrive at the geometric center of sphere in phase and result in a large pressure only at the focus, referred to as the focal gain (figure 1.3). Generally, FUS transducers are designed to apply the maximum amount of energy into the

smallest focus size at a distance that allows the transducer to noninvasively target the region of interest. Transcranial applications need a focal length that allows the transducer to be placed outside of the head while sonicating targets within brain. Since the attenuation of ultrasound waves is frequency dependent (eq. 1.12), transducers with a center frequency below 1 MHz are often used for transcranial applications for better transmission of energy [30].

Transducers can be described with a number of characteristics: frequency, radius of curvature, and aperture diameter. Each of these characteristics influences the focal shape and location. Transducers only resonate at certain frequencies dependent on the thickness of the piezoelectric element. The element is designed so that it is one half wavelength thick allowing for waves with the corresponding frequency to be emitted in phase. This design also allows the element to resonate at the harmonics of the designed frequency which can be used to expand the applications of the transducer [31].

1.2.3—The effect of f-number on focal spot size

The radius of curvature of the transducer determines where the geometric focus is located relative to the transducer face. The aperture diameter is the diameter of the face of the transducer and the ratio of the radius of curvature to aperture diameter is the f-number of the transducer

$$f/\# = \frac{ROC}{D} \qquad \text{Eq. 1.14}$$

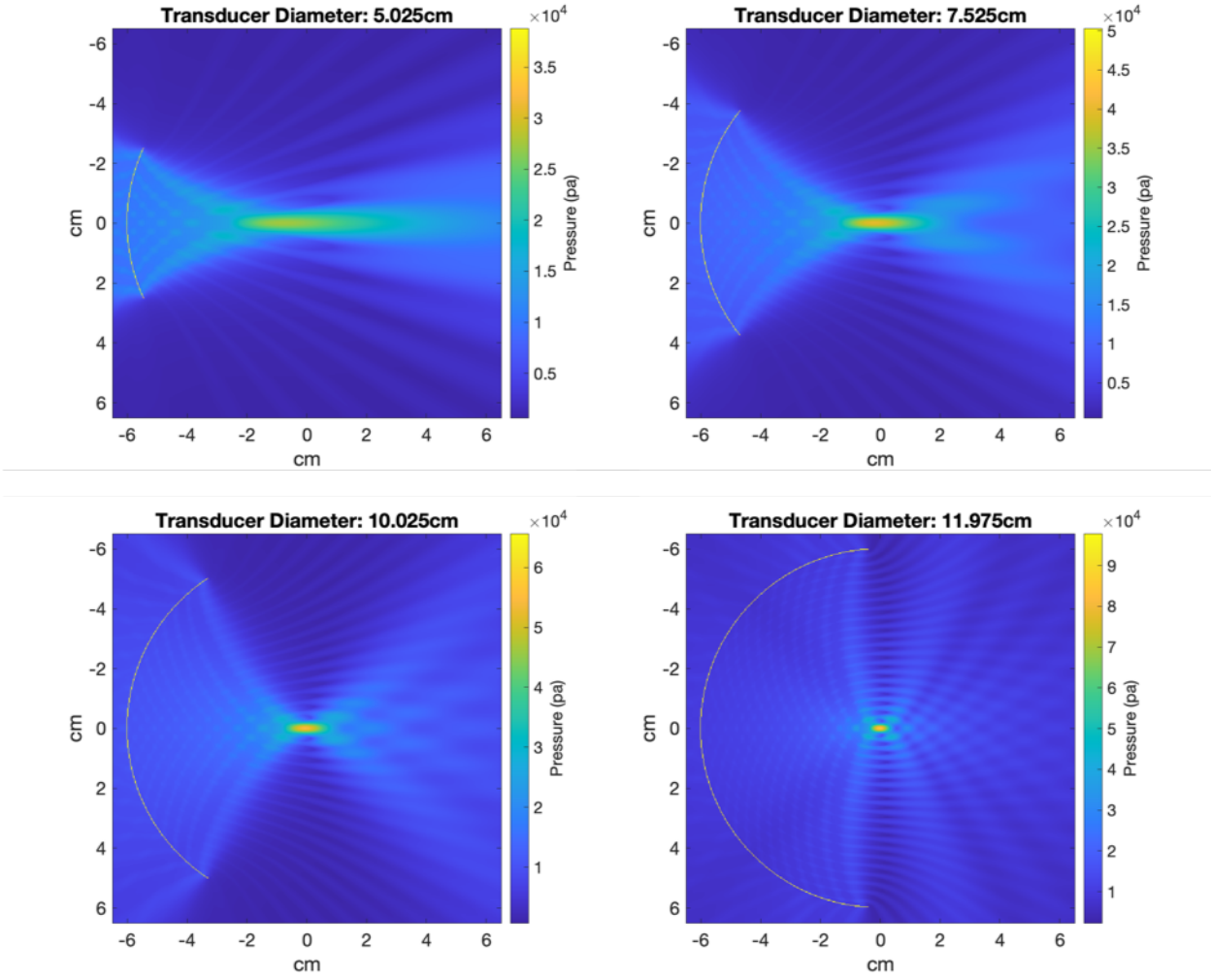

Figure 1.4: 2D simulations showing the effects of changing the transducer aperture. Each simulation is plotted on separate colormaps to show the focus. The same input wave was used for each simulation. There is increasing focal gain with larger apertures while maintaining the radius of curvature and frequency. The larger apertures, with smaller f-numbers, also have tighter focal shapes in both the lateral and axial directions.

where ROC is the radius of curvature of the transducer and D is the aperture diameter. A spherical transducer with a lower f-number and the same ROC will have a larger surface area generated ultrasound waves resulting in more focal gain and a smaller focal size. Figure 1.4 illustrates simple 3D simulations of spherical transducers with different aperture diameters showing the relationship between f-number and focal shape. As the aperture of the transducer increased the pressure at the focus increases as seen by the changing color bars. The focus is smaller in both the axial and lateral beam directions with a larger aperture for the same radius of curvature.

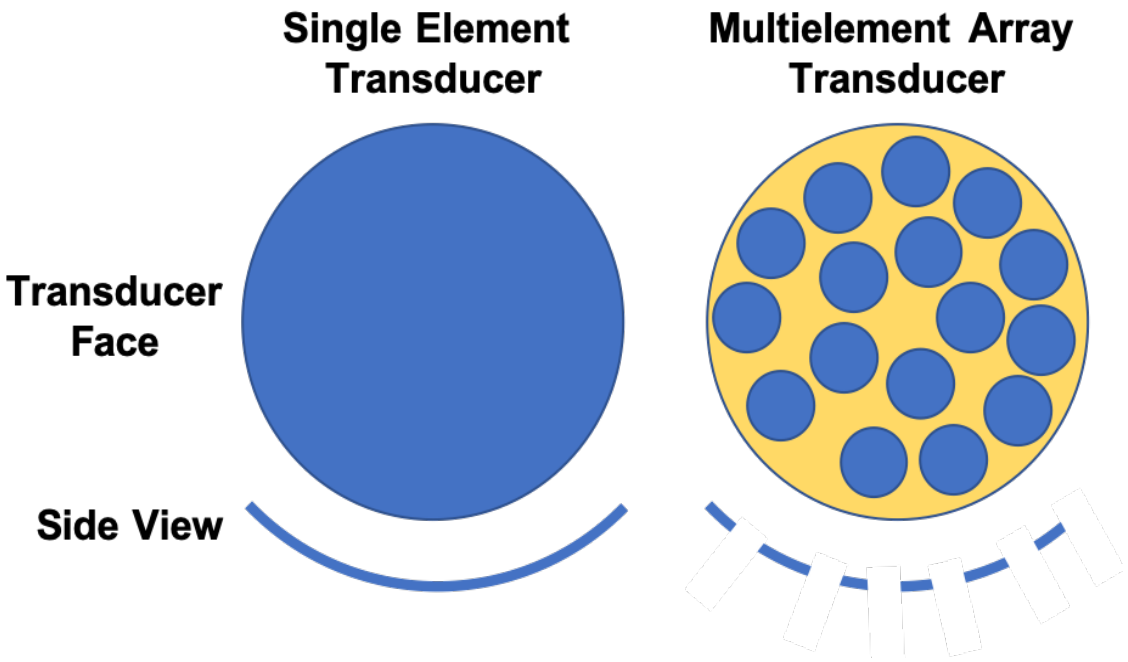

Figure 1.5: Example of single element transducer (left) vs multielement array transducer (right). A single element transducer has the full surface of the transducer as the active element. Spherically focused transducers are often used for therapeutic arrays, and the cross section of this array is the arc of a circle. Multielement arrays use a number of independent elements spaced out on the surface of the transducer. Each of these elements can be independently controlled.

1.2.2—Single element versus array transducers

Transducers can be made using a single piezoelectric element or an array of multiple elements (figure 1.5). A single element design is limited to sonicating only at its geometric focus, however these transducers are relatively cheap and do not require large banks of amplifiers. In contrast, a phased array can consist of hundreds or thousands of elements which can each be individually controlled allowing for electronic steering of the focus and aberration correction. Methods have been developed which allow for complex patterns to be generated where the focus can be steered away from the geometric focus of the transducer and multiple foci can be generated [32]. The ability to steer the focus of the transducer allows for a wider range for research and clinical applications. Individual control of each element allows for aberration correction to minimize the effects of the skull on the focus size and energy [33]. The focus location and intensity can be improved estimating the phase aberration induced by the skull with simulations [34], [35].

Much of the early work on transcranial FUS transducers was centered around thermal therapy applications. In 1977 a 1 MHz single element FUS transducer was shown to be able to induce thermal changes in a phantom after sonicating though a human skull [36]. Later, multielement phased arrays were developed for transcranial FUS. Clement et al. custom designed a 64 element phased array transducer for transcranial thermal therapy and discussed the tradeoffs in the transducer parameter space [37]. While higher frequencies provide a smaller focus at the target, more of the energy is absorbed by the skull at those higher frequencies. Simulations showed that larger numbers of elements provided better aberration correction through the skull but considerations need to be made with the cost and difficulty of

manufacturing an array with very large numbers of elements [37]. Further work by the same group designed a 500 element array which was used to test thermal ablation though a human skull in rabbits with MR guidance [38]. This transducer was able to steer to multiple targets and use aberration correction to improve the focus.

A clinical system for brain ablation has been designed and used for treatment of essential tremor by ablation of the thalamus. The ExAblate 4000 (InSightec, Haifa, Israel) consists of a MR compatible 1024 element hemisphere. This transducer has a 30 cm diameter and can operate at 650 kHz and phase correction can be applied to improve the focus [33], [39]. NaviFUS (NaviFUS Inc., Taipei, Taiwan) have produced a phased array transducer which can be coupled to a neuro-navigation tool to target specific brain structure outside of a MR suite for blood brain barrier opening [40]. Work presented in chapters 4 and 5 of this dissertation uses a transducer which was designed to sonicate a non-human primate (NHP) brain. This transducer is a 128-element phased array designed using simulations of random element locations and different radius of curvature, diameter, and coverage to optimize the focus size and steering. This resulted in a transducer with a diameter of 10.3 cm and a radius of curvature of 7.2 cm (f-number 0.7). The transducer could be steered ± 10 mm in the lateral direction and ± 20 mm in the axial direction [1].

1.3—FUS safety

When considering ultrasound safety, the bioeffects of FUS can be broadly divided into two categories: mechanical and thermal damage. Currently there is little formal guidance on the safety of long FUS pulses, especially for novel applications such as blood brain barrier (BBB)

opening and neuromodulation. The FDA has published guidelines for imaging pulses to limit the risk of heating and cavitation [12]; however, imaging pulses are normally single cycle pulses, unlike the multi-cycle pulses, often in the thousands, for therapeutic FUS. The ALARA principle ("as low as reasonably achievable") is a good practice to follow to reduce the likelihood of damage [41], [42]. For this reason, it is best to limit the ultrasound dose as much as possible within the confines of the experiment or treatment. This is especially true for localizing the FUS beam in areas where excess dose may cause unintended and undesired damage. Therefore, it is important to develop methods that minimize the necessary dose for beam localization, which this dissertation addresses.

1.3.1—Mechanical

Mechanical damage to tissue can occur due to inertial cavitation. Cavitation can occur during the rarefaction phase of the wave, where the low pressure can cause a gas bubble to form inside the tissue [43]. This bubble will then collapse during the high-pressure phase of the wave and can cause damage to surrounding tissue. Bubbles can form rapidly and the mechanism for damage has been adopted for therapy to kill tissues [2]. A major driving force for cavitation is the peak negative pressure (PNP) experienced by the tissue, however the effects vary with the center frequency. Theoretical models were developed to study the cavitation threshold and determine at what pressure for a given frequency cavitation was likely to occur [43], [44]. Experimental data from sonications in water or fluids which may contain cavitation nuclei generally fit these models [44]. The mechanical index (MI) is often used to estimate cavitation risk and is defined as

$$MI = \frac{PNP}{\sqrt{f_c}} \quad \text{Eq. 1.15}$$

where the PNP is in megapascal and f_c is the center frequency in megahertz. A theoretical study for MI, when performing ultrasound acoustic radiation force imaging (ARFI) pulses, found that the effect of longer duration pulses used for ARFI have only minor changes on the inertial cavitation threshold in tissue [45]. In this theoretical modeling of tissues, the exponent on the frequency in the MI equation was found to potentially be lower than necessary. Written as $MI = \frac{PNP}{f_c^n}$ where n = 0.5 currently, a value of n = 0.75 fits the calculation for inertial cavitation threshold for tissues with optimally sized bubbles. When these theoretical calculations were compared against the limited number of reported values for cavitation thresholds in tissue, it was found that the theoretical estimates were much smaller than the reported values, suggesting that optimally sized bubbles are not present in these tissues and that MI may not be the best estimate of cavitation damage in biological tissues [45]. Nonetheless, this discrepancy between theoretical and experimental data suggest an overestimation of risk so pulses which are below the current MI limits are more likely to be safe.

The FDA limits the maximum MI for imaging pulses to 1.9 with a smaller value of 0.23 for ophthalmic imaging [12], [46]. I_{sppa}, defined in equation 1.8, is a second metric used by the FDA to ensure safe pulses. I_{sppa} represents the average intensity at the spatial maximum during a single pulse with units of W/cm^2 and cavitation risk will increase is increasing intensity. The FDA limit for I_{sppa} for imaging pulses is 190 W/cm^2 except in ophthalmic imaging where the limit is 28 W/cm^3 [12], [46].

1.3.2—Thermal

Thermal effects of ultrasound are driven by absorption of ultrasound causing viscous heating. Heating will be increased whenever there is more ultrasound being absorbed which can be caused by longer pulses, higher pressure, or higher frequency. I_{spta}, defined in equation 1.9, of ultrasound sonication has units of mW/cm^2, and since this is the intensity over time thermal risk will increase with increasing I_{spta}. FDA limits for I_{spta} vary from 17 mW/cm^2 for ophthalmic imaging to 720 mW/cm^2 for peripheral vessels [12] .

If biological tissues heat too much or for too long the cells will be damaged and can die. This heating is used therapeutically to kill diseased tissues in the body but should be avoided in off-target regions and for other uses of therapeutic ultrasound. Heating tissue to a high temperature can kill the cells in a relatively short period of time [47]. Exposure to heat for a long duration can also kill cells within the body. A common metric when assessing the likelihood of cell death is the cumulative minutes at 43°C (CEM43). This metric is calculated from the following equation

$$CEM43 = \sum_{t=0}^{t_{final}} R^{43-T}\Delta t \qquad \text{Eq. 1.16}$$

where T is the temperature during the timestep Δt and R is equal to 0.5 above 43°C and 0.25 under 43°C [48]. An increasing value for CEM43 increases the likelihood of cell death where 240 equivalent minutes is often used as a measure of treatment volume for ablation [49][50].

1.4—Transcranial FUS Applications

FUS has a number of transcranial applications for both clinical and research settings. The ability to deposit energy within a localized region of the brain without opening the skull

provides clinicians and researchers new possibilities when treating and studying the brain. Ultrasound energy can be applied to kill tissue with heating or mechanical disruption. FUS can be used in conjunction with microbubbles to open the BBB, or with nanoemulsions to locally release drugs. FUS can be used on its own to modulate neural activity. Because the methods require selective localization it is important to be able to accurately target and confirm the focus location within the brain before applying the therapy.

FUS ablation has been used clinically to treat essential tremor by heating and killing cells in the thalamus [3], [51]–[53]. Essential tremor causes uncontrollable shaking of the patient's hand which natively impacts the quality of life. The ability to surgically ablate the thalamus without having to remove the skull allows physicians to perform surgery with minimal risk of harming healthy brain tissue. FUS thalamotomy has shown a decrease in measured essential tremor over a long period of time in treated patients [52]. Ablation can also be used outside of the brain to treat prostate cancer [49] and uterine fibroids [50], [54], among other conditions.

Histotripsy is the use of very high pressure short duration FUS pulses which can mechanically disrupt and kill cells [2]. These pulses can be used to target brain structures while minimizing the risk to healthy tissue. Histotripsy pulses have been applied to open porcine brains and were able to generate large lesions while maintaining very tight boundaries between the treated and untreated tissue [55]. In addition to brain tissue destruction, histotripsy pulses have been used to liquify blood clots *in vitro* while sonicating through an intact human skull [56]. These papers together show an ability to affect biological tissues through the skull in order to treat clotting or tumors. For this technique to be applied clinically it will be important to only apply these FUS pulses to regions which need treatment.

FUS can be used for nondestructive therapy as well. Targeted drug delivery within the brain through BBB disruption or targeted drug release within the brain can be achieved with FUS. By introducing microbubbles into the blood stream and then sonicating within the brain, stable cavitation can force open the tight junctions in the brain [57]–[60]. This opening of the BBB allows for large molecules to be delivered to the brain which could not ordinarily cross the BBB. In a rat model the chemotherapeutic agent doxorubicin was able to be selectively delivered to one side of the brain by sonicating microbubbles circulating in the blood [61]. Similarly, BBB opening has been used to transfect neurons at specific brain regions to encode specific proteins [62], [63]. By forcing the expression of FUS responsive proteins it is possible to selectively modulate neural activity in the areas where the BBB was opened allowing study of brain function [62].

Similar to BBB breakdown, nanoemulsions can be used for targeted drug delivery. These nanoemulsions, which consist of a perfluorocarbon and drug of interest surrounded by a block copolymer, will release the drug when the particle is sonicated [7]. This allows for a very high local drug dose while the systemic dose is below clinical levels. With this targeted drug release tool, specific areas of the brain can be subjected to drug levels for clinical or research purposes. Propofol loaded nanoparticles were used in a rat model and its brain was sonicated during a functional PET imaging session. The area of the brain where the FUS beam was located showed reduced glucose uptake and changes in functional connectivity maps were observed throughout the brain [64]. Delivery of anesthetics to spatially selective locations within the brain can help to understand how overall brain connectivity works by analyzing the changes throughout networks connected to the target.

1.4.1—Neuromodulation

Research has found that the application of FUS to brain tissue can lead to neuromodulation and the work presented in this dissertation contributed to ongoing neuromodulation studies [10], [65]. Both stimulation and inhibition has been observed with different FUS parameters. Reversible effects of ultrasound on neurons was first reported in the 1950s [66]. Ultrasound pulses through craniotomies in animal models showed elimination of cortical potentials evoked by a light stimulus following ultrasound exposure but these cortical potentials returned to baseline in a matter of minutes [67]. In 2008 Tyler et al. reported that low intensity, low frequency pulsed ultrasound was able to stimulate brain tissue samples *ex vivo* [68]. Further work was done in small animal models where the application of FUS to the brain resulted in changes to EMG signal or motor response in the tail or leg [69], [70]. The FUS pulses used in these studies were able to generate responses while maintaining I_{sppa} and MI below the highest FDA limits. A rodent study of various FUS parameters on the likelihood of observing EMG changes found an increased likelihood of stimulation with increasing I_{sppa}, I_{spta}, sonication duration and PRF. Lower frequency sonications caused stimulation at lower intensities compared to higher frequency sonications [11]. Following exposure to FUS, electrophysiology measurements of somatosensory evoked potentials can be altered for many minutes suggesting that the effects of FUS may induce long term changes to neuron activity allowing further clinical opportunities [71]. Suppressive effects have been observed in electrophysiology measurements of visual evoked potentials in rodents with FUS [72]. Yoo et al. tested the spatial selectivity of FUS neuromodulation in a rabbit model using fMRI as a readout

for brain activity by targeting specific brain areas [73]. In that study both stimulation of motor areas and suppression of visual areas were observed with different FUS parameters and in both cases the parameters were below the highest FDA limits for imaging pulses [73].

Experiments in NHPs allow for more complex behavior to be tested and the brain of a NHP shares more similarities with humans than small animal models [74]. The effects of FUS neuromodulation on NHP visuomotor behavior has been tested by sonicating the frontal eye field and observing eye motion tasks [75]–[77]. These studies found changes in the amount of time required for an eye motion task when the brain region responsible for eye motion was sonicated. In one of the experiments, electrophysiology measurements were taken at a distant, connected region of the brain and changes were observed in real time [76]. Brain activity has been measured using fMRI in NHPs to test the effects of FUS neuromodulation. Modulation of the somatosensory cortex responsible of paw touch reception with FUS has been compared to a direct tactile stimulation of the paw [10], [65]. The brain activity in the sonicated area of the brain and connected regions had similar responses to the tactile stimulation, however differences were observed in the latency of the response. This suggests a difference in the signal conduction pathway for when FUS stimulation was applied in the brain circuit compared to the normal stimulation [10]. When the FUS was applied to the somatosensory cortex while tactile stimulation was occurring, a suppression effect was observed, suggesting that FUS neuromodulation is state dependent [65]. Circuit level effects of FUS neuromodulation have been studied by sonicating brain regions in between resting state fMRI measurements. Following FUS neuromodulation circuit level changes were observed throughout the brain for regions connected to the sonicated area [9], [78].

FUS neuromodulation has been applied to humans as well. FUS was applied to the regions of the brain responsible for tactile sensations which resulted in the study participants reporting feeling sensations in their hands [79]. Changes in electrophysiology recordings were observed in addition to tactile sensations when stimulating this brain region [80]. Similarly, effects on electrophysiology records were observed in a different study where the spatial selectivity was also tested by moving the transducer to a new target eliminated the observed effects [81]. Behavior tasks have been used in addition to electrophysiology records to measure the effects of FUS neuromodulation. When stimulating the human primary motor cortex, a reduction in the amplitude of electrophysiology signals was observed along with a reduction in the reaction time to a stimulus response [82]. When targeting the thalamus, participants performed significantly worse than chance on a discrimination task during FUS sonications and electrophysiology signal amplitudes were also reduced [83].

These applications of transcranial FUS described here present a wide range of possibilities for better understanding of brain function and therapeutic treatments. FUS allows for spatially precise areas of the brain to be sonicated with the sonication effects limited to only the millimeter scale focal area. In order to use these applications successfully it is necessary to be able to accurately aim the transducer at brain region of interest and confirm that the FUS energy is localized at that target. When using FUS applications to localize the therapeutic focus prior to the actual treatment, there is risk that these sound waves may cause damage to healthy tissue. It is therefore important to be aware of the energy being used and limit the amount of energy needed to localize the FUS beam.

Chapter 2—Simulations, Measurements, and Guidance of FUS

This chapter will provide an overview of methods used throughout this dissertation to characterize and target ultrasound during transcranial application. A combination of methods including simulation, acoustic measurements, and closed-loop image-guided procedures are used to explore targeting accuracy and describe physical phenomena that occur during transcranial ultrasound. The present chapter describes the foundations of the tools used in this work and provides a context for how these tools are currently used in the field of transcranial ultrasound.

Because there is not a simple way to measure the ultrasound field during a transcranial procedure, researchers must rely on a combination of simulations, benchtop acoustic measurements, and real-time imaging to estimate the ultrasound fields that occur during therapy. Each method contributes different information. Simulations of pressure fields and heating are important for predicting the effects of transcranial FUS since direct measurement is difficult *in vivo*. Simulations allow for predictions of the transmission and aberration of the focus due to the skull and can help assess safety by predicting the heating that can occur due to the sonications. Laboratory measurements of the acoustic beam provide a basis for interpreting the simulation results and are required to assess the actual performance of the transducer being used for the experiments in terms of pressure output and focal shape. Imaging methods to visualize the FUS beam within the brain are important for knowing where the transducer is focusing sound during a procedure. Magnetic resonance imaging (MRI), can measure the effects

of the FUS beam to provide feedback about its location and effects. Optical tracking can be used in conjunction with biomedical imaging to estimate the beam location on biomedical images for aiming the transducer. Taken as a whole, information from each of these interrogation methods improve our understanding of targeting accuracy, dosimetry, and safety concerns.

2.1—Simulating ultrasound and its effects on tissue

Simulations of the FUS pressure field provide insight for both experimental planning and retrospective data analysis. Simulations through rodent skulls have revealed that *in vivo* pressure distribution and magnitude can be significantly different from a free field map of the pressure due to interactions with the skull [70]. Since the physical properties of the skull cause changes to the wave propagation, transcranial simulations have been used to estimate these changes and correct for them to maximize the focal energy [84]. The effects of FUS on tissue is pressure field dependent, thus when planning an experiment it is important to understand the distribution of the pressure field and when analyzing data it is important to understand what tissue was exposed to FUS and what was not. As discussed in section 1.3, FUS can harm healthy tissue through both thermal and mechanical effects and simulation can be used to manage the potential risk to tissue.

Generally, simulations work by solving the wave equation on a discretized grid that represents the area of interest for an experiment. Many variations on approaches to using computation to predict an acoustic focus have been developed to balance the competing interests of computation time, grid size, and accuracy. Simulations on homogenous media can

be performed relatively quickly by solving the Rayleigh-Sommerfeld integral to simulate the distribution of a complex pressure field emitted from a transducer in a large area [32]. The transducer is modeled as a collection of point sources and the Rayleigh-Sommerfeld integral sums the contribution of each of these points sources to estimate the pressure field [85]. This method has also been used in the design of transducers as it can simulate a large parameter space of design characteristics quickly but is not able to account for complex interactions in biological media [1]. Finite difference time domain (FDTD) simulations use numerical approximations of the spatial and temporal gradients about each node of a grid [86]. FDTD allow for arbitrary physical and acoustic properties throughout the grid which provide the ability to simulate FUS propagation through complex media like the skull [87]. Since the resolution of the simulation is determined by the grid spacing, these simulations can take a long time to complete or can only simulate a small area, though methods to perform these simulation at different resolutions within the grid can improve the speed of this simulations while providing accurate results [88]. The hybrid angular spectrum (HAS) method of simulation uses a grid of voxels where each voxel can have its own physical and acoustic properties. The spatial pressure field is simulated one plane at a time away from the transducer in the space domain and the spatial frequency domain [89]. This allows the simulations to be performed much faster while still simulating complex media. In determining the phases needed for aberration correction with simulations, HAS was shown to be over eight times faster compared to FDTD methods while having minimal difference from the FDTD solution [90].

Pressure simulations can be used as an input for heating simulations to can provide estimates for treatment when performing thermal therapies. Resultant thermal maps can be

used to estimate the safety of other applications where heating may pose risk of damage or influence the results of experiments. Simulations provide an important safety measure for both mechanical and thermal risk during transcranial FUS procedures and an ability to estimate the exposed tissue during experiments [31], [82], [83], [91], [92].

2.1.1—The K-Wave simulation package

The work in this dissertation uses the k-Wave package for MATLAB for all simulations [93]. This package solves acoustic equations using a k-space pseudospectral method on a Cartesian grid. A Fourier series is used to calculate the spatial derivatives for the wave equation which allows these calculations to be performed quickly by computers and requires fewer grid points per wavelength to accurately calculate the derivatives. The time domain gradients use a pseudospectral method to improve the numerical stability while using larger time steps compared to a FDTD method [93]. The k-Wave package can simulate heterogenous media while balancing the benefits of a full FDTD simulation of every spatial and temporal point with computational and speed advantages in HAS since both the spatial and temporal grid step size can be increased without sacrificing accuracy [94]. In transcranial simulations the FDTD and k-Wave package showed similar error while fewer points per wave were needed with the k-Wave package [95], [96].

2.1.2—Bioheat simulations

The heating of biological tissues can be modeled using Pennes' bioheat equations [97]. The equations add the effects of blood flow to diffusive heating modeling. Tissues are modeled

with their thermal conductivity, specific heat, and perfusion. The ultrasound pressure field and the parameter maps for absorption, speed of sound, and density are used to calculate the rate of heat deposition in W/m^3

$$Q = \frac{\alpha p^2}{\rho c} \quad \text{Eq. 2.1}$$

where Q is the volume rate of heat deposition, α is the absorption coefficient, p is the pressure amplitude, ρ is the density, and c is the speed of sound [98]. This heat source can be turned on and off during the simulation to represent the FUS being turned on and off.

2.1.3—Deriving acoustic parameters for simulation

To perform transcranial simulations, accurate physical and acoustic properties of the tissues must be known. The largest variation in material properties will be in the skull. Equation 1.10 shows that reflections are dependent on the difference in the acoustic impedance of the two media, therefore the density and speed of sound for each must be accurately inputted for simulations. Additionally, because the absorption is dependent on the absorption coefficient and the distance traveled through the tissue (equation 1.12) the absorption coefficient and the spatial thickness of tissues is important.

The current gold standard for transcranial simulations uses data from computed tomography (CT) scans to estimate the physical parameters of the skull. CT scans use a number of different x-ray measurements taken at different angles to create cross section images of the object of interest. Areas with a higher radiodensity will attenuate the x-ray beam more. CT data is generally presented in Hounsfield units (HU), where higher HU indicates greater density.

Hounsfield units scale such that air is -1000 HU, water is 0 HU, and bone is generally around 1000 HU.

CT data in HU can be converted into parameters of interest for acoustic simulations (density, speed of sound) and these parameter maps are then used in the acoustic simulation. Aubry et al present a set of equations to estimate the porosity from CT data and then calculate parameter maps from this porosity map

$$\Phi = 1 - \frac{HU}{1000} \qquad \text{Eq. 2.2}$$

where Φ is the porosity and HU is the Hounsfield units for a voxel. Acoustic parameter maps then follow

$$\rho = \rho_{water}\Phi + \rho_{bone}(1 - \Phi) \qquad \text{Eq. 2.3}$$

$$c = c_{water} + (c_{max} - c_{water})(1 - \Phi) \qquad \text{Eq. 2.4}$$

where ρ_{water} is the density of water, ρ_{bone} is the maximum expected bone density, c_{water} is the speed of sound in water, and c_{max} is the maximum expected speed of sound in bone [99].

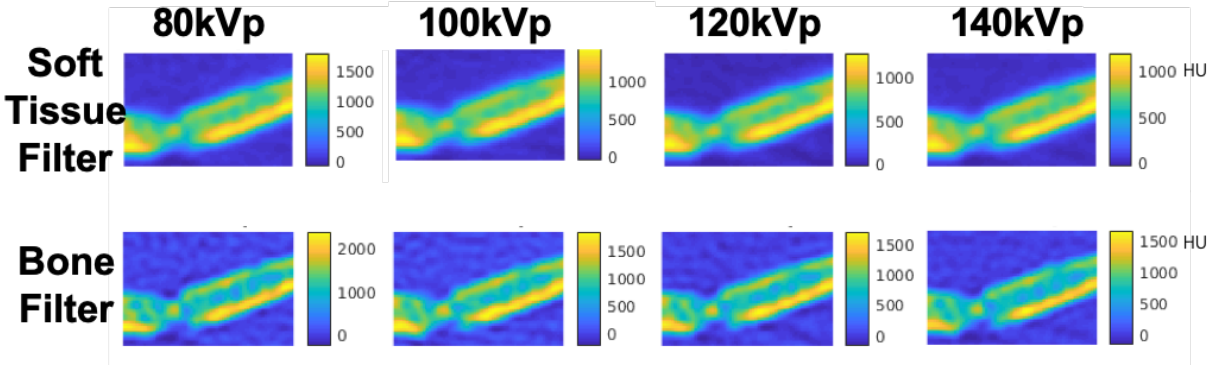

Figure 2.1: Example of CT images of an ex vivo skull sample with different energies and reconstruction filters. The Hounsfield units for a given voxel can vary based on the these factors. Note the changing color bars with larger HU values for lower energies and when comparing the bone filter to the soft tissue filter at the same energy.

These equations provide an estimate of the acoustic parameters of interest but there can be variation based on how the CT data is acquired. The measured HU of a sample can vary based on scanner type, x-ray tube energy, and reconstruction filter [100]. An example of these variations can be seen in figure 2.1 where the same CT scanner was used to acquire images of an *ex vivo* skull at four different x-ray energies and these data were reconstructed with two different filters. In a region of the skull the measured HU decrease with increasing x-ray energy. The measured values also change when the reconstruction filter is changed with a bone reconstruction filter resulting in larger HU in the skull and more noise compared to the soft tissue filter (figure 2.1).

Similar methods using CT data to calculate physical and acoustic parameters have been described in other papers with small variations. These different methods can result in speed of sound estimates that vary by 100s of meters per second for bone and the estimates are dependent on the x-ray energy [100]. Accounting for the x-ray energy is important to improve the accuracy of the conversion of HU to speed of sound but experimental findings suggest that some of the variation in speed of sound is not explained by HU changes [100]. A comparison of simulations with homogenous acoustic parameters in the skull and CT derived values found significant shifts in pressure and focal location for only some skull geometries suggesting the variations in parameters will not always cause noticeable shift in the simulation results [101]. Ultrashort echo time (UTE) MR imaging has been used to estimate parameters for FUS treatments by converting the UTE data into virtual CTs for simulations. Aberration correction was tested using UTE on *ex vivo* bone samples and was able to improve the transcranial focus [102]. Pressure and thermal simulations using CT and UTE images for a thermal therapy

resulted in similar results for both imaging modalities [103]. Further validation of UTE is needed before it can replace CT imaging for simulation parameters, but the lack of need for ionizing radiation and the ability to perform all the scan on a single scanner for MR guided procedures make UTE a promising method.

2.2—US measurement and localization

In order to apply focused ultrasound through the skull it is important to be able to estimate the transcranial pressure field. Challenges in directly measuring the pressure *in vivo* necessitate methods for estimating the transmitted pressure distribution and for measuring effects of the pressure. Laboratory measurements can be made with hydrophones to assess the pressure output and distributions in water tanks in the free field or though *ex vivo* samples. Simulations can be used to estimate the pressure in more complex tissues as described above, these simulations often use laboratory measurements as an accuracy check. Finally, experimental data can be collected using imaging methods to assess the effects of the FUS such as heating or displacement. MRI is widely used with transcranial FUS as it provides the ability to images heating due to thermal deposition or displacement from the acoustic radiation force.

2.2.1—Hydrophone based calibration

It is important to know the ultrasound pressure for transcranial applications. The pressure at the focus can be measured in a water bath giving the free field pressure of the beam. This measurement is made using hydrophones which convert pressure changes at the sensing area to a voltage signal which can be measured on an oscilloscope. The work in this

document uses two types of hydrophones: a ceramic needle hydrophone (HNC-0400, ONDA, Sunnyvale, CA, USA) and a fiber optic hydrophone system (FOH, Precision Acoustics, Dorchester, UK). The measurement of the pressure is made by aiming the transducer into a water tank and placing the hydrophone at the focus with its sensing element facing the transducer. The hydrophone is moved the focus location with a three-axis stage by maximizing the hydrophone signal. The output of hydrophone is measured with an oscilloscope that is synced with the transducer. A series of driving amplitudes are used to sonicate and the voltage at the focal location is measured. These measurements are then fit to line to estimate the receive voltage at given driving amplitude or the reverse. Calibration files are provided by the manufacturer to convert the measured voltage to pressure based on the frequency dependent sensitivity of the hydrophone being used. The driving amplitude needed to generate any specific pressure can thus be known.

The ceramic needle hydrophone sensing element is a small piezoelectric element (0.4mm diameter) which acts as a transducer as previously described in section 1.2. When a pressure change occurs at sensing element, the sensing element changes size which causes an electrical signal to be generated. This electrical signal can then be detected and converted to a pressure measurement. The fiber optic hydrophone sensing element consists of a thin polymer spacer between two mirrors. A laser is incident on these mirrors and with interferometry the optical thickness of this polymer spacer can be measured. Pressure and temperature changes can be estimated by measuring the change in the thickness of this polymer spacer [104].

The uncertainty in hydrophone measurements comes from multiple sources but the largest contributor is the uncertainty in the calibration. Each of these hydrophones used in this

work have a different error reported by the manufacturer. As part of a neuromodulation study where consistent pressure estimates were required [10], [65], repeated measurements of a transducer output were taken with the ceramic hydrophone to estimate the pressure. Four measurements taken over a span of more than a year found the driving voltage to achieve 425 kPa to be 66.95 mVpp with a standard deviation of 0.51 mVpp. This represents very consistent measurements over time and provides a good estimate of relative pressure increase with increasing driving voltage. However, the uncertainty in the conversion factor from hydrophone receive voltage to pressure at the frequency in use was 3 dB for this hydrophone. This uncertainty results in a pressure range from 301 kPa to 600 kPa. Using measurements from the optical hydrophone for this driving voltage results in a pressure estimate of 516 kPa. The fiber optic hydrophone has a manufacturer reported uncertainty of $\pm$9% resulting in a pressure range of 470 kPa to 562 kPa (see the appendix A of [65]). While the fiber optic hydrophone system has a lower calibration uncertainty and is able to measure larger pressure amplitudes providing important data for safety studies, it is also important to use consistent pressure estimates when performing experiments.

2.2.2—Image guidance and feedback

Image guidance of FUS procedures is necessary to accurately target specific regions for treatment and often is used to assess treatment. Most image guidance for FUS procedures is performed with ultrasound or MR imaging. For transcranial applications of FUS MR guidance is most common and is what is used in this work. MRI measures the interaction between atomic spins and magnetic fields and is most often used to image hydrogen spins in biomedical

imaging. Different MR sequences can provide contrast for a number of biologically interesting features. Both anatomical and functional imaging can be performed which provides the ability to measure functional changes in anatomically distinct brain regions. Imaging sequences can also be used to measure the effects of FUS on tissue. Image guidance is used to both locate the targets of interest during an experiment with anatomical or functional imaging and to assess the treatment by measuring the beam location and monitoring for heating or other effects.

2.2.3—MR thermometry

When a tissue is heated, the hydrogen bonds of water molecules within the tissue will be more likely to break. This results in less shielding of the magnetic field by the electrons compared to the water molecules with hydrogen bonds. Since the proton resonance frequency is dependent on the magnetic field, this increased shielding leads to a lower proton resonance frequency wherever the tissue is heated and this shift in the proton resonance frequency will scale with the amount of heating. By repeatedly imaging with a gradient echo sequence it is possible to map the phase changes induced by the changing proton resonance frequency and calculate the temperature change over time. The temperature change can be calculated as follows

$$\Delta T = \frac{\phi(T_1) - \phi(T_0)}{\gamma \alpha B_0 TE} \qquad \text{Eq. 2.5}$$

where $\phi(T_1)$ is the phase at the current time, $\phi(T_0)$ is the phase at a baseline before heating was initiated, γ is the gyromagnetic ratio, α is the proton resonance shift coefficient, B_0 is the magnetic field strength, and TE is the echo time. The proton resonance frequency shift coefficient varies little for non-fat tissues and is similar to water of -0.01ppm/C [105].

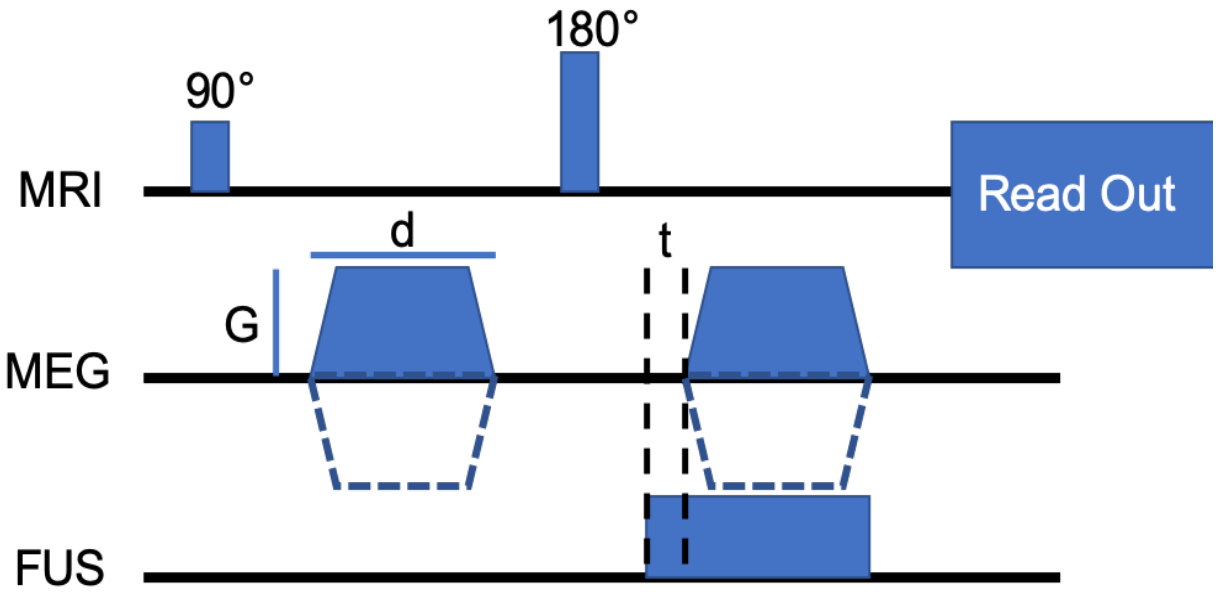

Figure 2.2: Basic MR-ARFI pulse sequence. A spin echo sequence is used and various read out work. Two motion encoding gradients are played out on either side of the 180 pulse and in line with the ultrasound propagation direction. The gradients are generally played at maximum amplitude (G) and slew rate for a fixed duration (d). The FUS pulse triggered with some delay (t) relative to one of the gradients. The displacement induced by the FUS pulse result in a phase change only in locations where the focus is located.

2.2.4—MR-ARFI

Magnetic resonance acoustic radiation force imaging (MR-ARFI) provides a method to localize the ultrasound beam by imaging direct effects of the intensity. As discussed in section 1.1.4, the force of the beam is proportional to the absorption of the tissue and the intensity of ultrasound. When this force is applied to a tissue, a micron scale displacement can be generated. These displacements, which match the intensity distribution of the beam can be imaged using ultrasound or MRI.

With MR-ARFI these small displacements can be encoded using motion encoding gradients (MEG). An example of a gradient echo MR-ARFI pulse sequence is shown in figure 2.2. These gradients are generally high strength to encode these small displacements and short duration and separation to reduce diffusion weighting in the image. When a region of tissue is displaced in the same direction as the MEG it will experience a different magnetic field compared to its rest position. Because of this different magnetic field the displaced area will accrue a different phase compared to tissue which did not displace. These measurements are then repeated with the MEGs inverted to double the phase difference. The resultant phase map can then be converted to displacement by using known values of the MEG strength and duration

$$\Delta x = \frac{\Delta \phi}{2\gamma G d} \qquad \text{Eq. 2.6}$$

where Δx is the calculated displacement, $\Delta \phi$ is the measured phase change, γ is the gyromagnetic ratio, *G* is the MEG strength, and *d* is the MEG duration [25].

Improving the sensitivity of the MR-ARFI sequence to small displacements allows less FUS energy to be used to localize the beam. The shape of the MEGs can be altered to improve the SNR of the sequence. Chen et al found that using bipolar gradients rather than unipolar gradients provides a large SNR increase for long duration MEGs [106]. The time and number of sonications required for an MR-ARFI sequence can be reduced by using fast readout methods. A single shot echo planar readout sequence was developed by Kaye et al. to rapidly detect the displacement induced by the focus [107]. Similarly, Paquin et al demonstrated a partial k-space method, keyhole acceleration, to reduce the time and FUS energy during beam localization [108].

2.3—Optical tracking

Optical tracking has been used to estimate the focus location prior to sonication. Since the focus of the FUS beam is only a few millimeters in diameter, aiming the transducer at the correct brain target can be challenging. Optical tracking provides a method to visualize the focus location on preacquired images of the brain to more accurately target specific structures. Optical tracking has been used for targeting in blood brain barrier opening in both research [57], and clinical settings [40] and in neuromodulation in large animals [10], [65], [109]. In these studies, optical tracking is used to position the transducer to the anatomical region of interest. The location of the beam was able to be measured using PCD monitoring [57] or MR-ARFI [65] in some of the studies to confirm the beam was on target.

2.3.1—General principles

Optically tracked tools are widely used in surgical areas where prior imaging can be used to allow for more accurate procedures. External tracking of tools can be used to identify the location and orientation of the tool in a tracked coordinate system which can be registered to the image coordinate system [110]. A stereovision camera system can be used with a known pattern of reflective spheres that are rigidly fixed to the tool to measure the location and orientation of the tool [110], [111]. This camera based coordinate system can be registered to the image based coordinate system using a point based registration between two sets of points in camera space ($\mathbf{x}_i$ for i = 1 to N) and image space ($\mathbf{y}_i$ for i = 1 to N) [111], [112]. A translation, $\boldsymbol{t}$, and rotation, R, are needed to align the set of camera points with the corresponding image

points. Since there is error in these measured locations, the translation and rotation will result in the two sets of points not being perfectly aligned. We want to find the translation and rotation which minimize the root mean square distance between these sets of points. This distance is referred to as the fiducial registration error (FRE), where

$$\mathrm{FRE}^2 = \frac{1}{N}\sum_{i=1}^{N} |R\boldsymbol{x_i} + \boldsymbol{t} - \boldsymbol{y_i}|^2 \qquad \text{Eq. 2.7}$$

The optimal translation can be found by

$$\mathbf{t} = \bar{\boldsymbol{y}} - R\bar{\boldsymbol{x}} \qquad \text{Eq. 2.8}$$

where the bar represents a mean from i = 1 to N [111], [112]. The optimal rotation is more difficult to calculate but a number of algorithms have been developed which are equally good at calculating R [113].

In addition to FRE two other errors are often reported with optical tracking: fiducial localization error (FLE) and target registration error (TRE). The FLE is the distance between the true point of a fiducial marker and its measured position. The TRE is the error between corresponding non-fiducial points in the two spaces. This error represents the error between the estimated tool tip location and the true tip location [111]. For focused ultrasound the TRE is the error between the predicted focus location and the measured focus location and is of most interest when localizing the beam beyond the skull.

These same methods can be applied to focused ultrasound. By optically tracking the focus of the ultrasound beam and using preacquired images it is possible to aim the transducer at targets within the brain with good accuracy. A number of transforms are needed to bring the ultrasound space into an image space where the predicted focus location can then be

visualized. This method allows the user to place the focus on the brain region of interest without applying any ultrasound energy.

2.3.2—Optically tracked methods

We can denote a location in coordinate in a given space A as ${}^{A}x$ and a transform from coordinate system A to coordinate system B by ${}^{B}T_{A}$. The inverse of the transform is the same as a transformation in the opposite direction so that ${}^{B}T_{A}^{-1} = {}^{A}T_{B}$. An optical tracker is placed on the FUS transducer and the location of this tracker can be recorded in real time. Since the goal of optical tracking is to visualize the FUS beam in a preacquired image, four spaces, the image space (I), the physical space (P), the tracker space (T) and the ultrasound space (U), and the transforms between each space are needed. We can thus use the following equation to find a coordinate in image space from a coordinate in ultrasound space

$$ {}^{I}x = {}^{I}T_{P}\,{}^{P}T_{T}\,{}^{T}T_{U}\,{}^{U}x \qquad \text{Eq. 2.9} $$

A coordinate in ultrasound space can then be found from a coordinate in image space by using the inverse transforms. Each of these transforms is measured in a different manner.

The transform from ultrasound coordinates to the tracker location, ${}^{T}T_{U}$, can be measured experimentally in a number of ways. A rod that matches the distance from the tracker to the focus and about which the tracker can be pivoted provides a basic way to associate the focus location with the tracker position [114]. This rod-based method was tested with MR thermometry and found to have a TRE of 4.4 mm. However, using the MR data to apply a bias correction, the transformation error was reduced to 1.9 mm [114]. A 3D beam map of the transducer can be transformed into image space by using optical tracking of a

hydrophone tip during the beam map and determining the transform from the transducer tracker to the hydrophone data [115]. In that study, optical tracking was used to record the hydrophone tip location and orientation simultaneously with the location and orientation of a tracker on the transducer. This data could then be used to project the beam map into image space, providing greater information about what brain regions will be sonicated compared to a single point. Using MR thermometry and MR-ARFI the TRE of this system was found to be as low as 2.4 mm [115]. A method using an optically tracked hydrophone with a steered array is presented in chapter 5.

The transform from tracker space to physical space is measured by the camera system and can be recorded on its own or passed into other software. The camera is able to image a pattern of reflective spheres and register these to a known position using equation 2.8. This registration provides and translation and rotation for the tracked tool. Finally, the transform from physical to image space can be measured using objects that can be localized in both spaces. Fiducial markers that can be localized in the camera space with an optically tracked stylus and localized in a MR image are used to facilitate a point-based registration as described with equation 2.8. These two sets of coordinates can then be registered together to find the transform between the two spaces and the FRE of this transform can be measured to estimate how good the transform is.

Because the focus location is generally only known in the free field, optical tracking does not account for any aberrating effects of the skull. Indeed, even if the transducer is not coupled to the head, it will still project the focus in the image of the target which may cause the user to think it is targeted well when no sound will propagate. A follow up measurement can be

performed to assess if the beam is in the correct location using MR thermometry or MR-ARFI [114], [115]. Measurements of the accuracy of optically tracked FUS systems generally result in less than 3 mm of error. The two neuromodulation systems previously mentioned resulted in 1.9 mm [114] and 2.4 mm [115]. Two other systems developed for BBB opening and using commercial neuronavigation reported mean errors of 3.1 mm [57] and 2.3 mm [116].

Optical tracking and image guidance provide tools to accurately aim the FUS transducer at a target of interest and assess if the target is being sonicated. With the addition of accurate measurement and simulations of the beam it is possible to limit the risk of damage to tissues by localizing the beam to only the target of interest and being aware of the amount and spatial distribution of FUS energy within the head. Beyond safety, it is important to understand this distribution of energy to analyze the results of experiments and predict treatment outcomes. The tools described in this chapter are used throughout the work in this dissertation.

Chapter 3—Considerations for Ultrasound Exposure During Transcranial MR Acoustic Radiation Force Imaging[1]

3.1—Introduction

Researches are increasingly interested in using FUS for neuromodulation [117]. FUS provides a method to noninvasively target millimeter scale regions of the brain for neuromodulation. FUS can also influence neural activity by targeted drug delivery [6], [64] or ablation of regions of the brain which contribute to disease [52]. For all of these applications of transcranial FUS it is important to accurately target the brain region of interest and to know where the focus is located during treatment.

For clinical ablation procedures, a small temperature rise is induced in the tissue [3] and its location is measured using MR thermometry [105]. However, too much heating at either the target or in an off target region, which may not be within in the image field of view, can cause damage to otherwise healthy tissue [51], [118], [119]. The brain is also known to be sensitive to temperature changes [120] and for neuromodulation studies the neurological changes induced by the targeting pulse will be mixed with any effects of the neuromodulation pulse. Optical tracking has been used to target brain regions [10], [57]. While optical tracking provides an estimate of the transducer location, it is offline and typically only overlays a free-field estimate of the transducer focus. A real-time method to visualize the acoustic focus that would not cause bioeffects or confounds would be desirable.

[1] The work described in this chapter was part of shared first author publication [91]. MAP explored the safety considerations of the FUS pulses using simulations and MR thermometry and ARFI and SVJ designed and programmed the MR-ARFI sequence.

MR-ARFI is a promising method of localizing the FUS beam for neuromodulation. MR-ARFI uses motion encoding gradients (MEG) to image the displacement induced by the FUS beam [25]. These displacements are caused by the acoustic radiation force acting on the tissue. Since the acoustic radiation force is proportional to the intensity of the FUS the displacement maps generated by MR-ARFI provide an accurate map of the FUS location within the brain. MR-ARFI has been shown beyond an *ex vivo* human skull [121] allowing the beam location to be measured for transcranial applications of FUS.

An ideal targeting and visualization method for transcranial FUS would not cause any bioeffects at the target or in off target areas. There are two major sources of potential damage with ultrasound: heating and cavitation [122]. As an ultrasound wave moves though tissue some of the energy is absorbed and converted to heat (see section 1.3.2). The amount of heating depends on the ultrasound parameters used and the tissue type. The attenuation coefficient of the skull (up to 20 dB/cm/MHz) is much larger than the attenuation coefficient of brain tissue (approximately 0.6 dB/cm/MHz) [15]. The rarefaction of FUS waves can also cause cavitation in tissues where bubbles are formed and collapse and these bubble collapses can damage tissue. For these reasons it is important to limit the FUS energy as much as possible to minimize potential damage or off target effects of the ARFI targeting pulse.

As part of a larger project studying the effects of FUS on the tactile circuit in a NHP [10], MR-ARFI methods were developed and the safety of the FUS pulses was studied. Simulations were used to estimate the pressure and heating during MR-ARFI sonication pulses and MR thermometry measurements were made during *in vivo* sonications to assess safety. The *in vivo* displacement was measured at decreasing FUS pressures to determine the lowest energy

needed for localization. By analyzing thermal deposition and pressure and comparing with observations made with MRI, our study highlights important parameters to consider to minimize bioeffects when mapping ultrasound beams with MR-ARFI.

3.2—Methods

3.2.1—Pressure estimates

A spherical cap single element transducer (Sonic Concepts H115MR) was used for all experiments. The radius of curvature is 63.2 mm and the aperture is 64 mm. The transducers center frequency is 250 kHz and was operated at its third harmonic of 802 kHz. The transducer was placed in a 3D printed coupling cone which could be filled with water and had a 3 cm aperture. Acoustic measurements were made with a needle hydrophone (HNC 0400, Onda Corp., Sunnyvale CA). The free-field pressure from the FUS transducer was measured for a series of input voltages up to a MI of 1.2 and a calibration curve was determined from this data set which was used to estimate pressures used for simulations and MR-ARFI.

An *ex vivo* skull fragment was used to estimate pressure loss due to the skull. The skull fragment is approximately 7 × 6 × 3 cm in dimension with a thickness between 2 and 3 mm and is from the top of the skull. The fragment was placed in degassed water for 24 hours prior to the measurements to rehydrate the fragment. The FUS transducer was coupled to the side of a water tank through a thin plastic acoustic window, and the needle hydrophone's voltage was recorded with the transducer driven at 802 kHz. To account for variations in thickness and incident angle the pressure during transcranial sonications was measured at the free-field focal location for five different placements of the skull. The transmission percentage was taken to be

the ratio of pressure measured with and without the skull present. This transmission percentage was used to derate our free field pressure values to estimate the focal pressure within the brain for *in vivo* studies.

3.2.2—Pressure and thermal simulation

The k-Wave package [93], [94] was used to model the NHP skull fragment surrounded by brain tissue for pressure and thermal simulations. The skull fragment was placed in degassed water for 48 hours to rehydrate and then embedded in 1% agar. A CT scan of the NHP skull fragment was acquired on a clinical PET/CT scanner (Philips Vereos PET/CT, Philips Healthcare, Best, NL). The scans were collected at 140 kVp and 300 mAs and with an in-plane resolution of 0.19×0.19 mm and a slice thickness of 0.67 mm. The data were reconstructed with soft tissue (filter type 'B') and bone (filter type 'YC') filters and the reconstructions were in HU. For simulations, the image volume was resampled to isotropic 0.3 mm voxels using the imresize3 function in MATLAB (Mathworks, Natick, MA, USA).

The dynamic range of the CT data was compressed so that the resulting speed of sound and density maps better resembled previously reported values. To determine the high range of data A 400 bin histogram (the bin size was approximately 7 HU but varied depending on initial HU minimum and maximum values) was generated. The HU value from the highest bin with at least 500 voxels was set to be the maximum HU for the skull. The CT data was then compressed so that all values below 0 HU were mapped to 0 HU and all values above the maximum threshold were remapped to that value (1632 HU for the bone reconstruction filter). The soft tissue filter was used to generate a mask of the skull fragment. This mask was used to generate

the parameter maps for acoustic absorption, thermal conductivity, and specific heat in the simulations (table 3.1). The bone filter reconstruction data was used to generate the parameter maps for speed of sound and density using a method similar to Aubry et al. [99]. The porosity was estimated for each voxel as $\varphi_i = 1 - (HU_i/\max(HU_{volume}))$. This value was then used to calculate a speed of sound and density for each voxel $\rho_i = \varphi*\rho_{water} + (1 - \varphi)*\rho_{bone}$; $c_i = (c_{Max} - c_{Min})*(1 - \varphi) + c_{Min}$ where $\rho_{water} = 1000\ kg/m^3$, $\rho_{bone} = 2100\ kg/m^3$, $c_{min} = 1500\ m/s^1$, and $c_{max} = 2900\ m/s^1$. All grids representing the propagating medium were padded to a grid size of [Nx,Ny,Nz] = [300,280,280].

Table 3.1: Tissue properties used in the simulation grid

Parameter	Skull	Non-skull
Absorption (dB/cm/MHz)	8	0.4
Thermal Conductivity (W/m/K)	0.3	0.5
Specific Heat (J/kg/K)	1700	3600

The H115MR single element transducer was modeled in k-Wave so that the geometric focus was approximately 1cm past the inner surface of the skull fragment. The simulations shown in this chapter were computed retrospectively after acquiring *in vivo* data. An 80-cycle pulse was used as the input source for the transducer and the amplitude was set so that a free-field simulation resulted in the same pressure that was estimated for *in vivo* (methods described below). An additional pressure simulation was performed to compare our simulation results with our water tank measurements behind the skull fragment. For this simulation the

free field pressure was matched to the measured free field pressure in the water tank (284 kPa) and then a simulation was performed through the skull to simulate the transmission loss in a water tank. A GPU-accelerated 3D k-Wave simulation was run on a workstation PC (HP Z820, Xeon E5, with 256 GB RAM, Hewlett Packard, Palo Alto, CA) with a 16 GB Nvidia Titan GPU (Nvidia, Santa Clara, CA). The maximum pressure was recorded for every voxel in the simulation grid.

Thermal simulations were performed using the k-Wave package to solve Pennes' bioheat equation. The maximum pressure from the pressure simulation and acoustic absorption were used as the volume rate of heat deposition for each voxel. Due to computation constraints the thermal simulations were only performed in a region around the focus that constrained the part of the skull fragment that experienced the highest pressure. The thermal simulation grid size was [Nx,Ny,Nz] = [140,80,80] with 0.3 mm spacing in all dimensions. The heat source was turned on and off to simulate the FUS pulses used for MR-ARFI with 4.5 ms pulses with a 1 Hz PRF. A time step of 0.1 ms was used during the 4.5 ms ARFI pulses, while a longer time step of 5 ms was used during the "off" periods to ensure feasible computation time. 100 sonications were simulated and the temperature was recorded at each point in the grid for each time point.

3.2.3—MR imaging

MR thermometry was used to measure heating *in vivo* during MR-ARFI pulses. Sonications consisted of 4.5 ms pulses repeated at 1 Hz. A gradient recalled echo sequence was used with a FOV of 10 cm by 10 cm, 2 mm isotropic voxels, 5 slices that were 2 mm thick, and

TE/TR 10/25 ms was used. The phase data were converted to temperature change with the follow equation

$$\Delta T = \frac{\phi(T_1) - \phi(T_0)}{\gamma \alpha B_0 TE} \quad \text{Eq. 3.1}$$

where $\phi(T_1)$ is the phase at the current time, $\phi(T_0)$ is the phase at a baseline before heating was initiated, γ is the gyromagnetic ratio, α is the PRF shift coefficient, B_0 is the magnetic field strength , and TE is the echo time [105]. Two regions of interest were selected, one around the focal location and one in the muscle above the skull to estimate skull heating.

To minimize the necessary energy to detect displacement signal the MEGs of the MR-ARFI sequence could be rotated to match the transducer using optical tracking information (for more detail this sequence worked see chapter 4 of [123]). A phantom was constructed to allow for rotation of the FUS transducer during MR-ARFI scans (figure 3.1). The phantom was a graphite-agar combination (4%/1% mass per volume) which displaced during MR-ARFI sonications. This phantom was physically connected to the coupling cone of the transducer which was filled with a 1% agar gel and a 6cm surface coil was positioned at the end of the

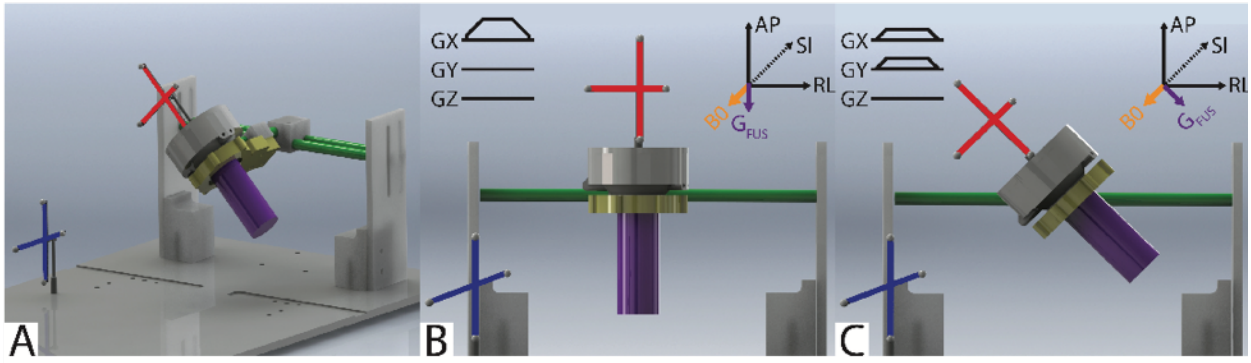

Figure 3.1: The phantom experiment allowed the transducer to be rotated relative the magnet coordinate system. The MEGs could be rotated to align with the beam propagation direction to measure the displacement at different MEG orientations.

coupling cone around the phantom. MR-ARFI images were collected with the MEGs aligned in each axis of the magnet coordinate system and in the transducer direction as measured by optical tracking.

MR-ARFI images were collected with a FOV of 12 cm by 12 cm, 2 mm isotropic voxels, a single 2mm thick slice, and TE/TR of 17/1000 ms. The MEG were 3ms in duration with the scanners maximum gradient strength of 40 mT/m and a 4.5 ms FUS pulse was triggered 2 ms before the MEG. Four sets of phase images were collected to reconstruct the ARFI image, $\phi^{+}_{FUS\ on}$, $\phi^{+}_{FUS\ off}$, $\phi^{-}_{FUS\ on}$, and $\phi^{-}_{FUS\ off}$ where the + and – refer to the polarity of the MEG. Displacement maps could be measured from these phase images by complex phase subtraction $\Delta x = \phi^{+}_{FUS\ on} \cdot (\phi^{-}_{FUS\ on})^{*} \cdot (\phi^{+}_{FUS\ off} \cdot (\phi^{-}_{FUS\ off})^{*})^{*})/2\gamma Gt$ where γ is the gyromagnetic ratio, G is the gradient strength, and t is the gradient duration.

3.2.4—*In vivo* imaging

In vivo MR-ARFI was performed on two healthy adult macaque monkeys (M fascicularis) with the approval of the Institutional Animal Care and Use Committee (IACUC) at Vanderbilt University and in accordance with all relevant guidelines and regulations. The NHP was initially sedated with ketamine hydrochloride (10 mg/kg) and atropine sulfate (0.05 mg/kg) and then anesthetized with isoflurane (1.0–1.5%) delivered over oxygen. After intubation, the animal was secured by ear bars, eye bars and a mouthpiece in a custom-designed MR stereotaxic frame. A 2.5% dextrose in saline solution was infused intravenously (3 ml/kg/h) to prevent dehydration during the scans. Animals were artificially ventilated throughout the experiment. Temperature was maintained by a water circulating blanket. Heart rate and peripheral capillary oxygen

saturation (SpO2; Nonin), respiration pattern and end-tidal CO2 (24–32 mmHg; SurgiVet) were continuously monitored and maintained during the entire scan period. The transducer was aimed at the somatosensory cortex, a target which was part of an ongoing neuromodulation experiment [10], [65]. Two experiments were performed to assess reduced energy, a set of rotated MEG gradients (aligned by optical tracking, 45° off, and 90° off) for an *in vivo* test of the MEG rotational response and a set of three different sonication pressures (free field PNPs of 1.68, 2.25, and 2.81 MPa) were used to test how much energy is needed to detect the focus.

3.3—Results

3.3.1—Transducer output and simulations

The output of the FUS transducer was measured with and without the *ex vivo* skull fragment in the beam path the characterize the attenuation of the beam due to the skull. The mean detected pressure at 802 kHz in a water tank was 284 kPa (free-field) and 91 kPa (skull

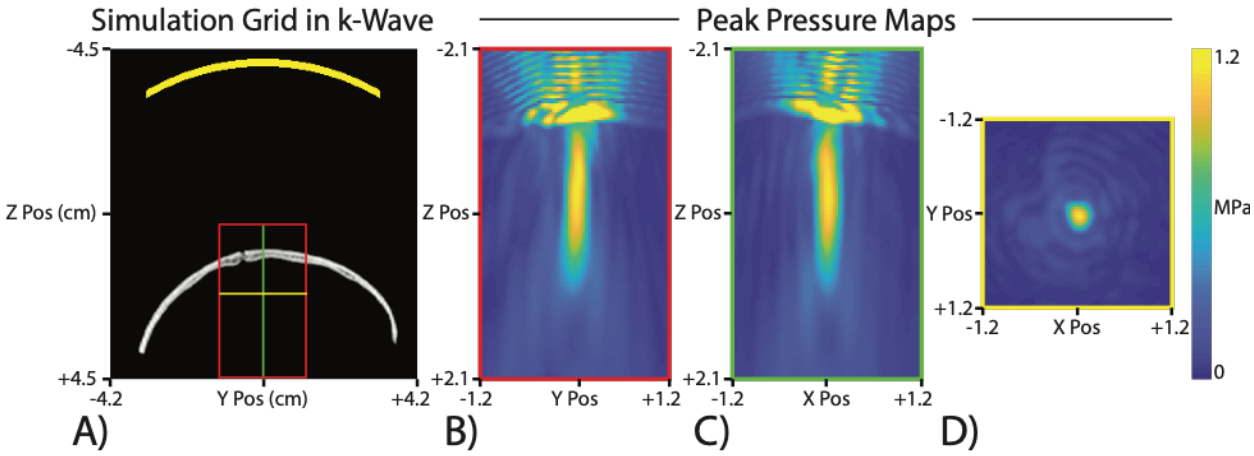

Figure 3.2: Pressure simulations with and ex vivo NHP skull fragment. (A) The simulation grid showing a CT of the NHP skull fragment, the transducer position at the top in yellow, and the three axis view through the focus location where thermal simulations where performed. (B-D) Peak pressure maps around the focus in three views. The highest pressure in the simulations was inside the skull but the pressure maps are scaled to better show the focus.

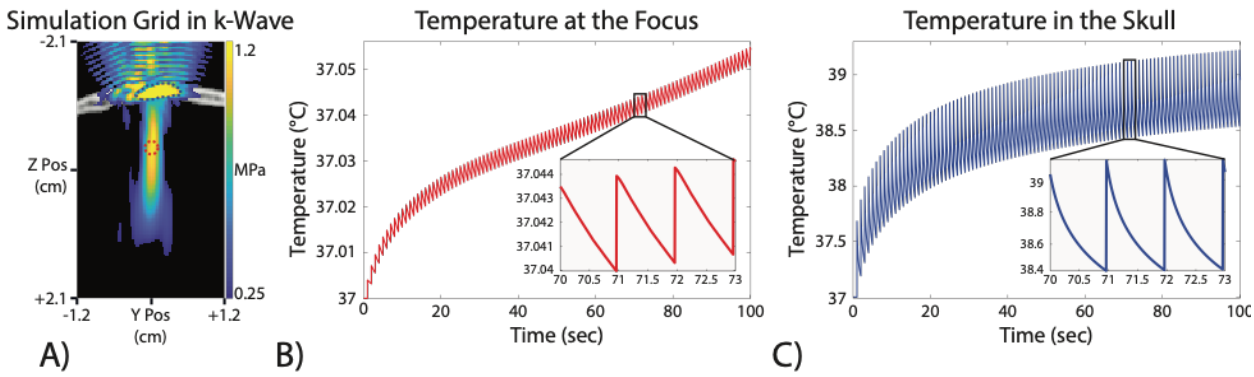

Figure 3.4: Thermal simulation of 100 MR-ARFI sonications. (A) The simulations grid showing a pressure simulations overlaid onto the NHP skull fragment CT. The red ROI shows the approximate area of maximum heating at the focus and the blue area shows the maximum heating area within the skull. (B) The simulated temperature rise at the focus was less then 0.1C . (C) The temperature rise within the skull was approximately 2C. The heating from the skull can also spread to the outer regions of the brain.

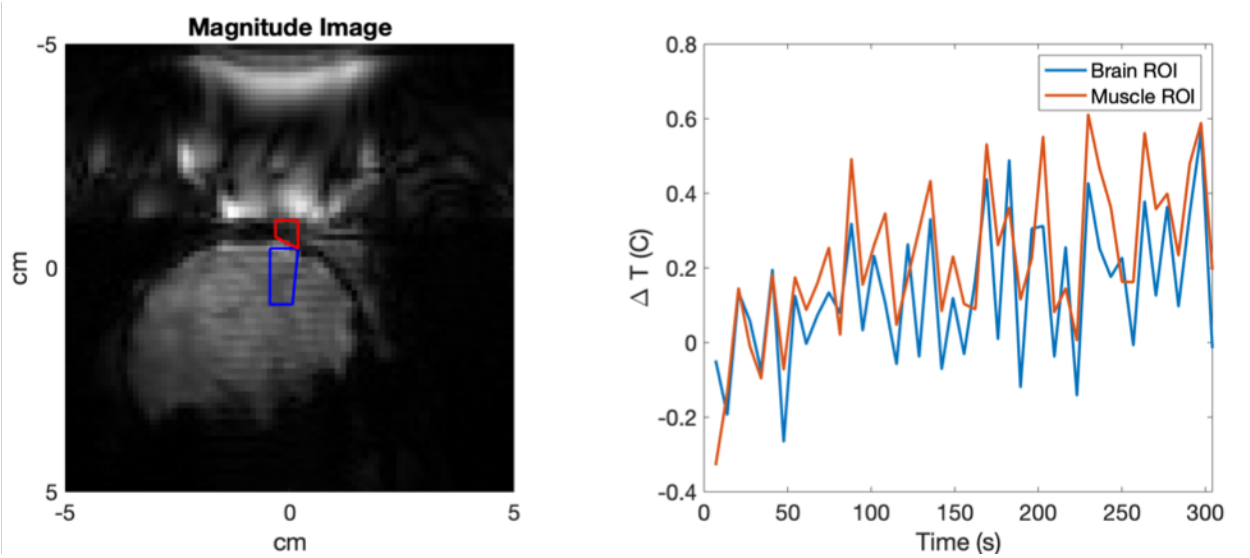

Figure 3.3: Temperature rise in vivo during 300s of a MR ARFI FUS pulse. A FUS pulse was applied at 1Hz and the temperature in the brain and in the muscle above the skull where measured with MR thermometry. Similar small temperature rises were seen in both the muscle and the brain.

fragment present). With the skull fragment, 32.1% of the free-field pressure was transmitted to the same location beyond the skull. Simulations matched to these water tank experiments resulted in a free field simulated pressure of 284 kPa and transcranial pressure of 118.5 kPa. This simulation showed 41.73% transmission through the *ex vivo* skull fragment. Simulations of

the same FUS pulses used during subsequent MR-ARFI showed a maximum pressure at the target in the brain of 1.14 MPa and a maximum pressure in the skull of 3.19 MPa (figure 3.2, note the color map is scaled to emphasize the focus in the brain).

Thermal simulations showed that the skull, which absorbs more sound than brain tissue and experienced the highest pressure, had the largest thermal rise with only modest temperature increases in the brain (figure 3.3). A 100-sonication simulation of an ARFI pulse resulted in a maximum heating in the skull of 2.22 °C and a maximum heating at the target of 0.05 °C. The heating in the skull approached a steady state; however, at the focus, the heating did not appear to be in a steady state.

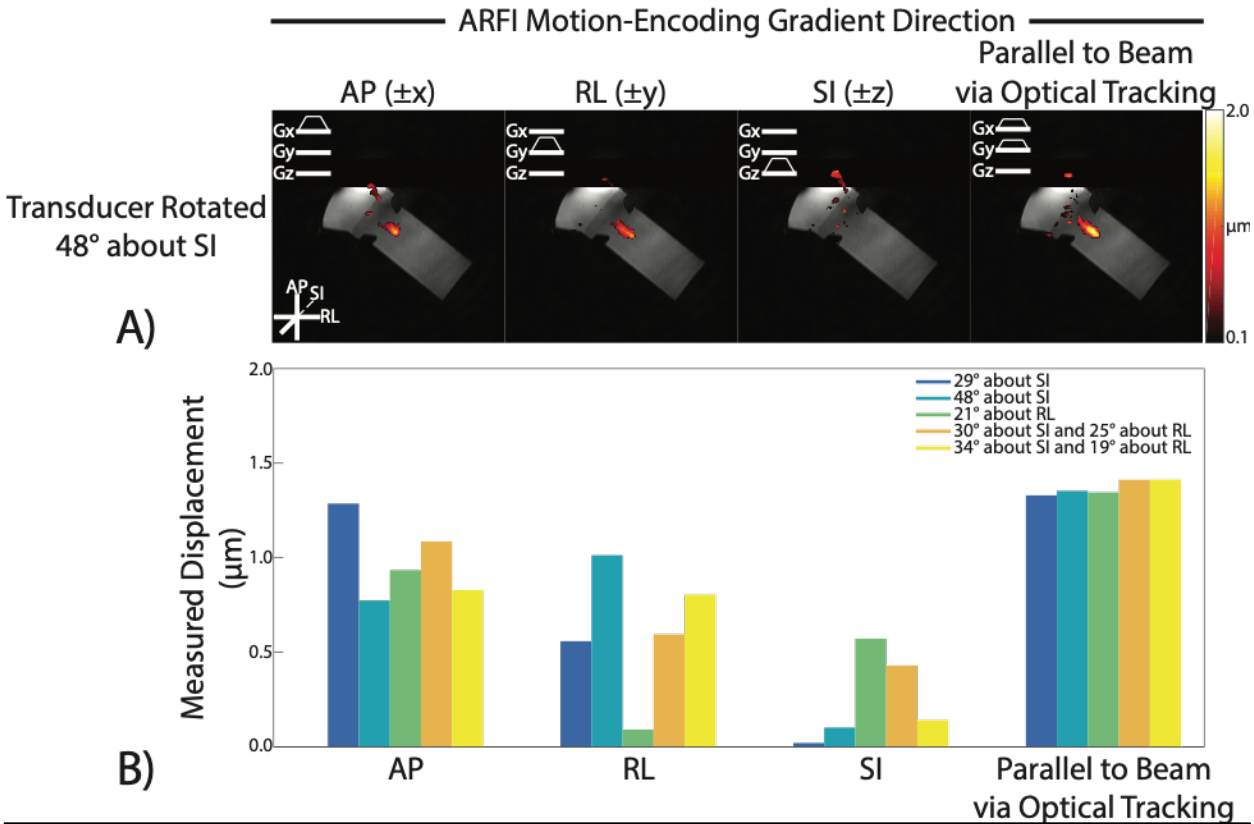

Figure 3.5: Top: An example of a single rotation of the phantom experiment showing the displacement maps generated with the MEGs aligned in the three magnet coordinates and with the optically tracked beam direction. Bottom: The maximum displacement was detected when the MEGs were aligned with the beam propagation direction.

3.3.2—*In vivo* imaging

In vivo MR thermometry showed similar, minor heating in the muscle above the skull and the focal area in the brain of approximately 0.3 °C (figure 3.3). These measurements do not represent the true skull heating since there is not enough MR signal from the skull and each ROI contains tissue that is near the skull from which heat can spread into the tissue.

In phantom scans MR-ARFI scans with different MEG angles the maximum signal was detected when the MEG align with the transducer beam propagation direction. Figure 3.5 shows average displacement over a 3x3 voxel region of interest at the focus location for 5 different transducer angulations with different MEG orientations. When measuring along the magnet coordinate system, the signal is maximized when the transducer is aligned with one of the magnet coordinate system directions. However, when the MEG are correctly aligned with the beam directions the full displacement is measured in all cases allowing less pressure to be used when forming MR-ARFI images. This was confirmed *in vivo* by acquiring displacement maps with the MEG at different orientations (figure 3.5). When the MEGs are rotated 90° from the beam direction no focus can be detected. As the MEGs are brought into alignment with the beam direction a larger signal is detected.

Figure 3.6 shows a pressure vs displacement curve for MR-ARFI maps. Since one of the major sources of risk is cavitation, and this risk scales with PNP, finding a minimal pressure to reliably localize the focus is important. Using a free field PNP of 1.68 MPa, corresponding to an estimated *in vivo* PNP after skull transmission of 0.54 MPa, the focus could still be identified.

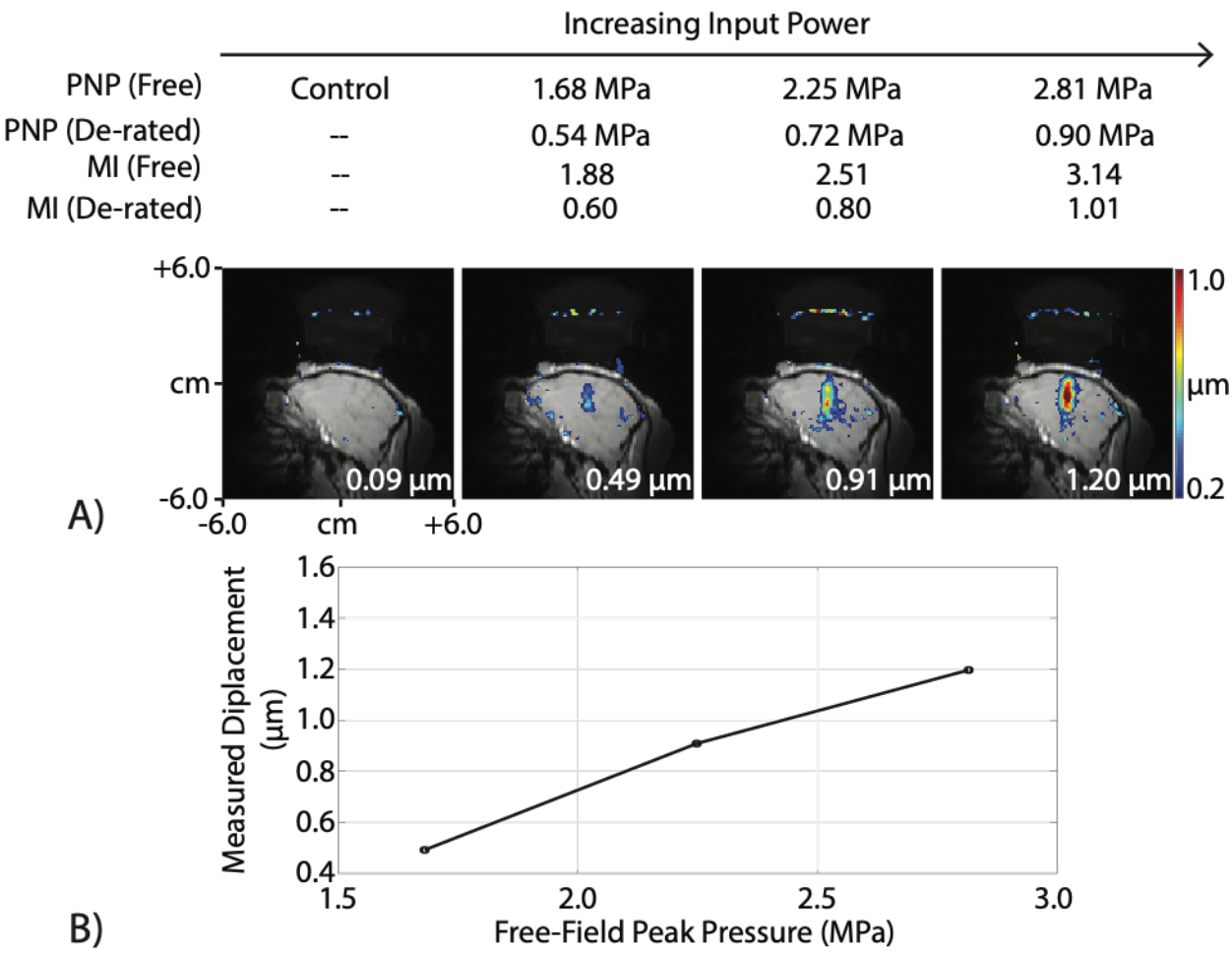

Figure 3.6: A: Displacement maps for increasing free field pressure sonications. Higher pressure sonications result in an easier to detect focus. B: The measured displacement increases with increasing PNP. Displacements were detectable with free field pressures that correspond to an MI below the highest acceptable FDA limits for diagnostic ultrasound.

This pressure corresponds to a MI of 1.88 which is within the highest limits allowed by the FDA for ultrasound imaging [12], [46].

3.4—Discussion

Simulations and *in vivo* measurement were used to identified FUS parameters that can be used to transcranially induce displacements in brain tissue that can be measured by MR-ARFI. Using these parameters, displacement maps were measured in living macaque brains to

localize the focus of the transducer safely and accurately. Much prior work has established MR-ARFI in phantoms [25]; this study demonstrates transcranial MR-ARFI in a survival imaging session in the brain of a large animal with intact skull with surrounding tissues of skin, soft tissue, and muscle without measurable negative bioeffects. This work shows the importance of parameter selection during the design of transcranial MR-ARFI protocols.

A low duty was used to avoid heating that could lead to adverse bioeffects in the brain, the skull, and the scalp. Heating was minimized by using the lowest FUS intensity needed to generate detectable displacement and separating the FUS pulses in time by lengthening MR repetition time to 1 second (overall duty cycle of 0.23%). The TR only needs to be short enough to acquire a large enough field of view to localize the focus. While tissue damage is known to occur with large temperature changes it is possible that even small temperature changes in the brain can temporally change neurological function, which could confound the results of a neuromodulation studies [120]. In both simulation and *in vivo* measurements we showed only small changes in temperature at the focus with our FUS pulses. *In vivo* MR thermometry is not able to directly measure temperature changes within the skull where simulations showed the largest temperature increase. By careful consideration of duty cycle and FUS intensity it is possible to localize the FUS beam with MR-ARFI with minimal heating.

In addition to the TR of the MR-ARFI sequence, other MR methods can be applied to reduce the needed risk of damage when localizing the focus. Improvements to the SNR of the sequence will allow for detection of smaller displacements that are generated with lower energy. Bipolar gradients have been shown to improve the phase images which are used to generate the displacement maps resulting in a more sensitive sequence [106]. Single shot EPI

read out has been used which can minimize the number of sonications needed to generate an image [107].

The Food and Drug Administration (FDA) mandates safety limits on the acoustic output levels of clinical ultrasound transducers to minimize the risk to thermal bioeffects [12]. The I_{SPTA}, which gauges the likelihood of heating, should not exceed 720 mW/cm^2. Although this metrics was designed around imaging transducers and pulses, it provides a basic guideline for MR-ARFI pulses as well. The pulses used in this work is lower than this limit for diagnostic imaging while still localizing the beam. This safety parameter combined with our simulations and the minimal heating measured with MR thermometry shows that heating from ARFI pulses can be reduced to a negligible amount while generating high quality images of the beam location.

A second potential source of damage from FUS is cavitation. While the FUS pulses used for MR-ARFI showed minimal heating there was high PNP present in and above the skull in simulations. Cavitation is the process of bubble forming from small nuclei during the rarefaction phase of the wave. These bubble can then collapse during the compression phase of the wave and generated forces which can damage tissue [124]. Cavitation is a stochastic process that is difficult to predict, since it depends on many conditions such as the presence of cavitation nuclei, frequency, and pressure [44]. The probability of cavitation occurring is proportional to the PNP and inversely proportional to the frequency of the FUS [43]. The MI is used to estimate the likelihood of cavitation and for imaging pulses is limited to a maximum of 1.9 [12], [46]. Most safety studies have been performed using imaging pulses which are at higher frequency and shorter duration then the pulses used for MR-ARFI. The MI within the brain for the pulses used in this work were within the safety limit but the free field MI and simulations showed an

MI above the safety limit. The pressure needed to acquire a similar displacement magnitude in both phantoms and *in vivo* was reduced by aligning the MEGs with the beam propagation direction.

The simulations of the FUS pulse through the skull showed pressure up to 3.2 MPa which corresponds to an MI of approximately 3.5 within the skull, suggesting that cavitation within or near the skull is a concern. Due to the voxel size of the CT used to generate the acoustic parameter maps, effects of the microstructure of the skull are not accounted for in these simulations. A prior study of FUS interactions with the microstructure of the skull show that small heterogeneities can cause multiple scattering within the skull that may reduce the PNP and reflect less uniformly than the simulations results [125]. Additionally, simulations have been shown to underestimate transmitted pressure through the skull if the simulation grid spacing is not at least 20 times the FUS wavelength due to a staircasing effect of the skull voxels [95]. While this effect is a concern, the hydrophone measurements compare well with the simulations. No evidence of cavitation was observed on the scalp of the NHP after sonications but further behavioral or post-mortem pathological analysis would improve our understanding of safety.

Other groups have also studied the safety of MR-ARFI. Ozenne et al. used a combined MR-ARFI MR thermometry pulse sequence to image the displacement induced by the focus while monitoring temperature and also simulated the pressure and temperature during these sonications [92]. This study was done at 850 kHz and reported higher free field and their simulations estimated 3.04 MPa in the brain (compared to 1.14 MPa). Ozenne et al. reported a maximum temperature rise of 0.7 °C in MR thermometry and the simulations showed the skull

having the largest temperature rise [92]. Gaur et al. performed a MR-ARFI pulses at 550 kHz in a range of *in vivo* pressures up to 3.6 MPa in sheep and performed histology [126]. The histological analysis of the sheep brain showed no signs of damage from the MR-ARFI sonications when compared to controls.

Alignment of the MEGs with beam propagation direction increased the measured displacement. By maximizing the detected signal less energy is needed when localizing the focus which reduces the risk of damage and limits possible off target effects of the localization sonication. The ability to rapidly and safely localize the FUS beam is important for applications of transcranial FUS such as neuromodulation and blood brain barrier opening. Further study of the safety of ARFI pulses is needed but the framework presented here of simulation and MR measurement for temperature risk and minimizing the amount of energy needed provides a basis for future study.

Chapter 4— Increasing Radiation Force-Induced Displacement at Matched Pressure by Reducing Effective Aperture[2]

4.1—Introduction

The previous chapter discussed a method to minimize the FUS energy needed to localize the beam with MR-ARFI by aligning the MEGs with the beam propagation direction. MR-ARFI provides a method to visualize the displacements induced by the FUS beam in the brain of a macaque [91]. Because damage and other unwanted effects can result from a localization scan, it is advantageous to limit the pressure necessary to detect the beam with MR-ARFI to reduce the likelihood of these unwanted effects. The mechanical index (MI) is used as a measure for the risk of cavitation induced damage and can be reduced by using lower PNPs. Other methods have been developed to improve the sensitivity of MR-ARFI [106] or reduce the number of sonications needed to localize the beam [107], [108]. In addition to improving the sensitivity of MR-ARFI, the transducer geometry can be changed to improve the displacement and make localization of the beam possible at lower pressures. Altered transducer geometry can be used in conjunction with methods to improve the MR sequence sensitivity to localize the beam with less energy delivered to the tissue.

Spherically focused multielement transducers are often used for transcranial FUS applications. Multielement arrays provide the ability to electronically steer the beam and correct aberrations induced by the skull by individually controlling the phase and amplitude for

[2] Portions of this chapter are adapted from reference [165].

each element. Aberration correction can reduce the focal size of the beam and increase the focal gain [33]. The transducer used in this chapter was designed for neuromodulation of the macaque somatosensory cortex and is able to steer 20 mm in the axial direction and 10 mm in the transverse direction allowing targeting of a number of brain regions from a single position [1]. The ability to electronically steer the focus with a multielement array makes safely localizing the beam even more important. Since the beam may be steered to multiple locations the energy used to localize the beam will be applied each time it is steered to assess the true location of the beam. Since each element of the transducer can be controlled individually, aspects of the transducer geometry can be altered by selectively turning elements off to create virtual transducers.

Transducer geometry affects the experiment design and pressure field characteristics. Spherical cap transducers (whether single element or multielement) can be characterized by the diameter of the aperture and the radius of curvature. The ratio of radius of curvature to the aperture diameter is the f-number of the transducer (equation 1.14). Transcranial FUS transducers can have f-numbers as low as 0.5 where the transducer is a full hemisphere that fits over the head [127]. A smaller f-number will result in a smaller focus and more focal gain but some experimental setups will not be possible since the transducer will have a larger surface area for a fixed radius of curvature which can limit what targets in the brain can be sonicated. On the other hand, transducers with larger f-numbers have been shown to have increased nonlinearities and enhanced cavitation [128], [129].

The acoustic radiation force is proportional to the attenuation of the tissue and the beam intensity [130]. Since larger f-number transducers will generate more nonlinearities a

larger force will be generated for the same FUS intensity. Modeling of the acoustic radiation force has shown increased force with increased nonlinearity as a result of the higher harmonics being absorbed by the media [131]. The maximum displacement has been shown to be proportional to the lateral focal diameter and this diameter will increase with increasing f-number [132]. Displacement can be expected to scale with f-number due to both the increased nonlinearity and the wider focus. Additionally, for a transducer with the same radius of curvature and a smaller aperture, a vector which is normal to the transducer face at the edge of the transducer will be more aligned with the beam propagation direction. The net directivity of the transducer elements will be more aligned with the measurement direction of the MEG for MR-ARFI scans.

By electronically reducing the aperture of the transducer we are able to achieve the same measured displacement for beam localization at lower focal PNP. Selectively turning off elements along the outer edge of the transducer produces a virtual transducer with the same radius of curvature but a small diameter, thus a larger f-number. These smaller virtual transducers generate more radiation force for the same PNP. In simulations, phantom experiments, and an *in vivo* test larger displacements were observed when using the same PNP. By increasing the displacement at matched PNP the beam can be localized lower PNPs with an electronically reduced aperture which corresponds to a lower MI and lower estimate of cavitation risk.

4.2—Methods

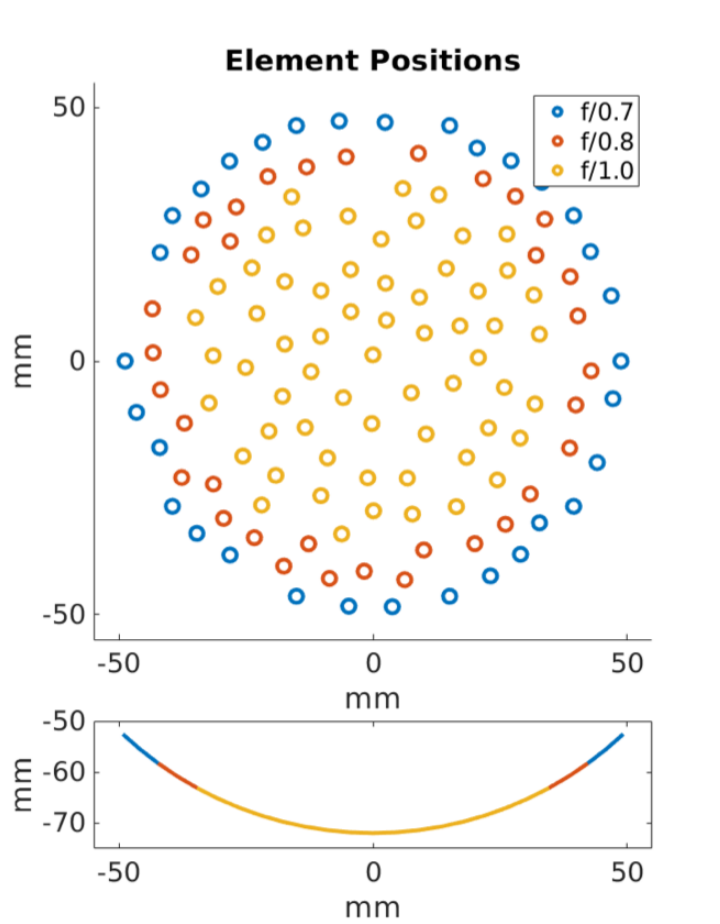

Figure 4.1: Top: Element positions on the transducer. The full array has an f-number of 0.7 and 128 elements. By electronically turning off the outside set of elements (in blue) the f-number is increased to 0.8 and by further turning off the elements in red the f-number is 1.0. Bottom: A profile of the transducer showing the decreasing aperture as element are turned off and the f-number is increased.

4.2.1—Transducer Calibration

A 128 element randomized phased array (Image Guided Therapy, Pessac, France) with a f-number of f/0.7, a radius of curvature of 7.2 cm, a diameter of 10.3 cm, and a center frequency of 650kHz was used [1]. Elements along the outer edge of the transducer were electronically inactivated so that the array could be used with f-numbers of f/1.0 and f/0.8 in addition to the full array of f/0.7 (figure 4.1). Each of these three configurations was calibrated with a fiber optic hydrophone system (Precision Acoustics, Dorset, UK) where 25 averages of a

100 cycle pulse were collected on an oscilloscope (PicoScope, Pico Technology, St Neots, UK) for a series of driving amplitudes. The measured voltages were converted to pressure using a calibration factor provided by the manufacturer. The peak negative pressure from these measurements were fit to a line to estimate the driving amplitude needed to generate a given pressure for each f-number configuration. Nonlinearity of the transmitted waveform was assessed by performing a Fourier transform on the measurement and comparing the peak amplitude at the second harmonic to the peak amplitude at the center frequency.

4.2.2—Simulations

Simulations of the three transducer f-number configurations were performed using the k-Wave Toolbox in MATLAB [93], [94]. Parameters for the 3D simulations were isotropic voxel size of 0.3mm, speed of sound of 1500 m/s, density of 1000 kg/m^3, nonlinear coefficient B/A of 7, alpha of 0.5 dB/cm/MHz, and alpha coefficient of 1.1. The transducer was modeled using the individual element locations and each f-number configuration was simulated. The transmitted signal for these simulations were planned such that the spatial peak negative pressure (PNP) for each f-number was the same by iterating the simulation until the PNP matched. A 50 cycle wave was used as the transmitted signal and the pressure for each time step (dt of 60 ns) was recorded. The PNP, PPP, and FWHM of the maximum pressure maps are reported. Similarly to the physical hydrophone measurements, a Fourier transform of each the pressure time series for each voxel was taken to compare the amplitude at the second harmonic to the center frequency.

Displacement simulations were adapted from Payne et al [26] and performed in MATLAB. The mean temporal intensity of the FUS was calculated for each voxel from the pressure simulations with the following equation $I = mean(\frac{p(t)^2}{\rho c})$ where p(t) is the pressure in each voxel for 23 cycles of the pressure wave, ρ is the density, and c is the speed of sound for the portion of the simulations after the FUS had arrived in every voxel. The acoustic radiation force can then be calculated as $F = \frac{2\alpha I}{c}$. The 3D accumulated displacement (w) induced in the beam direction (z) by the radiation force can be computed by $w = A'g(r)F$ where $A'g(r) = \frac{1}{8\pi\mu}(\frac{z^2}{r^3} + \frac{1}{r})$ and is a 3D Green's function and F is the 3D force pattern, μ is estimated to be one third of the Young's modulus assuming Poisson's ratio is 0.5. Convolving this Green's function with the force is done in frequency space. These equations assume elastostatic conditions are present which is not the case during MR-ARFI so the Green's function was weighted based on the velocity of the shear wave, $\beta = \sqrt{\frac{\mu}{\rho}}$, using a linearly decreasing function which is 1 at the center of the Green's function to 0 at a radius which equals the FUS duration times the shear wave speed. The intensity, peak displacement, and FWHM of the displacement region are reported.

4.2.3—MR-ARFI

A clinical 7T magnet (Philips Achieva 7T, Philips Healthcare, Best, NL) was used for all MR experiments. Phantom experiments were performed with a graphite agar phantom (1% agar w/v, 4% silica carbide w/v). The transducer was coupled to the top of the phantom with a water filled bubble and ultrasound gel. A MR thermometry of scan was acquired with a continuous

wave sonication for 20 seconds to localize the beam for ARFI planning. For each f-number configuration the transducer was driven at amplitudes so that the pressure at the focus would be matched as determined by the hydrophone calibration. Displacement maps were acquired in the lateral beam direction at the same location in the phantom which was centered on the hot spot found in the MR thermometry scan. A 2D spin-echo MR-ARFI sequence was used with 3ms unipolar trapezoidal motion-encoding gradients (MEG) placed before and after the refocusing pulse. The MEGs were aligned with the beam propagation direction and set to the maximum gradient strength of 40 mT/m. Images were collected perpendicular to the beam propagation direction with a 4 mm thick slice with 2 mm x 2 mm in plane voxel size with a TE/TR of 16 ms/500 ms. FUS sonications were 4.5 ms in duration and were able to generate enough displacement for beam localization with the full array.

NHP experiments were performed with approval of the Vanderbilt IUCAC. The transducer was placed above the shaved head of the NHP and coupled with a water filled bubble and ultrasound gel. The transducer was aimed at the center of the brain but not targeted to a specific region. The focus location was estimated by measuring 72 mm from the center of the transducer face and the MR-ARFI slice was planned at this location such that the long axis of the beam would be visible. MEG gradients were aligned with the FUS propagation direction. The same sequence that was used in phantoms was used with an extended TR of 1000 ms to reduce the risk of heat deposition. Sonications were performed with the full array (f/0.7) and the smallest aperture configuration (f/1.0). The full array used a 5 MPa pulse and the reduced array used a 4 MPa pulse based on a hydrophone calibration curve. Based on previous work through *ex vivo* skulls and simulations [91] we estimate 39% transmission at 650kHz which

corresponds to focal pressure in the brain of 1.95 MPa and 1.56 MPa for the two configurations.

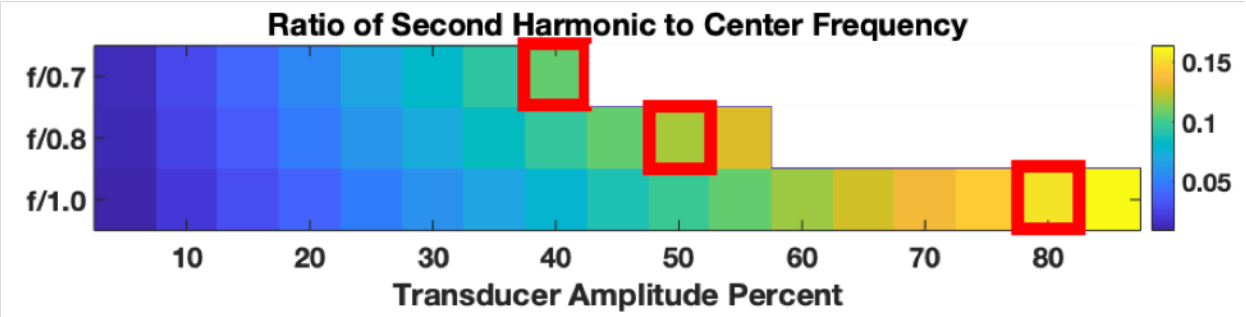

Figure 4.2: As expected at high pressure there is more harmonic content in the wave within each f-number configuration. For larger f-numbers we observed a higher ratio of harmonic content compared to the center frequency at similar pressures with the red boxes showing transducer driving amplitudes with approximately 4 MPa of pressure at the focus.

4.3—Results

4.3.1—Transducer Calibration

Calibrations of the three different f-number configurations showed that each configuration was capable of generating pressure high enough PNP that MR-ARFI was likely to be successful based on previous studies. As expected, when the outer rings of elements were inactivated, a higher driving amplitude was needed for matched pressure. As the transducer amplitude was increased the ratio of the FFT amplitude around the center frequency and the FFT amplitude around the second harmonic increased for each f-number. When comparing similar pressures across the f-number configurations an increase in this ratio is observed with increased f-number (figure 4.2).

4.3.2—Simulations

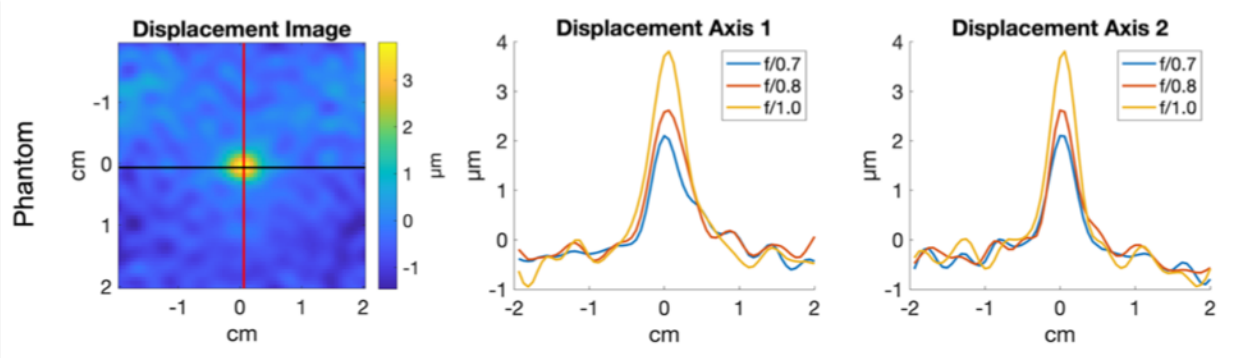

Figure 4.3: Phantom MR-ARFI displacement map showing the short axis view of the beam for f/1.0. The displacement was measured along both direction of the beam (red and black lines) and plots are shown to the right. Using pressure matched sonications, an increase in displacement is measured while using larger f-number apertures.

Results from the simulations are shown in table 4.1. Pressure simulations with matched PNP showed an increasing full width half max (FWHM) of the focus with increasing f-number leading to a larger volume were the pressure is being applied. A small shift of in the location of the focus towards the transducer of 1.8 mm was observed between the lowest and highest f-number. The peak positive pressure of the simulations increased with increasing f-number, this results in a higher intensity for the wave as well. When looking at the spectral content of the simulations an increase in the ratio of the amplitude of the second harmonic to the center frequency was observed. The displacement simulation resulted in an increased displacement with increased f-number from 3.2 µm at f/0.7 to 4.2 µm at f/0.8, and 5.9 µm at f/1.0. The displacement FWHM increased in similar proportion to the pressure FWHM.

Table 4.1: Displacement simulation results. Increased f-number resulted in larger displacement values and a larger displaced volume.

	f/0.7	**f/0.8**	**f/1.0**
PNP (MPa)	3.56	3.56	3.56
PPP (MPa)	4.11	4.27	4.57
Pressure FWHM	(8.9, 2.2, 2.2)	(11.6, 2.5, 2.4)	(17.9, 2.9, 2.8)
Intensity (W/cm^2)	476.7	491.6	525.5

Max FFT Amplitude around 650 kHz (MPa)	2.66	2.70	2.80
Max FFT Amplitude around 1300 kHz (MPa)	0.33	0.36	0.61
f2/f0	0.125	0.132	0.22
Displacement (μm)	3.2	4.1	5.9

4.3.3—MR-ARFI

Phantom MR-ARFI experiments showed an increase in measured displacement at matched pressure with increasing f-number. Displacement maps were acquired in the lateral view of the beam showing a circle of displacement in the image. The peak displacement increased with increasing f-number from 2.1 μm at f/0.7 to 3.8 μm at f/1.0 (figure 4.3). This increase is comparable to the increase in simulations. *In vivo* imaging showed similar displacement with a 20% reduction in free field pressure used when comparing f/0.7 and f/1.0 (figure 4.4). This method used less pressure to generate the same displacement at the focus.

4.4—Discussion

Localization of the FUS beam is important for therapeutic applications such as neuromodulation and drug delivery. MR-ARFI can image direct effects from the FUS beam for localization but also deposits ultrasound energy which can cause unwanted bioeffects. Methods to reduce the energy needed to localize the focus allow for safer localization and can be achieved by altering the MR sequence used for imaging or by changing the characteristics of the sonications. By electronically increasing the f-number of an array transducer, we are able to generate displacement with a peak in approximately the same region as low f-number sonications allowing for beam localization with less ultrasound energy.

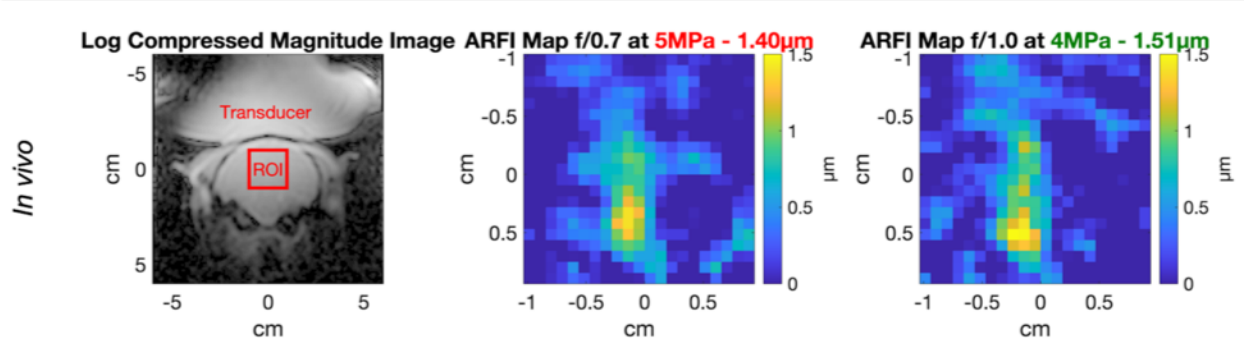

Figure 4.4: *In vivo* MR ARFI data. The magnitude image showing the positioning of the transducer over the NHP head and the region where the focus was located (left). A displacement of 1.4 µm was measured with the full array (f/0.7) using 5 MPa of free field pressure (center). With a reduced array (f/1.0), 20% less free field pressure was able to generate 1.5 µm of displacement (right).

Ultrasound can cause damage through mechanical and thermal effects. Mechanical damage can occur from cavitation. As described in section 1.3, the risk of cavitation is often assessed by the MI of the sonication. The risk of cavitation damage in diagnostic ultrasound is reduced by keeping the MI low as possible while acquiring images [42]. By using reduced aperture configurations the same displacement can be achieved with lower PNP and a lower MI. Recent work has been done on the thermal risk of MR-ARFI pulses. Simulations and MR thermometry imaging during sonications have shown that there is not significant heating that could cause damage during MR-ARFI sonications [91], [92]. Other work has performed histology to assess damage from MR-ARFI and neuromodulation sonications in two different species, sheep and NHPs [126]. This study did not find any evidence of damage to the brain that was attributed to the sonications. While these studies looked at potential damage another concern is changes to brain activity which could influence research results in any studies using brain activity as an outcome so it is important to minimize the energy needed to localize the beam.

The increase in measured displacement with reduced aperture may be due to multiple effects. By shifting power from the outer ring of elements to the more central elements the net

directivity of the elements is more aligned with the MEG direction. Because displacement occurs in the direction of sound propagation, this may result in greater displacement along the beam propagation direction. The increase in harmonic content seen in both the hydrophone experiments and simulation results may also contribute to the increase in displacement. Since the radiation force is proportional to the attenuation in the tissue [24], and attenuation is proportional to frequency [15], higher frequency content will result in a larger force being applied to the tissue. Modeling performed by Rudenko et al found an increase in the normalized radiation force with increased nonlinearity. The authors note that since the nonlinearities will be highest at the focus this increased force will be greatest at that area [131]. The pressure simulations show the expected increase in focus size when increasing the f-number and harmonics [129]. This larger pressure field will generate force over a larger volume of the tissue which may lead the greater displacement. Modeling has predicted that the maximum displacement induced by the radiation force will scale with the beam diameter [132].

A potential drawback of reducing aperture size to increase displacement is that the skull is known to strongly attenuate the FUS beam [125] and this attenuation factor will be larger for the harmonic content. The loss of energy through the skull may reduce the effectiveness of this method as the higher frequency energy will be partially filtered out by the skull. The reduction of harmonic content could explain why the phantom results show a much greater increase in displacement compared to the *in vivo* results. For a deep brain target nonlinearity can still build up inside of the skull. Previous studies on thermal brain therapy found increased heating and treatment volume when nonlinear effects were modeled [22].

It is also important to note that the increased focal size with the reduced aperture of the transducer may make localization of the full array beam shape more difficult. If the brain region being targeted is small relative the reduced aperture beam size it may be difficult to determine if the focus of the full array is correctly located at that target even if the displacement map appears to overlap with target location. This beam size effect is likely to worsen if steering is used with the reduced aperture since steering the array also leads to a larger beam as well [1]. The measured displacement volume will be larger for these virtual transducers compared to the full array but the center of the displacement is not expected to have large shifts in location. Further work is needed to understand how an ARFI displacement map corresponds to the bioeffects of FUS for neuromodulation, blood brain barrier opening, and other applications.

Using electronically reduced arrays to reduce the amount of FUS energy used to localize the beam can be combined with many of the other methods currently being employed to increase the sensitivity of MR-ARFI and time needed acquire the images. In chapter 3, a method to improve the sensitivity of the MR-ARFI sequence was shown were alignment of the MEGs with the beam propagation direction improved the measured displacement allowing less energy to be used [91]. The shape and duration of the MEGs used in the sequence can have a significant impact on displacement SNR with bipolar gradients providing better SNR for long gradients [106]. This improvement in SNR allows for detection of smaller displacements which can be generated with less FUS energy. Methods have also been developed to reduce the total number of sonications needed to acquire a MR-ARFI image such as keyhole acceleration [108] and different k-space trajectories like single shot EPI [107] or a spiral readout [133]. By reducing

the total number of sonication along with lower pressure per sonication the overall safety will be further improved.

Reducing the aperture of a transcranial transducer can improve the quality of MR-ARFI images at the matched pressure. Simulations and hydrophone data show increased harmonic content with increased f-number allowing for a larger radiation force. The smaller aperture configurations of the transducer are able to generate more displacement at the same peak negative pressure in both phantoms and *in vivo* in NHPs.

Chapter 5—Optically Tracked Steering and Correction for Transcranial Focused Ultrasound

5.1—Introduction

Transcranial FUS facilitates precise, non-invasive mechanical and thermal interaction with brain tissue. Researchers and clinicians are leveraging FUS for tissue ablation [134], drug delivery across the blood-brain barrier [135], and neuromodulation [117]. A primary technical challenge in all FUS procedures is targeting the sound to the region of interest. FUS's inherent spatial precision is the spot size of the transducer's focus which is often less than 2 mm. In practice, this precision is compromised by targeting error: the distance between the predicted focus and the actual focus. Eliminating targeting error is crucial to fully leverage the potential of FUS in procedures where spatial precision is required. In this manuscript, we present a technique that uses optical tracking combined with magnetic resonance image guidance to achieve sub-millimeter accuracy in acoustic targeting without the use of a surgically implanted frame.

Two techniques common for transcranial FUS targeting are stereotactic frames [136] and optical tracking [57], [114], [115]. Stereotactic frames, which are used in deep brain stimulation with electrodes [137], have been used to study brain function for over 100 years [138]. Clinical FUS sessions with the Insightec Exablate Neuro system [39] use a head-frame rigidly fixed to the skull of the patient. The transducer is mounted to this frame and a deformable membrane bag holds degassed water for acoustic coupling between the transducer and head of the patient [136]. This frame keeps the patient fixed in place on the treatment

table and allows the transducer to positioned and fixed in place to sonicate the region of interest. The frame requires skull screws to rigidly attach it to the skull making the procedure more invasive. This level of invasiveness is suitable for treating debilitating conditions but is overly invasive in applications such as neuromodulation where the patient may be otherwise healthy. Thus there is a need for methods to navigate the ultrasound focus to a desired target location with millimeter-scale precision, without a stereotactic frame.

Magnetic resonance imaging (MRI) can be used to directly measure effects of FUS beam for localization. MR thermometry can detect and measure the temperature change within a tissue based on the temperature dependence of MR parameters [105]. Changes to the proton resonance frequency during temperature changes is able to map *in vivo* temperature changes to an image [139]. MR thermometry requires heating the tissue which may not be suitable for all uses of FUS such as neuromodulation studies. MRI can also be used to measure displacements induced by the FUS beam in tissues with MR acoustic radiation force imaging (MR-ARFI) [25], [140]. The radiation force is proportional to the ultrasound intensity [23] so displacements induced by this force can be used to map the FUS intensity locations. Recent work to assess the safety of MR-ARFI in large animals has found non evidence of damage [91], [92], [126].

As discussed in chapter 2.3, optical tracking is a method of image guided neuronavigation that does not require rigid fixation. It is commonly used for transcranial magnetic stimulation [141]–[143] and increasingly for transcranial ultrasound [10], [57], [65], [91], [114], [115]. Optical tracking uses an infrared stereo camera to measure the position and orientation of reflective markers that can be rigidly affixed to an tool, enabling the tool's

location to be tracked in physical space [144]. In a typical workflow, fiducial markers that are visible in a 3D imaging modality, such as CT or MRI, are placed on the patient and their physical positions relative to the camera are recorded using an optically tracked stylus. The fiducials are localized in a pre-acquired image space. The two sets of fiducial locations can be used to define a rigid transform so that tools with reflective markers can be tracked in real-time and projected into the image space [145]. By placing a tracker on the transducer, the position and orientation of the transducer with respect to the patient can be estimated. This estimate allows the transducer's focus location to be overlaid on the images which provide visualization of anatomy. A primary metric for performance of such systems is the TRE, which is defined as the distance between the intended and actual target. When using optical tracking with ultrasound, studies have reported TREs of 2-3 mm [114], [115]. The TRE is a function of all aspects of the optical tracking system (fiducial localization error, operator error, among others) and 2-3 mm is close to the theoretical minimum for modern optical tracking systems. One of the main benefits of optical tracking is to avoid the need for skull screws, meaning the procedure is totally non-invasive. Additionally, by not using a frame to mount the transducer, it can be mechanically steered during procedures which increases the range of targets that can be sonicated in a single procedure [146]. Overall, optical tracking is non-invasive and the freely movable transducer has increased targeting range, but these qualities are offset by reduced accuracy.

Combining optical tracking with imaging feedback provides a basis for identifying and correcting tracking error. Here, we describe a methodology to target an ultrasound focus to a desired point in the brain under image guidance with optical tracking. We then use MR-ARFI or MR thermometry to confirm the actual focal location versus the location predicted by optical

tracking and use electronic steering of the transducer to account for the tracking error and correctly steer to targets in the surrounding area. By using the optical tracking information along with a single MRI localization scan, we can steer the FUS beam to any target in the brain within the transducer's electronic steering range and eliminate targeting error without the need for invasive stereotactic frames.

5.2—Methods

5.2.1—Coordinate Systems

For this study, an optical tracking camera (NDI Polaris Vicra, Northern Digital Inc., Waterloo, Ontario, CA) is used to track the location of the FUS transducer, and the software application 3D Slicer [147] is used to combine this tracking information with MR images using the OpenIGTLinkIF module [148]. The trackers used in this study consisted of both commercial and custom-built rigid bodies that used passive tracking spheres (Northern Digital Inc., Waterloo, Ontario, CA). Custom rigid bodies were designed following the camera manufactures guidelines. The ultimate goal of the tracking system is to know the transducer coordinates relative to an anatomical image. This requires the consideration of four coordinate systems: the

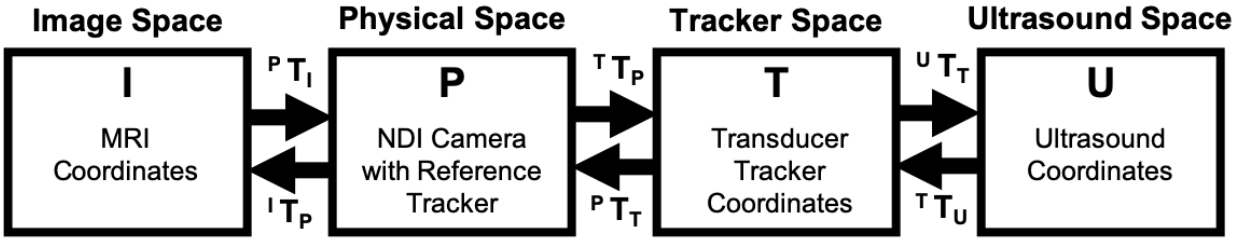

Figure 5.1: The four coordinate systems of interest in optically tracked FUS. The transducer steering coordinate system can be related to the imaging coordinate system through a series of transformations which allow for accurate targeting of specific brain structures with FUS.

MR image coordinates, the tracking camera coordinates, the transducer tracker coordinates, and the transducer coordinate system (figure 5.1). The MR coordinate system is defined by the scanner and is included in the image headers which are read into 3D Slicer. The tracking camera coordinates are streamed from the camera which is tracking a reference tracker. The reference tracker is fixed on the platform used for both phantom and NHP scans. Both the phantom and NHP are in fixed positions relative to the reference tracker (figure 5.2). This reference tracker allows for the camera position to move if needed and maintains a fixed coordinate system between repeated scans which may be acquired with different camera orientations. The coordinates of the transducer tracker, a tracking tool mounted onto the back of the transducer, is also streamed from the tracking camera and enables tracking the transducer relative to

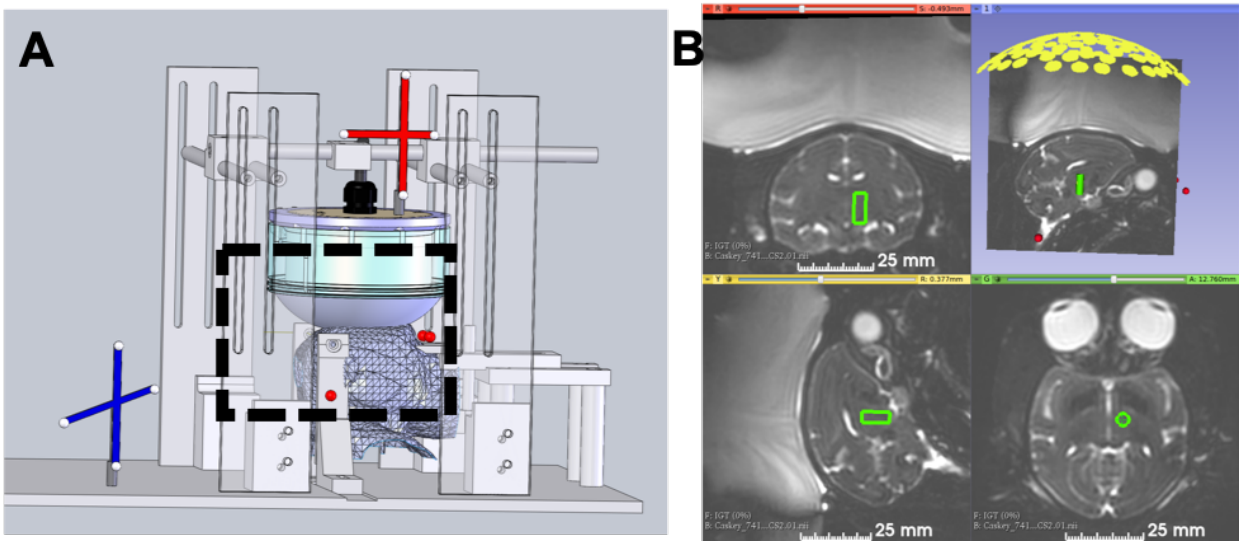

Figure 5.2: A: A model of the physical set up of the optically tracked NHP experiment. The NHP is placed on a custom table for MR imaging and the head fixed in place with a frame. The FUS transducer is placed over the head on a frame built into the table. The transducer has a optical tracker placed on the back and a water bubble on allows for ultrasound coupling. Fiducials are placed on the ear bars and eye bars of the frame (red spheres). A reference tracker is fixed to the table for optical tracking. MR coils are placed on either side of the head (not pictured). The black dashed region is the approximate MR imaging region. B: The 3D Slicer view of the NHP experiment. The optically tracked focus model is shown with the green cylinder. Fiducial markers (red spheres) can be localized and registered to the physical marker locations. The individual elements of the transducer can be visualized in the MR space.

reference tracker. Finally, the ultrasound coordinate system which has its origin at the geometric focus is given by a fixed offset and rotation from the transducer tracker coordinate system.

The notation from section 2.3.2 can be used where a location in a given space A is ${}^{A}x$ and a transform from coordinate system A to coordinate system B by ${}^{B}T_{A}$. The four coordinate systems described above can be denoted as the image space from the MRI (I), the physical space recorded by the camera (P), the tracker space (T), and the transducer coordinate system ultrasound space (U) as in figure 5.1 and the following equation 2.9 can be used to find a coordinate in image space from a coordinate in ultrasound space. Each of the transforms needed for this conversion is measured or calculated in a different manner.

${}^{P}T_{T}$ is measured from the Polaris Vicra system as a 4-element quaternion and converted to an augmented transformation matrix in the OpenIGTLink module of 3D Slicer and generated for the user. For this study a reference tracker which was fixed relative to the phantom or NHP was used to allow the camera to move during the experiment. Using this additional tracker established the physical coordinate system P relative to the location and orientation of the reference tracker as measured by the camera. ${}^{I}T_{P}$ is found by registering a set of fiducial markers visualized with MRI to the same markers located in physical space using a NDI tracked stylus. Doughnut shaped markers (MM3002, IZI Medical Products Owings Mills, MD) are used so that the optically tracked stylus can be positioned with the tracked tip of the stylus inside the doughnut. The SlicerIGT Fiducial Registration Wizard extension [149] is used to register these two sets of fiducial locations. ${}^{I}T_{P}$ must be calculated for each experiment.

5.2.2—Tracker to FUS Transform

The last transform needed for optical tracking, ${}^{T}T_{U}$, connects the transducer tracker and transducer ultrasound coordinate systems for electronic steering. This transform is needed to link the estimated pressure distribution and steering coordinates through the camera space and into MR space. An optically tracked hydrophone experiment was used to measure the location of maximum pressure relative to the transducer tracker at 27 steered locations in the ultrasound space. This procedure was similar to previously reported methods [115]. A tracker was placed on a hydrophone holder which could be attached to a three-axis stage. Because needle hydrophone tips are susceptible to damage a mock hydrophone was used to perform a pivot test within the NDI Track software to measure the hydrophone tip location in physical space. The transducer was placed in a water tank with the transducer tracker fixed in place and programmed to sonicate a 3x3x3 grid of points separated by 5 mm each. The three-axis stage was used to move the hydrophone to find the maximum pressure for each steered location and the location of the hydrophone tip and the transducer tracker were recorded. The set of steered locations in ultrasound space were registered with the hydrophone tip locations relative to the tracker providing the needed transformation [150].

5.2.3—Bias Correction

Image-based bias correction was used to reduce errors inherent in methods used to generate the initial calculation of ${}^{T}T_{U}$, resulting in a final bias-corrected transform of ${}^{T}T_{U}{}^{*}$. In practice, the rigidity and tracking uncertainty contribute to an error that can be improved through image-based bias correction [114], [115]. The initial transform ${}^{T}T_{U}$ was implemented in

a phantom and *in vivo* MR-ARFI scans. Across six phantom and three *in vivo* scans the error between the optically tracked prediction and the center of the MR thermometry or MR-ARFI location was measured. The mean error in these measurements was assumed to be a bias in the transformation and was subtracted from the translation of the transformation. The rotation of the transform was not altered.

5.2.4—Target Registration Error

Using equation 2.9, we project a model of the free field focus from the ultrasound space into the MR space to estimate the focus location relative to brain anatomy. MR thermometry or MR-ARFI visualize the focus location in the phantom or NHP to validate this estimate. The translational error between the visualized focus, ${}^{I}x_{focus}$, and tracker predicted focus, ${}^{I}x_{optical}$, can be quantified by placing a marker at the coordinate of the visualized focus, ${}^{I}x_{focus}$, in image space. Using eq. 1, this coordinate can be transformed into ultrasound space giving ${}^{U}x_{focus}$. $||{}^{U}x_{focus}||$ corresponds to the translational error between tracked and actual focus locations. Electronically steering the transducer focus to $-{}^{U}x_{focus}$ will steer the beam to the ${}^{U}x_{optical}$, the optical tracking predicted focus.

5.2.5—Steering to Arbitrary Targets

Once the error vector is known it can be used also steer to any point within the steering range of the transducer. A marker is placed at a desired target in MR space and transformed into the ultrasound coordinate space. The transformation gives the steering vector needed to move the focus from the initial estimate to the new target. By then adding the offset found

from the error vector to this point the tracking error is corrected and the ultrasound coordinate will coincide with desired target. Restated using coordinate notation, there is a target in image space ${}^{I}x_{target}$ where the FUS should be applied, the focus location of the first sonication ${}^{I}x_{focus}$ as determined by MR-ARFI, and the estimated focus location from optical tracking ${}^{I}x_{optical}$. The steering values, S for any ${}^{I}x_{target}$ is:

$$S = {}^{U}x_{target} - ({}^{U}x_{focus} - {}^{U}x_{optical}) \quad \text{Eq. 5.1}$$

5.2.6—FUS Pulses and Calibration

Sonications were performed with a 128 element randomized phased array with a radius of curvature (ROC) of 72 mm and diameter of 103 mm operated at 650 kHz [1]. The transducer output was characterized with hydrophone measurements at the geometric focus and steering locations out to 7 mm distance in 1mm steps with a ceramic needle hydrophone (HNC 0400, Onda Corp., Sunnyvale CA). Calibration curves were generated from low pressure sonications and a line of best fit was used to estimate free field pressure for each lateral steering distance. A separate calibration curve at the geometric focus was taken with a fiber optic hydrophone (FOH, Precision Acoustics, Dorchester, UK) at pressures up to 4.0 MPa and showed a good linear fit for the peak negative pressure (R^2=0.9987). MR thermometry in phantoms was acquired with continuous wave sonications until the focus was detected. Phantom MR-ARFI was performed with 10 ms sonications at 5.0 MPa free field pressure adjusted based on steering distance. *In vivo* MR ARFI was performed with up to 8.5 ms pulses at 5.5 MPa free field pressure. The pressure in the brain is expected to be significantly attenuated due to the skull. A transmission percentage of 39% was estimated based on previous tests though an *ex vivo* skull

[91] resulting in an estimated pressure of 2.1 MPa. This corresponds to an *in vivo* mechanical index (MI) of 2.6.

5.2.7—MR FUS Sequences

MR imaging was performed on one of two magnets: a clinical 7T system (Philips Achevia, Philips Healthcare, Best, Netherlands) and a clinical 3T system (Philips Achevia, Philips Healthcare, Best, Netherlands). On the 7T system a custom built surface coil was used which could be placed in between the transducer and phantom/NHP. For the 3T system a pair of surface coils (dStream Flex S, Philips Healthcare, Best, NL) were placed on either side of the phantom/NHP with the transducer positioned above. MR thermometry scans in phantoms were acquired with a multishot echo planar imaging gradient echo with a TE of 10 ms, a TR of 25 ms, 2 mm x 2 mm in-plane resolution with 5 slices of 3 mm slice thickness and a 1 mm slice gap. The real and imaginary data were collected and used to create the complex data where phase subtraction by complex multiplication was used to estimate phase difference from the initial dynamics [105]. MR-AFRI was performed using a 2D spin-echo EPI sequence (7T) or a 3D spin echo sequence (3T). The Motion encoding gradients (MEG) were trapezoidal, had durations between 3 ms (7T) and 8 ms (3T), had amplitudes of 40 mT/m, and were triggered 2 ms after the sonication start time. For 7T ARFI scans a 4 mm thick slice with 2 mm x 2 mm in plane voxel size with a TE/TR of 16 ms/500 ms was used. At 3T scans were 2 mm x 2 mm x 4 mm voxel size with 3 slices and a TE/TR of 34 ms/500 ms. A set of two ARFI scans were performed with the first scan using positive MEG polarity and the second scan using negative MEG polarity. FUS was applied on one dynamic of each scan and was turned off for a second dynamic so that four

images consisted of FUS off + MEG, FUS on + MEG, FUS off - MEG, FUS on - MEG. The resulted images images were used to compute displacement maps as described in [91].

5.2.8—Phantom Studies

Phantoms were prepared with 1% w/v agar power and 4% w/v silica carbide mixed into water and heated to boiling. The phantom mixture was then cooled while stirring to ensure consistency and pouring into a phantom holder. Once the phantom was set it was fixed to a stereotaxic table which allows for transducer positioning and is also used for the NHP studies. Fiducial markers were placed around the outside of the tube. The MR coil was put in place and the transducer positioned above the phantom with a water coupling bag and ultrasound gel and its position optically tracked. The positions of the fiducials were measured in physical space with a stylus tool and a T1 weighted scan was used to localize the fiducials in image space. These two sets of coordinates were registered to generate the physical to image transform, ${}^{I}T_{P}$. MR thermometry could then be performed at the geometric focus and steered locations. The optical tracking error was measured from the center of the predicted focus to the center of the thermometry hot spot. An arbitrary point was selected in the phantom and the steering coordinates for the transducer determined. This point was then sonicated to assess the accuracy of steering.

5.2.9—NHP Studies

All work on NHPs was performed with approval of the Vanderbilt IACUC. Sedation and anesthesia was performed the same as section 3.2.4 and the NHP was placed in a stereotactic

frame with ear bars, eye bars, and a mouthpiece (figure 5.2 A). Two fiducials were located on each of the ear bars and a fiducial was placed on each eye bar. The transducer with a degassed water filled coupling bag was placed on top of the shaved head with ultrasound coupling gel applied and the MR coils positioned by the head. The transducer was aimed at the center of the brain and the fiducial locations and transducer tracker location were collected in physical space. A T1 weighted image was acquired to localize the fiducials in image space and a T2* weighted image was used to target selection. MR-ARFI was performed and all MR images were loaded into 3D Slicer. The fiducials were used to register the physical space to image space as described above. A location within the thalamus and insular cortex were identified and image coordinates selected. The center of the displacement map from MR-ARFI and the optically tracked focus estimate were selected and the ultrasound steering coordinates for the thalamus and insula targets were calculated. The transducer was then steered each target and a MR-ARFI sequence was acquired.

5.3—Results

5.3.1—Transducer Calibration

The transducer was steered from the geometric focus to a lateral steering of 7mm in 1mm increments and the pressure recorded for a series of input driving amplitudes. As expected higher driving amplitudes are needed where steering away from the geometric focus. At each point tested the system was capable of generating sufficient pressure for transcranial displacement detection via MR-ARFI and this pressure could be matched to the geometric focus.

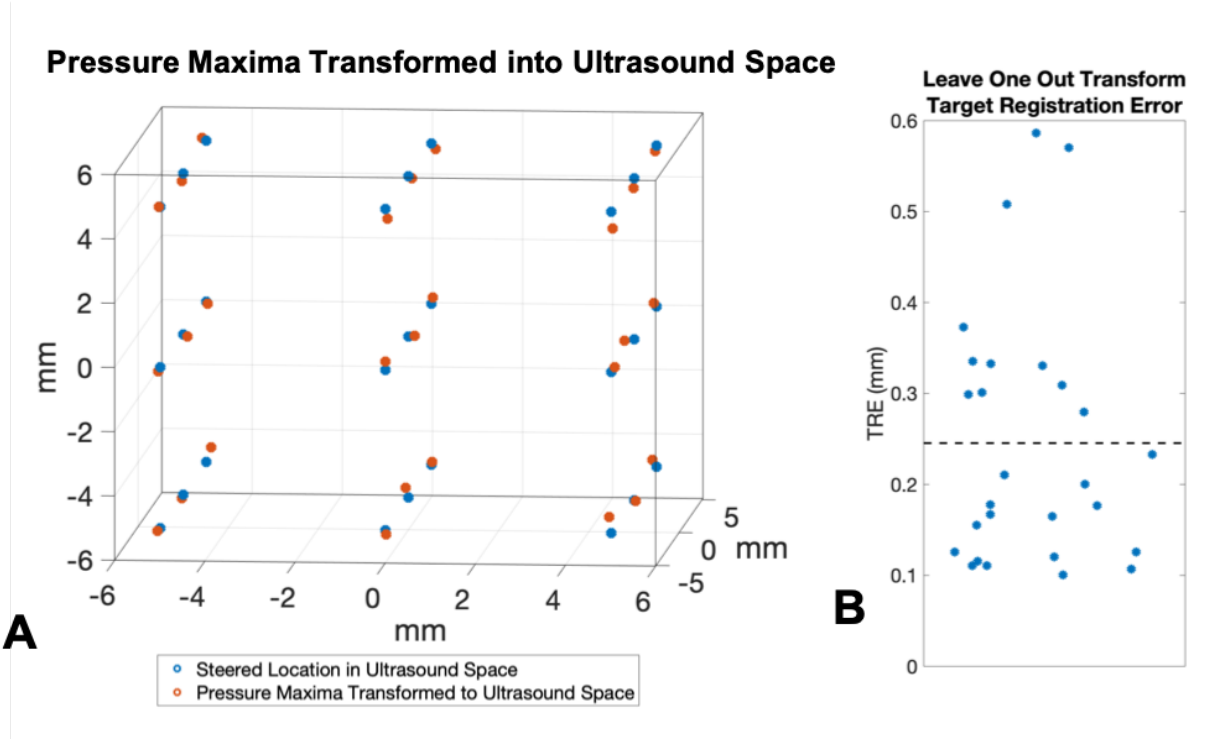

Figure 5.3: A collections of 27 optically tracked pressure maxima was found for 27 steered locations of the FUS beam along all three axes and a transformation generated between these data points. A: The optically tracked hydrophone focus locations transformed into ultrasound coordinates and plotted on top of the known steered locations in the ultrasound coordinate system. Points were sonicated in a 3 x 3 x 3 grid with 5 mm step sizes. There is good agreement between the sonicated locations and the optically tracked pressure maxima. B: To test the targeting error of the optically tracked hydrophone the transformation between the pressure maxima and the steered locations was generated using 26 of the 27 locations and the 27th point was used to measure the error. This measurement was made for each point. All errors were under 0.6 mm with a mean error shown with the black dashed line of 0.25 mm.

5.3.2—Transducer Coordinate Space Transformations

The hydrophone based transformation was generated by registering 27 known sonication locations in ultrasound space to the measured focus location of an optically tracked hydrophone. The fiducial registration error between these two datasets was 0.26 mm (figure 5.3 A). To test the accuracy of the transform the registration was performed in a leave one out

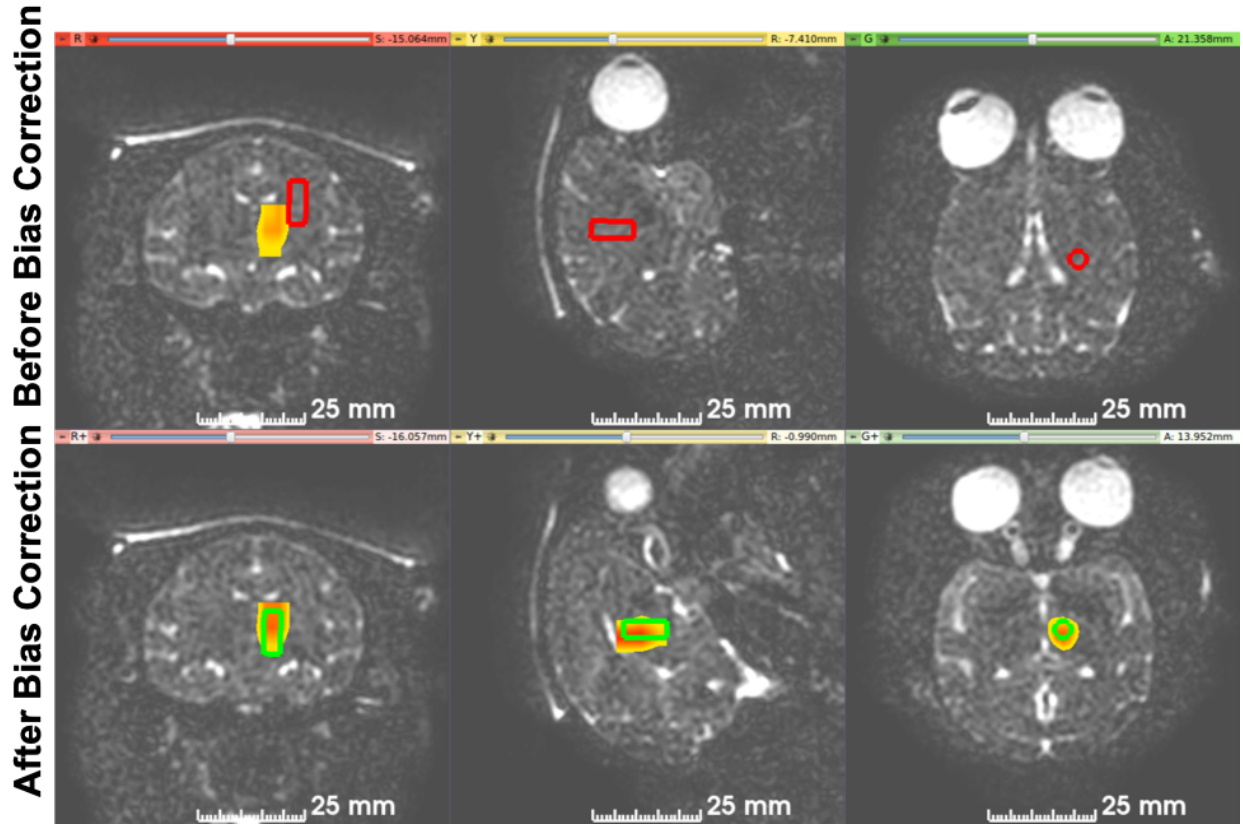

Figure 5.4: Top: The predicted focus location (red cylinder) compared to a thresholded MR-ARFI displacement map in the brain (color map in the middle of the brain) before bias correction was applied. Bottom: After bias correction was applied the predicated focus location (green cylinder) is now in agreement with the measured focus location.

fashion with 26 points being used to generate the transformation and the final point be used to test the target registration error (TRE). The mean TRE across these 27 points was 0.25 mm with a maximum error of 0.59 mm (figure 5.3 B).

After using this transform in both phantom and *in vivo* scans a lateral bias of 6.6mm and an axial bias of 7.0 mm was observed (figure 5.4). The translation portion of the transformation was modified to account for this bias and in three *in vivo* MR-ARFI tests the TRE after bias correction was found to be 1.0 mm, 3.6 mm, and 1.6 mm for an average TRE of 2.1 mm.

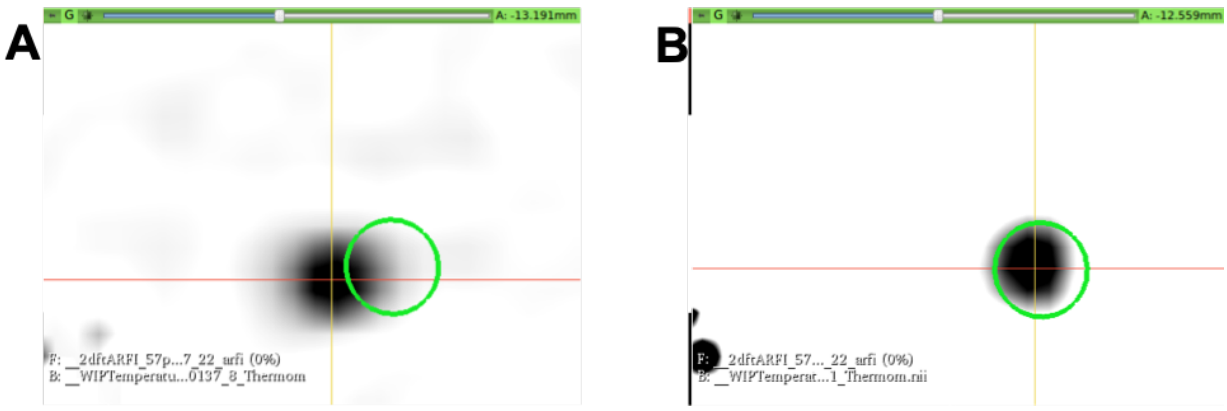

Figure 5.5: An example of the lateral bias in the initial tracker to ultrasound transformation. A: The optically predicted focus is shown with the green circle and MR thermometry shows a focus location that is laterally shifted from this focus. B: Even without bias correction we are able to use the thermometry derived location of the focus to steer the beam to the optically predicted location.

Even without this bias correction the optically tracking data can be combined with the focus location as measured by MRI to correct and steer the beam. By subtracting the error as described in the methods we are able to correct for error and target the FUS beam to the optically predicted focus location (figure 5.5).

5.3.3—*In Vivo* Multi-Target Steering

In an NHP experiment we selected two targets of interest: the thalamus and insula on the same side of the brain. The initial positioning of the transducer positioned the focus in between these two targets. The focus location was measured *in vivo* with MR-ARFI and the steering coordinates needed to correct for tracking error and target the thalamus and insula determined. Both targets were successfully sonicated with the selected point for each target being located within the displacement region on MR-ARFI images (figure 5.6).

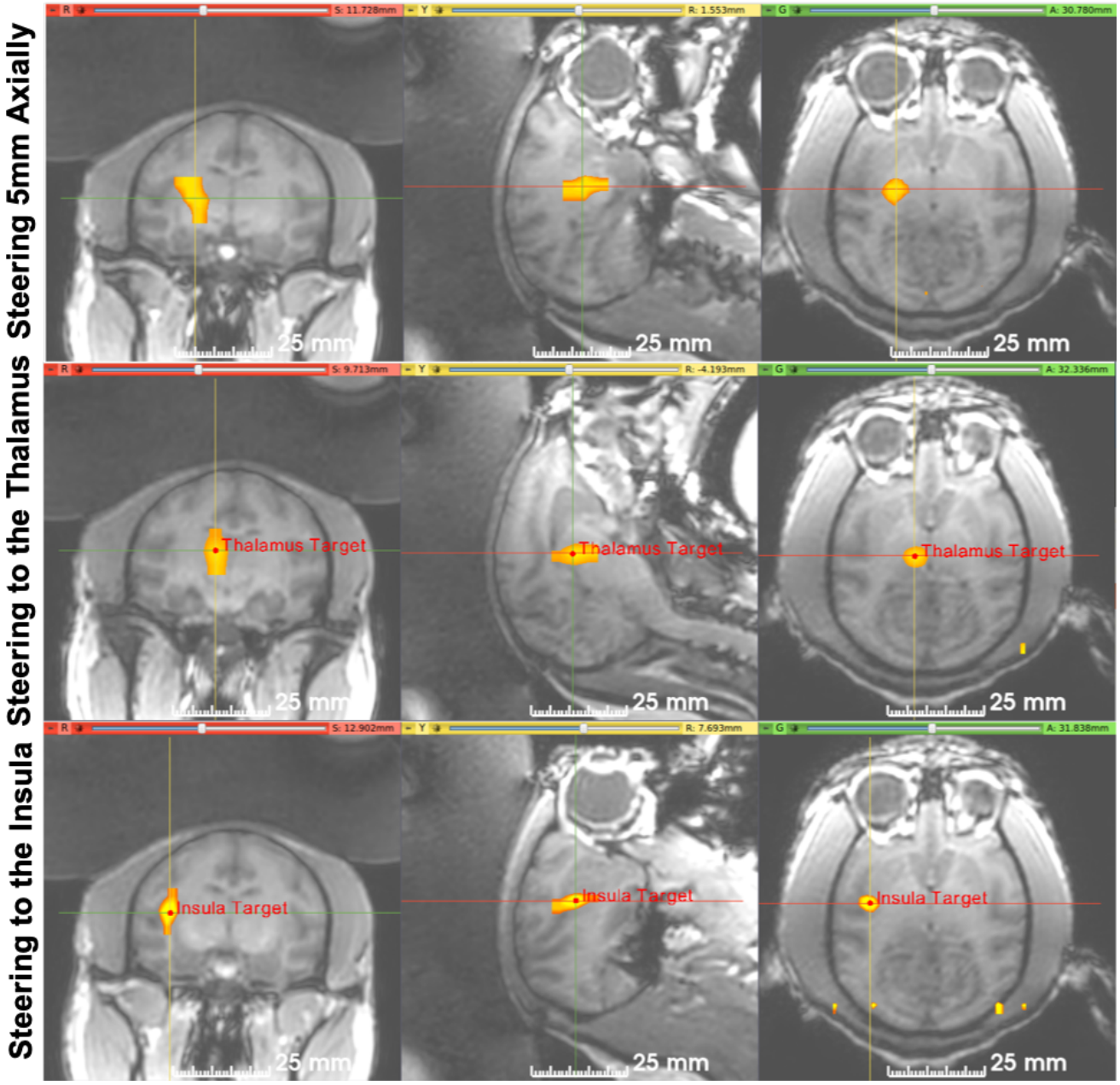

Figure 5.6: Steering to brain regions of interest. Top: The MR-ARFI focus location when steering 5mm towards the transducer. Middle: Using the optical tracking transformations and a know target in the thalamus we were able to steer the beam so that the target point was within the ARFI location of the beam with a single test sonication. Bottom: This same test sonication allowed for steering to the insula target such that the target point in MR space was within the ARFI location.

5.4—Discussion

Transcranial FUS is being used for a wide range of applications in which accurate and precise targeting is critical. The ideal targeting system would be noninvasive, allow for beam correction, and measure the effects of the beam on tissue. Combining optical tracking with MR-ARFI provides a method to place the transducer near a desired target, localize the beam, and then steer the beam to correct for any tracking error and to sonicate further targets. In this work, we demonstrated a method that allows for rapid and accurate target selection during FUS procedures with a minimum amount of FUS energy deposited in the tissue.

Deep brain targets are of interest for FUS neuromodulation since FUSis able to target these structures noninvasively with high spatial resolution [151]. The ability to target structures such as the thalamus and correct the targeting error is important for research or clinical applications. In this study, the optical tracking information about the transducers position within the image space was used to align the transducer near a target of interest in the NHP brain. A MR-ARFI localization scan then determined where the FUS beam was located *in vivo* and a tracking error was determined. This error was then used to correct the steering of the transducer to hit the initial target in addition to a secondary target as measured by MR-ARFI.

Optical tracking is frequently used for image guidance in transcranial FUS applications and studies designed to assess accuracy report errors in the 2-3 mm range. Previous work has used optical tracking with single element transducer to target specific brain structures. Kim et al performed optically tracked FUS application using a physical offset to mimic the transducer focus. This offset was then measured using tested using MRI and a bias was corrected providing an error of 1.9 mm [114]. Wu et al. performed optical tracking of a blood brain barrier opening with FUS. For this study optical tracking was used to position a transducer so that the beam

path and focus location matched preplanned path [57]. Chaplin et al. used an optically tracked beam map to project the free field focus into MR anatomical images. The transducer could then be moved so that the beam map overlapped with the desired target. This method was shown to have an error in phantoms of 2.4 mm [115]. In these studies a single element transducer was used which could not be steered, corrections between the estimated focus locations and a measured focus location could not be applied electronically.

Here, the ability to target multiple areas of interest within the brain based on optical tracking information and a single localization scan is shown. Two brain regions were selected, the insula and thalamus, and each the beam was steered to these targets and the MR-ARFI signal overlapped with the selected target points. Recent studies with FUS neuromodulation have targeted multiple regions of the brain to better understand networks and to act as controls so that the effects of stimulations can be better understood [78], [152]. Accurate electronic steering of an array transducer allows for multiple regions to be targeted without having to adjust the transducers position. With electronic steering, the focus of the transducer can be rapidly moved between targets in millisecond time scales which is much faster than the hemodynamic response measured by fMRI [153]. The FUS system used in this study is also capable of sonicating multiple targets at once [154]. The ability to target separated brain regions with a single experimental setup will allow for new hypothesis to be tested.

Safety of FUS pulses in the brain is currently being studied, and there does not yet exist a well-defined standard for ultrasound pulses used in ARFI. FDA guidelines on safety requirements for ultrasound imaging devices were developed based on assessments of ultrasound devices deployed in 1976 and for short duration pulses that are many times shorter

than those used for ARFI [12], [46]. While diagnostic imaging metrics and limitations were not designed for transcranial ARFI pulses, they still provide a useful means to quantify the pulse. To generate a detectable displacement of approximately 2 µm, we required a pulse with an estimated pressure at the transcranial focus of 2.1 MPa. This corresponds to an MI of 2.4 which exceeds the diagnostic imaging guideline of 1.9 and was below highest guidelines for I_{sppa} (153.4 W/cm^2) and I_{spta} (690 mW/cm^2). Because much of the transmitted sound is scattered and absorbed in the skull, the peak negative pressure experienced by neural tissue is much lower than if the skull were not present. Thermal safety is also of concern with repeated FUS pulses. Studies have shown through simulation and MR thermometry that heating can be minimized to under 0.5°C in the brain while still localizing the beam [91], [92]. MR-ARFI is capable of sensing displacements as low as 100 nanometers in phantoms [25], [106], but the sensitivity in an *in vivo* imaging situation is often lower due to the inhomogeneous media, motion, and other factors. Previous studies of neuromodulation and ARFI FUS pulses have not found any histological evidence of damage at higher MI than used in this study [126] but further study is needed to ensure damage or secondary effects are not occurring.

Optically tracking the transducer coordinates can be used to allow for aberration correction through the skull. Since the skull is known to attenuate the FUS beam and distort the shape and location of the focus methods have been developed to correct for these effects [33]. The repeated collection of MR-ARFI displacement information can be used correct for these aberrations [155]. Other methods use simulations through the skull to estimate the aberration and correct the focus [99]. By combining CT or MR bone imaging methods with the optically

tracked and registered data, aberration correction can be added to the procedure allowing for a smaller focus with more gain at the desired targets.

5.6—Conclusion

In this work we detail a method to target and sonicate brain regions of interest with transcranial FUS. By improving the targeting of FUS we can perform better basic research into FUS neuromodulation with better confidence of what brain regions are being sonicated. This improved targeting can also help with clinical applications of FUS since all applications require accurate targeting.

Chapter 6—Applications and Future Directions

Transcranial focused ultrasound has potential to provide clinical and research tools for a number of areas. Direct effects of the FUS beam are being studied for neuromodulation. FUS and microbubbles are being used to open the BBB. Heating can be used for therapeutic purposes, either high heat to kill tissue or mild heating for immune response. All of these applications require accurate targeting. For clinical uses, poor targeting can result in unexpected damage or no treatment of the condition. For a research study, poor targeting can confound the results since the data will not represent what the experimenters thought was occurring. Safe and accurate targeting is an important aspect of transcranial focused ultrasound.

6.1—Summary of Key Findings

Chapter 3 presented simulations of measurements of the heating that can occur when using MR-ARFI to localize the focus of the transducer. Pressure measurements and simulations were made while transmitting the beam through a representative NHP skull fragment to estimate the pressure loss due to the skull. These pressure simulations were used to generate thermal simulations. It was shown that MR-ARFI type sonications could induced mild heating within the skull of around 2 degrees but that minimal heating would occur at the focus. MR thermometry was performed *in vivo* to measure the heating when sonicated with a MR-ARFI style FUS pulse which found minimal heating *in vivo*. Finally these safety tests enabled the

testing of *in vivo* MR-ARFI in NHPs for beam localization. This fully developed MR-ARFI sequence with safe FUS pulses allowed localization of direct effects of the beam within the NHP brain. While no histology was able to be performed since the NHPs are still involved in ongoing neuroscience experiments no signs of damage have been detected in scalp and no gross behavioral changes have been observed. This tool was used in these ongoing neuroscience studies and continues to be used to localize the beam for fMRI studies.

Chapter 4 presented a method to reduce the amount of FUS energy needed to localize the beam by reducing the effective aperture of the transducer. A 128-element array was programmed so that the outer elements could be selectively turned off, reducing the effective aperture of the array. Hydrophone measurements were taken for three different configurations of this array and an increase in the harmonic content was observed with the smaller aperture configurations. Simulations of each of these configurations also found an increase in the harmonic content as well as an increase in the focal size in axial and lateral directions of the beam. These pressure simulations were used to simulate the displacement in a homogeneous medium which found that the smaller aperture size lead to a larger focal displacement and larger displaced volume. Phantom studies using the same three configurations confirmed this increased displacement with a near doubling in measured displacement at the same peak negative pressure from the largest to smallest aperture. *In vivo* studies found similar displacement while using 20 percent less PNP for the smallest aperture compared to the full array. This work shows a method to reduce the needed energy localize the beam with MR-ARFI allowing for safer experiments with a lower likelihood of off target effects from the localization sonications. The effect was less pronounced *in vivo* compared to phantom studies and

homogeneous simulations which could be due to filtering of the harmonics due to the skull. This method of reducing the amount of energy used can be combined with other methods to localize the beam with as little energy as possible.

Chapter 5 presented a method to correct optical tracking error and accurately target multiple brain regions. Optical tracking for a 128-element array transducer was developed using an optically tracked hydrophone to measure the focus location relative the tracker. The error in this optically tracked focus was corrected with a number of phantom and *in vivo* MR thermometry and ARFI scans. A MR-ARFI localization scan was then used with this optically predicted focus to correct any error. In addition to error correction this method could be used to steer to other brain regions which are identified on MRI so that further regions could be sonicated. This method allows for multiple targets in the brain to be accurately targeted within one session and with a single localization scan. Targeting multiple regions allows for new options for both clinical and research studies by targeting multiple parts of brain network and providing control regions.

6.2—Recent and Ongoing Applications

The work presented here has been used as part of ongoing neuromodulation studies in NHPs. FUS was applied to the somatosensory areas 3a/3b to study the neuromodulation induced by the FUS [10], [65]. The goal of this study was to better understand the effects of FUS neuromodulation in large animal model. This model allowed for a straight forward study design since the somatosensory regions of NHPs are well studied [156], [157]. A tactile stimulation of the hand was used as a control for the somatosensory region and FUS was targeted to area

3a/3b. Initial studies were performed without any image based targeting using external features of the head. An optical tracking system was developed to better target the beam [115].

Optical tracking of the beam location provided the ability to quickly target the correct region but was not able to determine if the FUS was reaching the region. If the transducer was poorly coupled to the head then most of the FUS would reflect off any air in the coupling leading to significantly less energy at the focus than predicated. Since angle of incidence on the skull also affects transmission of sound [158] the optically tracked focus may be accurately targeted to the region but the sound could be reflected off of the skull. By adding MR-ARFI after targeting the transducer it is possible to confirm that focus is in the targeted region and that energy is being transmitted well. The optical tracking information was used to better align the MEGs needed for MR-ARFI with the beam direction to maximize the detected signal [91]. Further work is needed to understand how the ARFI displacement maps correspond to neuromodulation bioeffects on tissue.

Since optical tracking and MR-ARFI provide a much better estimate of the beam location more confidence can be placed in the results of the experiments. To study the possibility of using FUS for neuromodulation a block based fMRI study was performed where blocks of either FUS or tactile stimulation were interleaved with rest periods. This study design allowed the fMRI signal of various brain regions to be measured in response to direct stimulation of the NHP hand or FUS stimulation of the 3a/3b region of the brain. This study found activation in the FUS targeted region and in spatially distinct regions of the brain which are functionally connected to the 3a/3b region. Only small signal changes in nearby white matter regions suggests that this response is neural and not due to some other effect. For both the tactile stimulation and FUS

stimulation the hemodynamic response for each region was similar suggesting a neural response. A difference in the magnitude and latency of signal was seen between tactile and FUS which can be interpreted as the neural response having different pathways for each stimulation. For the tactile stimulation, the signal is generated in the hand and then travels to the brain and though the circuits while FUS is able to directly stimulate the 3a/3b region in the middle of the circuit [10].

A follow up study was conducted with lower amplitude FUS stimulation, approximately half the pressure as in the previous study [65]. A model of FUS neuromodulation looking at published data suggested that lower intensity FUS could lead to inhibition of neurons while higher pressure would lead to activation [159]. Since activation was observed in the previous study using a lower amplitude pulse allowed the mechanisms of FUS neuromodulation to be studied. This study used blocks of FUS, tactile, and FUS+tactile stimulation with the FUS targeted to area 3a/3b. When only FUS was applied, similar activations were seen compared to the higher pressure pulses. However, when FUS was applied at the same time as tactile stimulation the fMRI signal was reduced in the target area and downstream pathways compared to tactile stimulations alone. By accurately targeting and confirming the beam location with ARFI, brain circuits can be interrogated with FUS to better understand brain function and connectivity.

Current NHP neuromodulation studies are being performed on different brain targets to study pain circuits. These targets are deeper in the brain and a more robust study design to target multiple regions within the same session is desired. Using the work demonstrated in chapter 5, a single localization scan with MR-ARFI can allow for any target within 10mm

laterally and 20mm axially of the initial focus placement [1]. Recent neuromodulation studies have shown changes in activity of interconnected regions following FUS neuromodulation pulses [9], [78]. The ability to steer the focus of the transducer to multiple targets in a single study will improve the ability to test circuits rather than single regions. A steerable focus can also be used to target unconnected regions of the brain to better control for potential off target effects of the FUS stimulation, such as auditory stimulation [160], [161], which can confound the results of neuromodulation studies.

6.3—Future Applications and Directions

The blood brain barrier can be opened using FUS and microbubbles. Opening the BBB provides clinical treatment options and new research opportunities. Whether delivering cancer therapeutics [162] or opening the BBB to study brain circuits [63] targeting the correct region is important and verifying sound delivery increases the confidence in the treatment. MR-ARFI can be used before the microbubble injection to ensure the focus is in the brain region of interest and to predict spatial distribution of the BBB opening by visualizing the size and shape of the beam. Since BBB disruption relies on microbubbles to open the tight junctions in the brain [163] too much energy can result in cavitation and damage to the tissue [164]. Displacement induced by the acoustic radiation force scales with the acoustic power and frequency [25], [91], [106]. The displacement can potentially be used to estimate pressure at the focus so the BBB disruption pulses can be programmed at the optimal pressure to not cause damage while opening the BBB.

The methods presented in this dissertation can be extended to provide easier to use tools and better understanding of possible damage or off target effects. Optical tracking provides a very good method to place the focus of the transducer on a target of choice in the brain but has some strong drawbacks. The optical tracking equipment is expensive and may not be available for many people who wish to perform transcranial FUS. Optical tracking often requires multiple trips into and out of the magnet room to perform the initial scan for fiducial localization, then perform optical tracking and possible retarget if the targeting does not work due to coupling or other reasons; these trips add time and risk the experiment. A similar resteering method can be developed by using MR visible fiducials fixed relative the transducer and generated a transformation to convert points in MR space to ultrasound space. These fiducials would eliminate the need to optical tracking while still providing a method to steer to multiple regions within the brain with a single localization scan. This method of steering would require good initial placement of the transducer so the focus is within steering range of the desired targets which may be difficult to achieve though an external frame could be using known anatomy of the head to place the transducer within a steerable range of the target.

Further safety studies are needed to advance MR-ARFI for human studies. The work presented in this dissertation shows a method to study the risk of thermal damage when performing MR-ARFI. Pressure and thermal simulations can provide insight into how much heating will occur in the brain at the focus and in skull along the beam path and MR thermometry can measure *in vivo* heating in the brain tissue. The risk of thermal damage to the bone marrow is concern during transcranial FUS procedures [118], [119]. Only a limited amount of histology has been shown following exposure to MR-ARFI sonications. This histology showed

no signs of damage to the brain tissue on the sonicated side compared to controls [126]. However, many of the reported ARFI pulses exceed the FDA limits for MI during ultrasound imaging. It is not clear that these pulses are safe for long term use and further study of the safety is warranted. Ongoing studies which the work in this dissertation contributed to with NHPs provides a source for histology studies. MR-ARFI and neuromodulation pulses have been applied at known locations within the brain over multiple years of studies providing known sonication locations such as area 3a/3b and control regions where sonications have not occurred.

The work contained here uses MRI to localize the target region and the FUS beam but for many uses being able to sonicate outside of a MR suite would provide strong advantages. Using a frame to place the transducer in the same location on the subjects head repeatable would allow of accurate sonications outside of the magnet. This frame can then be combined with optical tracking or a MR-ARFI session to determine steering coordinates to different brain targets. For clinical uses, treatments outside of a magnet could reduce the cost of treatment. Performing experiments outside of the magnet allows for a wider range of neuroscience tools to be used such as behavior assays. Neuromodulation studies have been performed using eye tracking to measure the effect of FUS neuromodulation on eye motion [75], [77]. By increasing the accuracy of the FUS transducer and opening the ability to steer to multiple targets in a single session these experiments can become more complex to probe more difficult questions in neuroscience.

Bibliography

[1] V. Chaplin, M. A. Phipps, and C. F. Caskey, “A random phased-array for MR-guided transcranial ultrasound neuromodulation in non-human primates,” *Phys. Med. Biol.*, Apr. 2018.

[2] A. D. Maxwell, C. A. Cain, A. P. Duryea, L. Yuan, H. S. Gurm, and Z. Xu, “Noninvasive Thrombolysis Using Pulsed Ultrasound Cavitation Therapy - Histotripsy,” *Ultrasound Med. Biol.*, vol. 35, no. 12, pp. 1982–1994, Dec. 2009.

[3] W. J. Elias *et al.*, “A Pilot Study of Focused Ultrasound Thalamotomy for Essential Tremor,” *N. Engl. J. Med.*, vol. 369, no. 7, pp. 640–648, 2013.

[4] V. Krishna, F. Sammartino, and A. Rezai, “A Review of the Current Therapies, Challenges, and Future Directions of Transcranial Focused Ultrasound Technology,” *{JAMA} Neurol.*, vol. 75, no. 2, p. 246, Feb. 2018.

[5] N. Todd *et al.*, “Focused ultrasound induced opening of the blood-brain barrier disrupts inter-hemispheric resting state functional connectivity in the rat brain,” *Neuroimage*, vol. 178, 2018.

[6] A. N. Pouliopoulos, S. Y. Wu, M. T. Burgess, M. E. Karakatsani, H. A. S. Kamimura, and E. E. Konofagou, “A Clinical System for Non-invasive Blood–Brain Barrier Opening Using a Neuronavigation-Guided Single-Element Focused Ultrasound Transducer,” *Ultrasound Med. Biol.*, vol. 46, no. 1, pp. 73–89, Jan. 2020.

[7] R. D. Airan *et al.*, “Noninvasive Targeted Transcranial Neuromodulation via Focused Ultrasound Gated Drug Release from Nanoemulsions,” *Nano Lett.*, vol. 17, no. 2, pp. 652–659, 2017.

[8] J. B. Wang, M. Aryal, Q. Zhong, D. B. Vyas, and R. D. Airan, “Noninvasive Ultrasonic Drug Uncaging Maps Whole-Brain Functional Networks,” *Neuron*, 2018.

[9] D. Folloni *et al.*, “Manipulation of Subcortical and Deep Cortical Activity in the Primate Brain Using Transcranial Focused Ultrasound Stimulation,” *Neuron*, vol. 101, pp. 1109-1116.e5, 2019.

[10] P.-F. Yang *et al.*, “Neuromodulation of sensory networks in monkey brain by focused ultrasound with MRI guidance and detection,” *Sci. Rep.*, vol. 8, no. 1, p. 7993, Dec. 2018.

[11] R. L. King, J. R. Brown, W. T. Newsome, and K. B. Pauly, “Effective parameters for ultrasound-induced in vivo neurostimulation,” *Ultrasound Med. Biol.*, vol. 39, no. 2, pp. 312–331, 2013.

[12] FDA, “Information for Manufacturers Seeking Marketing Clearance of Diagnostic Ultrasound Systems and Transducers.” .

[13] B. W. Cunitz, B. Dunmire, and M. R. Bailey, “Characterizing the Acoustic Output of an Ultrasonic Propulsion Device for Urinary Stones,” *IEEE Trans. Ultrason. Ferroelectr. Freq. Control*, vol. 64, no. 12, pp. 1818–1827, Dec. 2017.

[14] F. J. Fry and J. E. Barger, “Acoustical properties of the human skull,” *J. Acoust. Soc. Am.*, vol. 63, no. 5, pp. 1576–1590, May 1978.

[15] F. A. Duck, *Physical Properties of Tissue. A Comprehensive Reference Book, edited by Francis A. Duck*, vol. 18, no. 4. IPEM, 1990.

[16] J. Arendt Jensen, “A model for the propagation and scattering of ultrasound in tissue,” *J. Acoust. Soc. Am.*, vol. 89, no. 1, pp. 182–190, Jan. 1991.
[17] P. N. T. Wells, “Absorption and dispersion of ultrasound in biological tissue,” *Ultrasound in Medicine and Biology*, vol. 1, no. 4. Elsevier, pp. 369–376, 01-Mar-1975.
[18] M. D’Souza *et al.*, “Impact of skull density ratio on efficacy and safety of magnetic resonance–guided focused ultrasound treatment of essential tremor,” *J. Neurosurg.*, pp. 1–6, Apr. 2019.
[19] W. S. Chang *et al.*, “Factors associated with successful magnetic resonance–guided focused ultrasound treatment: efficiency of acoustic energy delivery through the skull,” *J. Neurosurg.*, vol. 124, no. 2, pp. 411–416, Feb. 2016.
[20] N. Y. Jung, I. Rachmilevitch, O. Sibiger, T. Amar, E. Zadicario, and J. W. Chang, “Factors related to successful energy transmission of focused ultrasound through a skull: A study in human cadavers and its comparison with clinical experiences,” *J. Korean Neurosurg. Soc.*, vol. 62, no. 6, pp. 712–722, Nov. 2019.
[21] P. J. J. White, K. Hynynen, G. T. T. Clement, and K. Hynynen, “Longitudinal and shear mode ultrasound propagation in human skull bone,” *AIP Conf. Proc.*, vol. 829, no. 7, pp. 251–255, Jul. 2006.
[22] G. Pinton, J.-F. Aubry, M. Fink, and M. Tanter, “Effects of nonlinear ultrasound propagation on high intensity brain therapy,” *Med. Phys.*, vol. 38, no. 3, pp. 1207–1216, 2011.
[23] A. P. Sarvazyan, O. V. Rudenko, and W. L. Nyborg, “Biomedical applications of radiation force of ultrasound: Historical roots and physical basis,” *Ultrasound in Medicine and Biology*, vol. 36, no. 9. Elsevier, pp. 1379–1394, 01-Sep-2010.
[24] K. Nightingale, “Acoustic Radiation Force Impulse (ARFI) Imaging: A Review,” *Curr. Med. Imaging Rev.*, vol. 7, no. 4, pp. 328–339, Nov. 2011.
[25] N. McDannold and S. E. Maier, “Magnetic resonance acoustic radiation force imaging,” *Med. Phys.*, vol. 35, no. 8, pp. 3748–3758, 2008.
[26] A. Payne, J. de Bever, A. Farrer, B. Coats, D. L. Parker, and D. A. Christensen, “A simulation technique for 3D MR-guided acoustic radiation force imaging,” *Med. Phys.*, vol. 42, no. 2, pp. 674–684, 2015.
[27] A. Manbachi and R. S. C. Cobbold, “Development and Application of Piezoelectric Materials for Ultrasound Generation and Detection,” *Ultrasound*, vol. 19, no. 4, pp. 187–196, Nov. 2011.
[28] M. R. Bailey, V. A. Khokhlova, O. A. Sapozhnikov, S. G. Kargl, and L. A. Crum, “Physical mechanisms of the therapeutic effect of ultrasound (a review),” *Acoustical Physics*, vol. 49, no. 4. Springer, pp. 369–388, Jul-2003.
[29] J. Y. Chapelon *et al.*, “New piezoelectric transducers for therapeutic ultrasound,” *Ultrasound Med. Biol.*, vol. 26, no. 1, pp. 153–159, Jan. 2000.
[30] J.-F. Aubry and M. Tanter, “MR-Guided Transcranial Focused Ultrasound,” in *Therapeutic Ultrasound*, J.-M. Escoffre and A. Bouakaz, Eds. Cham: Springer International Publishing, 2016, pp. 97–111.
[31] C. Constans, T. Deffieux, P. Pouget, M. Tanter, and J. F. Aubry, “A 200-1380-kHz Quadrifrequency Focused Ultrasound Transducer for Neurostimulation in Rodents and Primates: Transcranial in Vitro Calibration and Numerical Study of the Influence of Skull

Cavity," *IEEE Trans. Ultrason. Ferroelectr. Freq. Control*, vol. 64, no. 4, pp. 717–724, 2017.
[32] E. S. Ebbini and C. A. Cain, "Multiple-Focus Ultrasound Phased-Array Pattern Synthesis: Optimal Driving-Signal Distributions for Hyperthermia," *IEEE Trans. Ultrason. Ferroelectr. Freq. Control*, vol. 36, no. 5, pp. 540–548, 1989.
[33] A. Kyriakou, E. Neufeld, B. Werner, M. M. Paulides, G. Szekely, and N. Kuster, "A review of numerical and experimental compensation techniques for skull-induced phase aberrations in transcranial focused ultrasound," *Int. J. Hyperth.*, vol. 30, no. 1, pp. 36–46, Feb. 2014.
[34] F. Marquet *et al.*, "Non-invasive transcranial ultrasound therapy based on a 3D CT scan : protocol validation and in vitro results," *Phys. Med. Biol.*, vol. 54, pp. 2597–2613, 2009.
[35] G. T. Clement and K. Hynynen, "A non-invasive method for focusing ultrasound through the human skull," *Physics in Medicine and Biology*, vol. 47, no. 8. IOP Publishing, pp. 1219–1236, 21-Apr-2002.
[36] F. J. Fry, "Transkull transmission of an intense focused ultrasonic beam," *Ultrasound Med. Biol.*, vol. 3, no. 2–3, pp. 183–184, Jan. 1977.
[37] G. T. Clement, J. Sun, T. Giesecke, and K. Hynynen, "A hemisphere array for non-invasive ultrasound brain therapy and surgery," *Phys. Med. Biol.*, vol. 45, no. 12, pp. 3707–3719, Dec. 2000.
[38] K. Hynynen *et al.*, "500-Element ultrasound phased array system for noninvasive focal surgery of the brain: A preliminary rabbit study with ex vivo human skulls," *Magn. Reson. Med.*, vol. 52, no. 1, pp. 100–107, 2004.
[39] P. Ghanouni *et al.*, "Transcranial MR-Guided Focused Ultrasound: A Review of the Technology and Neuro Applications."
[40] K.-T. Chen *et al.*, "Neuronavigation-guided focused ultrasound for transcranial blood-brain barrier opening and immunostimulation in brain tumors," *Sci. Adv.*, vol. 7, no. 6, p. eabd0772, Feb. 2021.
[41] J. J. Bevelacqua, "Practical and Effective ALARA," *Health Phys.*, vol. 98, no. 2 SUPPL. 2, pp. S39–S47, May 2010.
[42] T. R. Nelson, J. B. Fowlkes, J. S. Abramowicz, and C. C. Church, "Ultrasound biosafety considerations for the practicing sonographer and sonologist.," *J. Ultrasound Med.*, vol. 28, no. 2, pp. 139–50, 2009.
[43] R. E. Apfel and C. K. Holland, "Gauging the likelihood of cavitation from short-pulse, low-duty cycle diagnostic ultrasound," *Ultrasound Med. Biol.*, vol. 17, no. 2, pp. 179–185, Jan. 1991.
[44] C. K. Holland and R. E. Apfel, "Thresholds for transient cavitation produced by pulsed ultrasound in a controlled nuclei environment," *Cit. J. Acoust. Soc. Am.*, vol. 88, p. 2059, 1990.
[45] C. C. Church, C. Labuda, and K. Nightingale, "A Theoretical Study of Inertial Cavitation from Acoustic Radiation Force Impulse Imaging and Implications for the Mechanical Index," *Ultrasound Med. Biol.*, vol. 41, no. 2, pp. 472–485, Feb. 2015.
[46] D. L. Miller, "Safety Assurance in Obstetrical Ultrasound," *Semin. Ultrasound, CT MRI*, vol. 29, no. 2, pp. 156–164, Apr. 2008.
[47] D. Schlesinger, S. Benedict, C. Diederich, W. Gedroyc, A. Klibanov, and J. Larner, "MR-guided focused ultrasound surgery, present and future," *Med. Phys.*, vol. 40, no. 8, p.

080901, 2013.
[48] S. A. Sapareto and W. C. Dewey, “Thermal dose determination in cancer therapy.,” *Int. J. Radiat. Oncol. Biol. Phys.*, vol. 10, no. 6, pp. 787–800, Jun. 1984.
[49] D. Bonekamp *et al.*, “Twelve-month prostate volume reduction after MRI-guided transurethral ultrasound ablation of the prostate,” *Eur. Radiol.*, vol. 29, no. 1, pp. 299–308, Jan. 2019.
[50] Y. S. Kim *et al.*, “Volumetric MR-HIFU ablation of uterine fibroids: Role of treatment cell size in the improvement of energy efficiency,” *Eur. J. Radiol.*, vol. 81, no. 11, pp. 3652–3659, 2012.
[51] P. S. Fishman *et al.*, “Neurological adverse event profile of magnetic resonance imaging–guided focused ultrasound thalamotomy for essential tremor,” *Mov. Disord.*, vol. 33, no. 5, pp. 843–847, Apr. 2018.
[52] C. H. Halpern *et al.*, “Three-year follow-up of prospective trial of focused ultrasound thalamotomy for essential tremor,” *Neurology*, vol. 93, no. 24, pp. E2284–E2293, Dec. 2019.
[53] M. Rohani and A. Fasano, “Focused Ultrasound for Essential Tremor: Review of the Evidence and Discussion of Current Hurdles.,” *Tremor Other Hyperkinet. Mov. (N. Y).*, vol. 7, p. 462, 2017.
[54] F. Fennessy, K. Fischer, N. McDannold, F. Jolesz, and C. Tempany, “Potential of minimally invasive procedures in the treatment of uterine fibroids: a focus on magnetic resonance-guided focused ultrasound therapy,” *Int. J. Womens. Health*, vol. 7, p. 901, 2015.
[55] J. R. Sukovich *et al.*, “In vivo histotripsy brain treatment,” *J. Neurosurg.*, vol. 131, no. 4, pp. 1331–1338, Oct. 2019.
[56] T. Gerhardson, J. R. Sukovich, A. S. Pandey, T. L. Hall, C. A. Cain, and Z. Xu, “Effect of Frequency and Focal Spacing on Transcranial Histotripsy Clot Liquefaction, Using Electronic Focal Steering,” *Ultrasound Med. Biol.*, vol. 43, no. 10, pp. 2302–2317, Oct. 2017.
[57] S.-Y. Wu *et al.*, “Efficient Blood-Brain Barrier Opening in Primates with Neuronavigation-Guided Ultrasound and Real-Time Acoustic Mapping,” *Sci. Rep.*, vol. 8, no. 1, p. 7978, Dec. 2018.
[58] C. Poon, D. McMahon, and K. Hynynen, “Noninvasive and targeted delivery of therapeutics to the brain using focused ultrasound,” *Neuropharmacology*, vol. 120, pp. 20–37, 2017.
[59] F. Marquet *et al.*, “Real-time, transcranial monitoring of safe blood-brain barrier opening in non-human primates,” *PLoS One*, vol. 9, no. 2, 2014.
[60] N. Sheikov, N. McDannold, S. Sharma, and K. Hynynen, “Effect of Focused Ultrasound Applied With an Ultrasound Contrast Agent on the Tight Junctional Integrity of the Brain Microvascular Endothelium,” *Ultrasound Med. Biol.*, vol. 34, no. 7, pp. 1093–1104, 2008.
[61] L. H. Treat, N. McDannold, N. Vykhodtseva, Y. Zhang, K. Tam, and K. Hynynen, “Targeted delivery of doxorubicin to the rat brain at therapeutic levels using MRI-guided focused ultrasound,” *Int. J. Cancer*, vol. 121, no. 4, pp. 901–907, 2007.
[62] C. Y. Wu, C. H. Fan, N. H. Chiu, Y. J. Ho, Y. C. Lin, and C. K. Yeh, “Targeted delivery of engineered auditory sensing protein for ultrasound neuromodulation in the brain,” *Theranostics*, vol. 10, no. 8, pp. 3546–3561, 2020.

[63] J. O. Szablowski, A. Lee-Gosselin, B. Lue, D. Malounda, and M. G. Shapiro, “Acoustically targeted chemogenetics for the non-invasive control of neural circuits,” *Nat. Biomed. Eng.*, vol. 2, no. 7, pp. 475–484, Jul. 2018.

[64] J. B. Wang, M. Aryal, Q. Zhong, D. B. Vyas, and R. D. Airan, “Noninvasive Ultrasonic Drug Uncaging Maps Whole-Brain Functional Networks,” *Neuron*, vol. 100, no. 3, pp. 728-738.e7, Nov. 2018.

[65] P. F. Yang *et al.*, “Bidirectional and state-dependent modulation of brain activity by transcranial focused ultrasound in non-human primates,” *Brain Stimul.*, vol. 14, no. 2, pp. 261–272, Mar. 2021.

[66] W. J. Fry and F. J. Fry, “Fundamental Neurological Research and Human Neurosurgery Using Intense Ultrasound,” *IRE Trans. Med. Electron.*, vol. ME-7, no. 3, pp. 166–181, 1960.

[67] F. J. Fry, H. W. Ades, and W. J. Fry, “Production of reversible changes in the central nervous system by ultrasound,” *Science (80-.).*, vol. 127, no. 3289, pp. 83–84, Jan. 1958.

[68] W. J. Tyler, Y. Tufail, M. Finsterwald, M. L. Tauchmann, E. J. Olson, and C. Majestic, “Remote Excitation of Neuronal Circuits Using Low-Intensity, Low-Frequency Ultrasound,” *PLoS One*, vol. 3, no. 10, p. e3511, Oct. 2008.

[69] Y. Tufail *et al.*, “Transcranial Pulsed Ultrasound Stimulates Intact Brain Circuits,” *Neuron*, vol. 66, no. 5, pp. 681–694, 2010.

[70] Y. Younan, T. Deffieux, B. Larrat, M. Fink, M. Tanter, and J.-F. Aubry, “Influence of the pressure field distribution in transcranial ultrasonic neurostimulation,” *Med. Phys.*, vol. 40, no. 8, p. 082902, Jul. 2013.

[71] S.-S. Yoo, K. Yoon, P. Croce, A. Cammalleri, R. W. Margolin, and W. Lee, “Focused ultrasound brain stimulation to anesthetized rats induces long-term changes in somatosensory evoked potentials,” *Int. J. Imaging Syst. Technol.*, Dec. 2017.

[72] H. Kim, M. Y. Park, S. D. Lee, W. Lee, A. Chiu, and S.-S. Yoo, “Suppression of EEG visual-evoked potentials in rats through neuromodulatory focused ultrasound.,” *Neuroreport*, vol. 26, no. 4, pp. 211–5, Mar. 2015.

[73] S.-S. Yoo *et al.*, “Focused ultrasound modulates region-specific brain activity.,” *Neuroimage*, vol. 56, no. 3, pp. 1267–75, Jun. 2011.

[74] S. Herculano-Houzel, “The human brain in numbers: a linearly scaled-up primate brain,” *Front. Hum. Neurosci.*, vol. 3, p. 31, Nov. 2009.

[75] T. Deffieux, Y. Younan, N. Wattiez, M. Tanter, P. Pouget, and J.-F. Aubry, “Low-Intensity Focused Ultrasound Modulates Monkey Visuomotor Behavior,” *Curr. Biol.*, vol. 23, no. 23, pp. 2430–2433, Dec. 2013.

[76] N. Wattiez *et al.*, “Transcranial ultrasonic stimulation modulates single-neuron discharge in macaques performing an antisaccade task,” *Brain Stimul.*, vol. 10, no. 6, pp. 1024–1031, Nov. 2017.

[77] K. A. Lowe *et al.*, “Visuomotor Transformations Are Modulated by Focused Ultrasound over Frontal Eye Field,” *Ultrasound Med. Biol.*, Dec. 2020.

[78] L. Verhagen *et al.*, “Offline impact of transcranial focused ultrasound on cortical activation in primates,” *Elife*, vol. 8, Feb. 2019.

[79] W. Lee, Y. A. Chung, Y. Jung, I.-U. Song, and S.-S. Yoo, “Simultaneous acoustic stimulation of human primary and secondary somatosensory cortices using transcranial focused

ultrasound," *BMC Neurosci.*, vol. 17, no. 1, p. 68, 2016.
[80] W. Lee, H. Kim, Y. Jung, I.-U. Song, Y. A. Chung, and S.-S. Yoo, "Image-Guided Transcranial Focused Ultrasound Stimulates Human Primary Somatosensory Cortex," *Sci. Rep.*, vol. 5, no. 1, p. 8743, 2015.
[81] J. Mueller, W. Legon, A. Opitz, T. F. Sato, and W. J. Tyler, "Transcranial focused ultrasound modulates intrinsic and evoked EEG dynamics," *Brain Stimul.*, vol. 7, no. 6, pp. 900–908, 2014.
[82] W. Legon, P. Bansal, R. Tyshynsky, L. Ai, and J. K. Mueller, "Transcranial focused ultrasound neuromodulation of the human primary motor cortex," vol. 8, no. 1, p. 10007, Dec. 2018.
[83] W. Legon, L. Ai, P. Bansal, and J. K. Mueller, "Neuromodulation with single-element transcranial focused ultrasound in human thalamus," *Hum. Brain Mapp.*, Jan. 2018.
[84] J.-F. Aubry, M. Tanter, M. Pernot, J.-L. Thomas, and M. Fink, "Experimental demonstration of noninvasive transskull adaptive focusing based on prior computed tomography scans," *J. Acoust. Soc. Am.*, vol. 113, no. 1, pp. 84–93, Jan. 2003.
[85] K. Mahoney, T. Fjield, N. McDannold, G. Clement, and K. Hynynen, "Comparison of modelled and observed in vivo temperature elevations induced by focused ultrasound: Implications for treatment planning," *Phys. Med. Biol.*, vol. 46, no. 7, pp. 1785–1798, Jul. 2001.
[86] I. M. Hallaj and R. O. Cleveland, "FDTD simulation of finite-amplitude pressure and temperature fields for biomedical ultrasound," *J. Acoust. Soc. Am.*, vol. 105, no. 5, pp. L7–L12, May 1999.
[87] C. W. Connor and K. Hynynen, "Patterns of thermal deposition in the skull during transcranial focused ultrasound surgery," *IEEE Trans. Biomed. Eng.*, vol. 51, no. 10, pp. 1693–1706, Oct. 2004.
[88] K. Yoon, W. Lee, P. Croce, A. Cammalleri, and S.-S. Yoo, "Multi-resolution simulation of focused ultrasound propagation through ovine skull from a single-element transducer," *Phys. Med. Biol.*, vol. 63, no. 10, p. 105001, May 2018.
[89] U. Vyas and D. Christensen, "Ultrasound beam simulations in inhomogeneous tissue geometries using the hybrid angular spectrum method," *{IEEE} Trans. Ultrason. Ferroelectr. Freq. Control*, vol. 59, no. 6, pp. 1093–1100, Jun. 2012.
[90] S. Almquist, D. L. Parker, and D. A. Christensen, "Rapid full-wave phase aberration correction method for transcranial high-intensity focused ultrasound therapies," *J. Ther. Ultrasound*, vol. 4, no. 1, p. 30, 2016.
[91] M. A. Phipps *et al.*, "Considerations for ultrasound exposure during transcranial MR acoustic radiation force imaging," *Sci. Rep.*, vol. 9, no. 1, pp. 1–11, Dec. 2019.
[92] V. Ozenne *et al.*, "MRI monitoring of temperature and displacement for transcranial focus ultrasound applications," *Neuroimage*, vol. 204, p. 116236, Jan. 2020.
[93] B. E. Treeby and B. T. Cox, "k-Wave: MATLAB toolbox for the simulation and reconstruction of photoacoustic wave fields," *J. Biomed. Opt.*, vol. 15, no. 2, p. 021314, 2010.
[94] B. E. Treeby, J. Jaros, A. P. Rendell, and B. T. Cox, "Modeling nonlinear ultrasound propagation in heterogeneous media with power law absorption using a *k* -space pseudospectral method," *J. Acoust. Soc. Am.*, vol. 131, no. 6, pp. 4324–4336, Jun. 2012.

[95] J. L. B. Robertson, B. T. Cox, J. Jaros, and B. E. Treeby, “Accurate simulation of transcranial ultrasound propagation for ultrasonic neuromodulation and stimulation,” *J. Acoust. Soc. Am.*, vol. 141, no. 3, pp. 1726–1738, 2017.
[96] J. L. Robertson, B. T. Cox, and B. E. Treeby, “Quantifying numerical errors in the simulation of transcranial ultrasound using pseudospectral methods,” in *IEEE International Ultrasonics Symposium, IUS*, 2014, pp. 2000–2003.
[97] H. H. Pennes, “Analysis of Tissue and Arterial Blood Temperatures in the Resting Human Forearm,” *J. Appl. Physiol.*, vol. 1, no. 2, pp. 93–122, Aug. 1948.
[98] W. L. Nyborg, “Heat generation by ultrasound in a relaxing medium,” *J. Acoust. Soc. Am.*, vol. 70, no. 2, pp. 310–312, Aug. 1981.
[99] J.-F. Aubry, M. Tanter, M. Pernot, J.-L. Thomas, and M. Fink, “Experimental demonstration of noninvasive transskull adaptive focusing based on prior computed tomography scans,” *J. Acoust. Soc. Am.*, vol. 113, no. 1, pp. 84–93, Jan. 2003.
[100] T. D. Webb *et al.*, “Measurements of The Relationship Between CT Hounsfield Units and Acoustic Velocity and How it Changes with Photon Energy and Reconstruction Method,” *IEEE Trans. Ultrason. Ferroelectr. Freq. Control*, pp. 1–1, 2018.
[101] J. K. Mueller, L. Ai, P. Bansal, and W. Legon, “Numerical evaluation of the skull for human neuromodulation with transcranial focused ultrasound,” *J. Neural Eng.*, vol. 14, no. 6, p. 066012, Nov. 2017.
[102] G. W. Miller, M. Eames, J. Snell, and J. F. Aubry, “Ultrashort echo-time MRI versus CT for skull aberration correction in MR-guided transcranial focused ultrasound: In vitro comparison on human calvaria,” *Med. Phys.*, vol. 42, no. 5, pp. 2223–2233, Apr. 2015.
[103] S. Guo *et al.*, “Feasibility of ultrashort echo time images using full-wave acoustic and thermal modeling for transcranial MRI-guided focused ultrasound (tcMRgFUS) planning,” *Phys. Med. Biol.*, vol. 64, no. 9, p. 095008, Apr. 2019.
[104] P. Morris, A. Hurrell, A. Shaw, E. Zhang, and P. Beard, “A Fabry–Pérot fiber-optic ultrasonic hydrophone for the simultaneous measurement of temperature and acoustic pressure,” *J. Acoust. Soc. Am.*, vol. 125, no. 6, pp. 3611–3622, 2009.
[105] V. Rieke and K. B. Pauly, “MR thermometry,” *J. Magn. Reson. Imaging*, vol. 27, no. 2, pp. 376–390, 2008.
[106] J. Chen, R. Watkins, and K. B. Pauly, “Optimization of encoding gradients for MR-ARFI,” *Magn. Reson. Med.*, vol. 63, no. 4, pp. 1050–1058, 2010.
[107] E. A. Kaye, J. Chen, and K. B. Pauly, “Rapid MR-ARFI method for focal spot localization during focused ultrasound therapy,” *Magn. Reson. Med.*, vol. 65, no. 3, pp. 738–743, 2011.
[108] R. Paquin *et al.*, “Keyhole acceleration for magnetic resonance acoustic radiation force imaging (MR ARFI),” *Magn. Reson. Imaging*, vol. 31, no. 10, pp. 1695–1703, 2013.
[109] W. Lee *et al.*, “Image-Guided Focused Ultrasound-Mediated Regional Brain Stimulation in Sheep,” *Ultrasound Med. Biol.*, vol. 42, no. 2, pp. 459–470, 2016.
[110] D. P. Perrin *et al.*, “Image Guided Surgical Interventions,” *Curr. Probl. Surg.*, vol. 46, no. 9, pp. 730–766, Sep. 2009.
[111] J. B. West and C. R. Maurer, “Designing optically tracked instruments for image-guided surgery,” *IEEE Trans. Med. Imaging*, vol. 23, no. 5, pp. 533–545, May 2004.
[112] J. Michael Fitzpatrick, J. B. West, and C. R. Maurer, “Predicting error in rigid-body point-

based registration," *IEEE Trans. Med. Imaging*, vol. 17, no. 5, pp. 694–702, 1998.
[113] D. W. Eggert, A. Lorusso, and R. B. Fisher, "Estimating 3-D rigid body transformations: A comparison of four major algorithms," *Mach. Vis. Appl.*, vol. 9, no. 5–6, pp. 272–290, 1997.
[114] H. Kim, A. Chiu, S. Park, and S. S. Yoo, "Image-guided navigation of single-element focused ultrasound transducer," *Int. J. Imaging Syst. Technol.*, vol. 22, no. 3, pp. 177–184, 2012.
[115] V. Chaplin *et al.*, "On the accuracy of optically tracked transducers for image-guided transcranial ultrasound," *Int. J. Comput. Assist. Radiol. Surg.*, vol. In press., 2019.
[116] K. C. Wei *et al.*, "Neuronavigation-guided focused ultrasound-induced blood-brain barrier opening: A preliminary study in swine," *Am. J. Neuroradiol.*, vol. 34, no. 1, pp. 115–120, Jan. 2013.
[117] J. Blackmore, S. Shrivastava, J. Sallet, C. R. Butler, and R. O. Cleveland, "Ultrasound Neuromodulation: A Review of Results, Mechanisms and Safety," *Ultrasound Med. Biol.*, vol. 45, no. 7, pp. 1509–1536, Jul. 2019.
[118] M. L. Schwartz *et al.*, "Skull bone marrow injury caused by {MR}-guided focused ultrasound for cerebral functional procedures," *J. Neurosurg.*, pp. 1–5, May 2018.
[119] N. McDannold, P. J. White, and R. Cosgrove, "Predicting Bone Marrow Damage in the Skull After Clinical Transcranial MRI-Guided Focused Ultrasound With Acoustic and Thermal Simulations," *IEEE Trans. Med. Imaging*, vol. 39, no. 10, pp. 3231–3239, Oct. 2020.
[120] H. Wang *et al.*, "Brain temperature and its fundamental properties: A review for clinical neuroscientists," *Front. Neurosci.*, vol. 8, no. SEP, pp. 1–17, 2014.
[121] L. Marsac *et al.*, "MR-guided adaptive focusing of therapeutic ultrasound beams in the human head," *Med. Phys.*, vol. 39, no. 2, pp. 1141–1149, Feb. 2012.
[122] G. ter Haar, "Ultrasonic imaging: Safety considerations," *Interface Focus*, vol. 1, no. 4. The Royal Society, pp. 686–697, May-2011.
[123] S. V. Jonathan, "Advancements in MRI-based Methods for Targeting Transcranial Focused Ultrasound," 2020.
[124] E. . Brujan, "The role of cavitation microjets in the therapeutic applications of ultrasound," *Ultrasound Med. Biol.*, vol. 30, no. 3, pp. 381–387, Mar. 2004.
[125] G. Pinton, J.-F. Aubry, E. Bossy, M. Muller, M. Pernot, and M. Tanter, "Attenuation, scattering, and absorption of ultrasound in the skull bone," *Med. Phys.*, vol. 39, no. 1, pp. 299–307, 2011.
[126] P. Gaur *et al.*, "Histologic safety of transcranial focused ultrasound neuromodulation and magnetic resonance acoustic radiation force imaging in rhesus macaques and sheep," *Brain Stimul.*, vol. 13, no. 3, pp. 804–814, May 2020.
[127] J. Song, A. Pulkkinen, Y. Huang, and K. Hynynen, "Investigation of standing-wave formation in a human skull for a clinical prototype of a large-aperture, transcranial mr-guided focused ultrasound (MRgFUS) phased array: An experimental and simulation study," *IEEE Trans. Biomed. Eng.*, vol. 59, no. 2, pp. 435–444, Feb. 2012.
[128] T. Khokhlova *et al.*, "Dependence of inertial cavitation induced by high intensity focused ultrasound on transducer *F* -number and nonlinear waveform distortion," *J. Acoust. Soc. Am.*, vol. 144, no. 3, pp. 1160–1169, Sep. 2018.

[129] P. B. Rosnitskiy *et al.*, "Design of HIFU transducers for generating specified nonlinear ultrasound fields," *IEEE Trans. Ultrason. Ferroelectr. Freq. Control*, vol. 64, no. 2, pp. 374–390, Feb. 2017.
[130] K. Nightingale, "Acoustic Radiation Force Impulse (ARFI) Imaging: a Review," *Curr. Med. Imaging Rev.*, vol. 7, no. 4, pp. 328–339, 2012.
[131] O. V. Rudenko, A. P. Sarvazyan, and S. Y. Emelianov, "Acoustic radiation force and streaming induced by focused nonlinear ultrasound in a dissipative medium," *J. Acoust. Soc. Am.*, vol. 99, no. 5, pp. 2791–2798, May 1996.
[132] V. Andreev, V. Dmitriev, Y. A. Pishchal'nikov, O. Rudenko, O. Sapozhnikov, and A. Sarvazyan, "Observation of Shear Waves Excited by Focused Ultrasound in a Rubber-like Medium," *Acoust. Phys.*, vol. 43, no. 2, 1997.
[133] A. Ilovitsh, B. Z. Fite, T. Ilovitsh, and K. W. Ferrara, "Acoustic radiation force imaging using a single-shot spiral readout," *Phys. Med. Biol.*, vol. 64, no. 12, p. 125004, Jun. 2019.
[134] W. J. Elias *et al.*, "A Randomized Trial of Focused Ultrasound Thalamotomy for Essential Tremor," *N. Engl. J. Med.*, vol. 375, no. 8, pp. 730–739, 2016.
[135] Y. Meng *et al.*, "Technical Principles and Clinical Workflow of Transcranial MR-Guided Focused Ultrasound," *Stereotact. Funct. Neurosurg.*, pp. 1–14, Dec. 2020.
[136] E. Martin, D. Jeanmonod, A. Morel, E. Zadicario, and B. Werner, "High-intensity focused ultrasound for noninvasive functional neurosurgery," *Ann. Neurol.*, vol. 66, no. 6, pp. 858–861, 2009.
[137] H. Bjartmarz and S. Rehncrona, "Comparison of Accuracy and Precision between Frame-Based and Frameless Stereotactic Navigation for Deep Brain Stimulation Electrode Implantation," *Stereotact. Funct. Neurosurg.*, vol. 85, no. 5, pp. 235–242, Aug. 2007.
[138] M. Rahman, G. J. A. Murad, and J. Mocco, "Early history of the stereotactic apparatus in neurosurgery," *Neurosurg. Focus*, vol. 27, no. 3, 2009.
[139] N. McDannold, "Quantitative MRI-based temperature mapping based on the proton resonant frequency shift: Review of validation studies," *Int. J. Hyperth.*, vol. 21, no. 6, pp. 533–546, 2005.
[140] A. P. Sarvazyan, O. V. Rudenko, S. D. Swanson, J. B. Fowlkes, and S. Y. Emelianov, "Shear wave elasticity imaging: A new ultrasonic technology of medical diagnostics," *Ultrasound Med. Biol.*, vol. 24, no. 9, pp. 1419–1435, Dec. 1998.
[141] J. Ruohonen and J. Karhu, "Navigated transcranial magnetic stimulation," *Neurophysiologie Clinique*, vol. 40, no. 1. Elsevier Masson s.r.l., pp. 7–17, 01-Mar-2010.
[142] U. Herwig *et al.*, "The navigation of transcranial magnetic stimulation," *Psychiatry Res. - Neuroimaging*, vol. 108, no. 2, pp. 123–131, Nov. 2001.
[143] M. Cincotta *et al.*, "Optically tracked neuronavigation increases the stability of hand-held focal coil positioning: Evidence from 'transcranial' magnetic stimulation-induced electrical field measurements," *Brain Stimul.*, vol. 3, no. 2, pp. 119–123, Apr. 2010.
[144] F. Kral, E. J. Puschban, H. Riechelmann, and W. Freysinger, "Comparison of optical and electromagnetic tracking for navigated lateral skull base surgery," *Int. J. Med. Robot. Comput. Assist. Surg.*, vol. 9, no. 2, pp. 247–252, Jun. 2013.
[145] R. F. Labadie, B. M. Davis, and J. M. Fitzpatrick, "Image-guided surgery: What is the accuracy?," *Current Opinion in Otolaryngology and Head and Neck Surgery*, vol. 13, no. 1. Curr Opin Otolaryngol Head Neck Surg, pp. 27–31, Feb-2005.

[146] FUS-Foundation, “Focused Ultrasound for Glioblastoma Workshop Summary,” Charlottesville, VA, 2015.
[147] A. Fedorov *et al.*, “3D Slicer as an image computing platform for the Quantitative Imaging Network,” *Magn. Reson. Imaging*, vol. 30, no. 9, pp. 1323–1341, Nov. 2012.
[148] J. Tokuda *et al.*, “OpenIGTLink: An open network protocol for image-guided therapy environment,” *Int. J. Med. Robot. Comput. Assist. Surg.*, vol. 5, no. 4, pp. 423–434, Dec. 2009.
[149] T. Ungi, A. Lasso, and G. Fichtinger, “Open-source platforms for navigated image-guided interventions,” *Medical Image Analysis*, vol. 33. Elsevier B.V., pp. 181–186, 01-Oct-2016.
[150] J. M. Fitzpatrick, D. L. G. Hill, and C. R. Maurer Jr, “Image Registration,” in *Handbook of Medical Imaging, Volume 2, Medical Image Processing and Analysis*, M. Sonka and J. M. Fitzpatrick, Eds. Bellingham, WA: SPIE Press, 2000.
[151] L. Di Biase, E. Falato, and V. Di Lazzaro, “Transcranial Focused Ultrasound (tFUS) and Transcranial Unfocused Ultrasound (tUS) neuromodulation: From theoretical principles to stimulation practices,” *Front. Neurol.*, vol. 10, no. JUN, p. 549, 2019.
[152] D. Folloni *et al.*, “Manipulation of Subcortical and Deep Cortical Activity in the Primate Brain Using Transcranial Focused Ultrasound Stimulation,” *Neuron*, vol. 101, no. 6, pp. 1109-1116.e5, Mar. 2019.
[153] F. M. Miezin, L. Maccotta, J. M. Ollinger, S. E. Petersen, and R. L. Buckner, “Characterizing the hemodynamic response: Effects of presentation rate, sampling procedure, and the possibility of ordering brain activity based on relative timing,” *Neuroimage*, vol. 11, no. 6 I, pp. 735–759, 2000.
[154] A. Singh, A. G. Nyankima, M. Anthony Phipps, V. Chaplin, P. A. Dayton, and C. Caskey, “Improving the heating efficiency of high intensity focused ultrasound ablation through the use of phase change nanodroplets and multifocus sonication,” *Phys. Med. Biol.*, vol. 65, no. 20, p. 205004, Oct. 2020.
[155] E. A. Kaye *et al.*, “Application of Zernike polynomials towards accelerated adaptive focusing of transcranial high intensity focused ultrasound,” *Med. Phys.*, vol. 39, no. 10, pp. 6254–6263, Sep. 2012.
[156] G. H. Wilson, P.-F. Yang, J. C. Gore, and L. M. Chen, “Correlated inter-regional variations in low frequency local field potentials and resting state BOLD signals within S1 cortex of monkeys,” *Hum. Brain Mapp.*, vol. 37, no. 8, pp. 2755–2766, Aug. 2016.
[157] B. P. Delhaye, K. H. Long, and S. J. Bensmaia, “Neural Basis of Touch and Proprioception in Primate Cortex,” *Comprehensive Physiology*, vol. 8, no. 4. NLM (Medline), pp. 1575–1602, 14-Sep-2018.
[158] P. J. White, G. T. Clement, and K. Hynynen, “Longitudinal and shear mode ultrasound propagation in human skull bone,” *Ultrasound Med. Biol.*, vol. 32, no. 7, pp. 1085–1096, Jul. 2006.
[159] M. Plaksin, E. Kimmel, and S. Shoham, “Cell-Type-Selective Effects of Intramembrane Cavitation as a Unifying Theoretical Framework for Ultrasonic Neuromodulation,” *eNeuro*, vol. 3, no. 3, pp. 1–16, 2016.
[160] T. Sato, M. G. Shapiro, and D. Y. Tsao, “Ultrasonic Neuromodulation Causes Widespread Cortical Activation via an Indirect Auditory Mechanism,” *Neuron*, vol. 98, no. 5, pp. 1031-1041.e5, Jun. 2018.

[161] H. Guo *et al.*, “Ultrasound Produces Extensive Brain Activation via a Cochlear Pathway,” *Neuron*, vol. 98, no. 5, pp. 1020-1030.e4, Jun. 2018.
[162] N. McDannold *et al.*, “Acoustic feedback enables safe and reliable carboplatin delivery across the blood-brain barrier with a clinical focused ultrasound system and improves survival in a rat glioma model,” *Theranostics*, vol. 9, no. 21, pp. 6284–6299, 2019.
[163] N. Sheikov, N. McDannold, N. Vykhodtseva, F. Jolesz, and K. Hynynen, “Cellular mechanisms of the blood-brain barrier opening induced by ultrasound in presence of microbubbles,” *Ultrasound Med. Biol.*, vol. 30, no. 7, pp. 979–989, Jul. 2004.
[164] M. Aryal, C. D. Arvanitis, P. M. Alexander, and N. McDannold, “Ultrasound-mediated blood-brain barrier disruption for targeted drug delivery in the central nervous system,” *Adv. Drug Deliv. Rev.*, vol. 72, pp. 94–109, 2014.
[165] M. A. Phipps, S. Jonathan, P. F. Yang, L. M. Chen, W. Grissom, and C. F. Caskey, “Increasing radiation force-induced displacement at matched pressure by reducing effective aperture,” in *IEEE International Ultrasonics Symposium, IUS*, 2020, vol. 2020-September.